Higher-Order Structure Formation, Phase Transition, and Distribution of Polymorphic Crystals of Biodegradable Polymers Studied Using Time-Resolved Infrared Spectroscopy, X-ray Scattering, and High-Resolution Raman Imaging Techniques

A Thesis for the Degree

of

Doctor of Science

Submitted to

School of Science and Technology

Kwansei-Gakuin University

By

Mengfan WANG

in May 2017

Contents

List of Symbols and Abbreviations

2D	two dimensional
2*θ*	diffraction/scattering angle of the X-ray measurement
AFM	atomic force microscope
ATR-FTIR	attenuated total reflection Fourier-transform infrared
CCD	charge-coupled device
C=O	carbonyl group
<d>	averaged lamellar thickness of the stacked lamellar structure
D	dichroic ratio
DSC	differential scanning calorimetry
FTIR	Fourier-transform infrared
GI-WAXD	grazing incidence wide angle X-ray diffraction
HB(s)	hydrogen bonding(s)
inter	Intermolecular interactions exists between PHB molecular chains and chloroform molecules
inter, H	highly ordered intermediate structure of PHB
inter, L	less ordered intermediate structure of PHB
intra	intramolecular interactions
LP	long period of the stacked lamellar structure
MCT	mercury-cadmium-telluride
MW	weight-averaged molecular weight of polymer chains

NA	numerical aperture of object lens
PBA	poly(butylene adipate)
PHAs	poly(hydroxyalkanoate)s
PHB	poly(3-hydroxybutyrate)
POM	polarized optical microscope
$\boldsymbol{\theta_c}$	critical angle for total reflection
Q	scattering invariant
S	banding spacing of the ring-banded PBA spherulites
SAXS	small-angle X-ray scattering
SEC	solvent evaporation crystallization
$\boldsymbol{T_c}$	crystallization temperature
$\boldsymbol{T_g}$	glass transition temperature
$\boldsymbol{T_m}$	melting temperature
WAXD	wide angle X-ray diffraction
$\boldsymbol{X_{Crys}}$	weight fractions of crystalline structure
$\boldsymbol{X_{inter,\ H}}$	weight fractions of highly ordered intermediate structure
$\boldsymbol{X_{inter,\ L}}$	weight fractions of less ordered intermediate structure

General Introduction

This thesis is mainly focused on investigating the crystal structure evolution and the distribution of polymorphic crystals within semicrystalline biodegradable polymers. Semicrystalline biodegradable polymers are very important kinds of polymer materials, which have been widely used in our daily life. For the real application of the biodegradable polymers, it is indubitable that the mechanical property and biodegradability are always the most important. These properties are highly related to the inner physical structure of the biodegradable polymers, such as crystal structures, crystal morphologies, crystal or amorphous phase distribution, etc. Therefore, the knowledge about these factors will help us better understanding and application of the biodegradable polymers.

A crystal structure, or a crystal phase, can form by a phase transition process from an amorphous phase or another crystal phase. Phase transition from the amorphous phase is usually called crystallization, and that from the crystal phase is named as crystal phase transition. Note that the phase transition behavior for polymeric materials is a multiple process, containing the evolution of complex hierarchical structures. Therefore, the research on the phase transition process is one of the most important topics of polymers. In the first and second chapters of this thesis, two typical semicrystalline biodegradable polymers, poly(3-hydroxybutyrate) (PHB) and poly(butylene adipate) (PBA) (also named poly(tetramethylene adipate) (PTMA)) were chosen as candidates to systemically investigate the crystallization process during solvent evaporation and crystal phase transition behavior by using time-dependent attenuated total reflection Fourier-transform infrared (ATR-FTIR) spectroscopy, FTIR spectroscopy, grazing incidence wide angle X-ray diffraction (GI-WAXD), and WAXD/small-angle X-ray scattering (SAXS).

The crystal morphologies, such as spherulitic morphologies and the distribution of the different phases within the polymeric material system can also affect the biodegradability. Since different morphologies and phases show different biodegradability as well. When PBA is isothermal melt-recrystallized at an ambient temperature, it will exhibit both ring-banded spherulite and polymorphic crystals, which makes the situation more complicated. To investigate

that, Raman imaging technique is a good choice, for the reason that Raman imaging combines the information not just from the morphologies but also the molecular structure. In the third chapter of the present thesis, the author studied and discussed in detail the distribution of the polymorphic crystals within the spherulite of PBA using Raman imaging.

The originality and novelty of this thesis can be described as follows:

(1) Up to now, studies on the crystallization of PHB have been mainly concerned with melt crystallization process, but no related studies on solvent evaporation crystallization (SEC) process for PHB. Through the time-dependent ATR-FTIR spectra of PHB/chloroform solution during SEC process, the author found out that PHB/chloroform solution was in a homogeneous state at first. With the evaporation of chloroform, the separated PHB from the solution was in the mixture of intermediate and amorphous states, but no crystal structure formed due to the presence of chloroform. Moreover, there was no C－H···O=C intramolecular interactions within the intermediate structure of PHB. Subsequently, further evaporation induced a transition from intermediate phase to crystal phase and the formation of C－H···O=C intramolecular interactions within the latter. As the crystal structure developed, the intramolecular interaction become stronger due to the reduced intra-molecular distance within the lamella structure. Moreover, the time-dependent GI-WAXD profiles suggested the presence of two kinds of intermediate structures with different order (less ordered and highly ordered).

(2) The author have solved the long-term controversial problem about the mechanism of the *β*-to-*α* phase transition of PBA through the techniques of the time-resolved FTIR measurement as well as the simultaneous time-resolved WAXD/SAXS measurement in the quick and stable temperature jumping process, by which the time-dependent structural change has been traced quite clearly. The results indicated that the transformation from the *β*- to *α*-phase is not a solid-to-solid mechanism but occurs through the process of the melting of the *β*-phase into the amorphous phase followed by the subsequent recrystallization of the amorphous phase into the high temperature α-form.

(3) The relationship between ring-banded spherulites and polymorphic crystals behavior of PBA have been constructed based on Raman spectroscopy and Raman imaging technique. The characteristic Raman bands for *α*, *β*-form crystals and the amorphous phase of PBA, which are

suitable for quantitative analysis, have been identified. Through Raman imaging, the α- and β-form crystals of PBA uniformly distributed rather than alternate distributed as suggested by precious study within the ring-banded region and they grow together when the ring-banded PBA spherulites are formed.

1. Introduction of PHB and PBA

After the modern concept of polymers was proposed by Hermann Staudinger in 1920,[1] the polymeric materials have acted as an essential role in our daily life, since they hold wide range of properties. The polymeric materials can be divided into synthetic plastics and natural biopolymers, but they are all formed by many repeat subunits which are created through polymerization of the monomers. The traditional synthetic plastics which derived from petrochemicals, such as polyethylene (PE), polystyrene (PS), poly(vinyl chloride) (PVC), etc., have been popular for more than one century since they can displace traditional materials in the industries of packaging, piping, etc. However, with the big amount usage of the synthetic plastics, the serious challenges for the environment also become a worldwide problem. That is because these plastics are very stable and cannot be degraded naturally. Replacing the usage of traditional plastics by biodegradable polymers (or plastics) is a good idea to overcome the above problems; since the polymer chains in the biodegradable polymers can break down into small, stable end-products in physiological environments.[2] Moreover, some biodegradable polymers show not only good biocompatibility and bioresorbable but also excellent mechanical properties, which make them very suitable to be used in biomedical field, such as surgical suture, wound dressings, tissue engineering scaffolds, etc. The above advantages make biodegradable polymers a promising kind of materials and have received substantial interest in both fundamental research and technology in the recent several decades.[2,3]

1.1 PHB and Its Crystallization Behavior

Linear aliphatic polyesters, for example, PHB, is one of the most popular biodegradable materials. PHB, which belong to the poly(hydroxyalkanoate)s (PHAs) family, was first reported to isolate from the bacterial cells and to characterize by Maurice Lemoigne in the 1920s.[4] The chemical structure of PHB is presented in Figure 1(a), the typical features for not only PHB but

actually for all of the PHAs are that both of them having three-carbon backbone structure and one of the hydrogen atoms in the 3 position is substituted by an alkyl group,[4] and the different types of alkyl groups in the 3 position play an important role in determine the physical properties of PHAs[5].

That alkyl group for PHB is a methyl group ($-CH_3$), which can form a weak hydrogen bonding (HB) with a carbonyl group (C=O) within the PHB crystals. The HBs have been supposed to affect the thermal properties of the PHB crystals;[6,7] which will be introduced in the following paragraph. PHB can crystallize in two types of crystal modifications, the α and β forms. The chains within the crystal structure of α-form is packed in an orthorhombic unit cell ($P2_12_12_1$-D_2^4) having axes a=5.76 Å, b=13.2 Å and c(fiber period)=5.96 Å with left-handed 2_1 helical conformation;[8-10] while the polymer chains of β-form crystals with nearly planar zigzag conformation [11-13] packed in an hexagonal unit cell[12]. Since PHB with the α-form crystals are most commonly used, which can be easily produced by melt, cold and solution crystallization, it has been extensively studied.[6,7,14-29] PHB has a glass transition temperature (T_g) around 5 ℃[14] and a melting temperature (T_m) around 178 ℃[15]. Due to nearly perfect stereoregularity of its molecular chains, PHB can achieve relative high crystallinity, which makes PHB products perform similar mechanical properties to isotactic polypropylene (iPP).[30]

In 2004, Sato et al. firstly reported that C−H···O=C weak HBs existed between the C=O groups in one helix and one of the C−H groups of CH_3 groups in the adjacent helix within PHB α-form crystals by temperature-dependent FTIR and WAXD experiments,[6,7] the α-form crystal structure of PHB with HBs is illustrated in Figure 1(b). They showed the following evidences: (1) the IR band for CH_3 asymmetric stretching vibration appeared at an unusual high wavenumber (around 3009 cm^{-1}), while the corresponding C=O stretching mode showed relative low frequency shift to around 1731 cm^{-1};[7] (2) the distance between the H atom of the CH_3 group and the O atom of the C=O group (2.63 Å) is shorter than their van der waals separation (2.72 Å);[7,31] Recently, Wang and Tashiro have further confirmed such HBs on the basis of accurate crystal structure analysis and the normal mode calculations of the α-form PHB.[29]

For semicrystalline biodegradable polymers, like PHB, it is no doubted that the crystallization process is always the most important. Through controlling the crystal structures and the crystal morphologies, the crystallization can affect the final mechanical properties and biodegradability

for biodegradable polymers. Thus, the research topics about the crystallization is continuously popular throughout the development of the biodegradable polymers. The crystallization of polymer is a process that the polymer chains packed regularly into crystal region. Semicrystalline polymers consist of both crystalline and amorphous regions, since the usual length of the molecular chains is far greater than the size of the crystallites, one molecular chain is considered to pass through many crystalline and noncrystalline regions successively. Lotz and Cheng et al.[32,33] suggested that every polymer chain should go through several selection processes on different length and time scales during crystallization. Therefore, the transformation from the entangled melt into the crystalline state will pass several steps, and each step will corresponds to a different state. Based on a variety of evidence from experiments on several polymer systems, Strobl[34] suggested that the crystallization process from the amorphous state should passing over intermediate states (mesophase) before transforming to the lamellar crystallites. This novel crystallization model has been widely proven and used in the recent research of the semicrystalline polymers.[19,26,35-43]

Due to its exceptional purity and low nucleation density,[44,45] PHB is usually treated as a good model for investigating polymer crystallization behavior. FTIR spectroscopy and X-ray analysis are very popular techniques to study the crystallization behavior of polymer materials for a long time since not only they can provide abundant information about the crystal structure evolution, but they are also easy to be performed. FTIR spectroscopy can tell us the molecular structure change from a functional group level,[46] for example, conformations and intermolecular interaction change during crystallization. While X-ray analysis can give information from unit cell to lamellar periodical structure. Therefore, by combing the information from FTIR and X-ray, we can deeply understand the crystallization process.

Until now, by using FTIR,[17,19,40,41,47,48] WAXD,[26,49-52] and SAXS[26,50-52] techniques, the crystallization behavior of PHB and its copolymer have been extensively studied. Through time-dependent IR measurements combined with two-dimensional (2D) correlation analysis, Zhang et al.[19] investigated the isothermal melt-crystallization process of PHB. They found out that during crystallization, the amorphous C=O stretching bands at 1747 and 1739 cm^{-1}, the crystal band at 1731 cm^{-1} and another crystal band at 1728 cm^{-1} showed sequence change, and they suggested the band at 1731 cm^{-1} might come from the intermediate structure. Recently, Suttiwijitpukdee et al.[40] and Guo et al.[26] investigated and discussed the intermediate structure within PHB by time-resolved

FTIR spectroscopy and synchrotron WAXD/SAXS measurements, respectively in detail.

It should be noted that, the studies on the crystallization of PHB have been mainly concerned with isothermal melt-crystallization process at around 110 ℃ thus far, but there has few research about the SEC process. Being different from crystallization from pure polymers system, such as melt-crystallization, SEC is in general more complex,[53-56] since the solvent molecules usually exhibit complex interactions with polymer chains. Therefore, it is very necessary for us to investigate the SEC of PHB. Moreover, as mentioned above, HBs also exist within the lamellar structure of PHB, thus, study about the formation of HBs combining with the multiple crystal structure evolution during SEC (the molecular interaction exchange from polymer-solvent to polymer-polymer) is also very meaningful and importance.

An SEC PHB film is formed in a few minutes at room temperature by using the solvent of chloroform, however, to ensure better signal-to-noise ratio (SNR), it usually takes at least 30 s to obtain one IR spectrum. Therefore, it is very difficult to measure SEC by normal FTIR. In Chapter 1 of this thesis, a glass tube was used to hold the PHB/chloroform solution, and the author successfully investigated the SEC of PHB by using time-resolved ATR-FTIR and GI-WAXD methods. The author had detected the detail SEC process from homogeneous solution to phase separation and finally formation the crystal structure. The transformation of the intermediate structure and the evolution of the HBs were discussed systemically.

1.2 *β*-to-*α* Phase Transition Behavior and the Spherulite of PBA

PBA is also an important kind of biodegradable linear aliphatic polyester, different from PHB, PBA is petroleum-based polyester. PBA has shown its potential as it can be used in biomedical and ecofriendly materials. PBA is also an shared comonomer in poly(butylene adipate-co-terephthalate) (PBAT, Ecoflex®) and [57]poly(butylene succinate-co-adipate) (PBSA, Bionolle®), which are known for flexible, toughness and good processability, and have been widely applied in cling wrap for food packing, water resistant coatings, plastic bags, drug encapsulation systems, and so on.[58,59] Recent years, more attention has been paid on PBA for its complicated and interesting polymorphic crystalline structure, phase transition and crystal morphology.[60-80]

The chemical structure of PBA is shown in Figure 2(a). PBA has been reported to crystallize

into two types of crystal modifications under different conditions. The crystal structure of PBA was firstly studied by Fuller et al.[81-83] and the lattice parameters were further identified later by Minke et al.[84, 85] through studied the PBA single crystal. The α-form is characterized by its chain conformation of the planar zigzag type and these chains are packed in the monoclinic unit cell with the dimensions of a = 6.73 Å, b = 7.94 Å, c (fiber period) = 14.20 Å and β = 45.5°, while the β-form of the planar zigzag chain conformation takes the orthorhombic unit cell with the dimensions of a = 5.06 Å, b = 7.35 Å and c (fiber period) = 14.67 Å.[84, 85] The crystal structures of PBA are shown in Figure 2(b). It has been demonstrated that a film with α-form crystal structures has a higher degradation rate than that with β-form crystal structures, and that a film with both α- and β-form crystal structures shows the slowest degradation rate.[64]

1.2.1 β-to-α Phase Transition Behavior of PBA

In most of the cases, the β-form crystal structures for the linear aliphatic polyesters can be achieved only by stretching the polymer film or solution spun-coating to obtain the planar zigzag polymer chain conformation, like β-form PHB and PLA; by normal crystallization condition, such as solution-casting or isothermal melt-crystallization at T_c (crystallization temperature) higher than T_g, α-form is mainly formed. However, in the case of PBA, it has been reported that the β-form crystalline structure can be prepared by either stretching PBA film[77] or just by simply isothermal melt-crystallized at T_c that lower than 29 ℃[60] (The T_g of PBA is around -55 ℃). Moreover, when isothermal melt-crystallization at T_c that higher than 31 ℃, α-form crystals of PBA are mainly formed, while α- and β-form crystals are formed simultaneously at T_c that between 29 and 31 ℃. Such significantly temperature dependence of the PBA crystalline structure were firstly revealed by Gan et al.[60] In the same research, they also indicated that the α-phase of PBA can form through non-isothermal crystallization with slow cooling rate of 1 ℃/min from melt, while by fasters cooling (> 5 ℃/min), β-phase is dominantly developed.

Spontaneous transformation from the β-phase to the α-phase of bulk PBA can occur slowly by storing the specimen at room temperature for a week.[84] Which suggests that α-phase is thermodynamically more stable for the bulk PBA sample. This point was also proved by calculating the equilibrium melting temperature (T_m^0) value by both Gibbs-Thomson and Hoffman-

Weeks methods; the T_m^0 value for the α-form is shown higher than that for the β-form, indicating the α-form is a structure stable phase, while the β-form is a metastable phase.[62]

The mechanism of the β-to-α phase transition of PBA is still unclear until now, even though some groups have already done some works about that. Gan et al.[62] suggested this phase transition is a solid-to-solid process accompanied by the lamellar thickening, which based on the results of DSC, WAXD and SAXS. By time-resolved FTIR during annealing at 49 ℃[69] and temperature dependent FTIR during melting process of the β-form crystal structure[72], Yan et al.[69] and Yang et al.[72], respectively also indicated the solid-solid phase transition. On the contrary, through FTIR and WAXD measurements during heating process of the PBA/poly(4-vinylphenol) (PVPh) blends, Sun et al.[86] found out that the T_m of α-phase PBA depression with the addition of the PVPh, moreover, the β-to-α phase transition temperature showed parallel depression as well. They suggested that this phase transition might be a microdomain melting and recrystallization process. Li et al.[76] based on the results of time-dependent FTIR of ultrathin PBA film during annealing at 45 and 47 ℃, respectively, also suggested a melt-recrystallization phase transition process.

The controversial about the β-to-α phase transition of PBA is continuing since there is no direct evidence to demonstrate which is the really phase transition pathway. In general, the phase transition of the crystalline polymers usually occurs over a relatively wide temperature region; this is due to the crystallite size in the semicrystalline polymer distributes over a wide range and so the melting point itself distributes correspondingly.[87] Therefore, by the conventional temperature- or time-dependent X-ray and vibrational spectroscopic measurements, it is sometimes difficult to judge the phase transition process, since temporal resolution limitation. Moreover, to investigate the phase transition, the evolution of the amorphous structure is also very important to trace at the same time.

In Chapter 2 of the present thesis, a temperature-jump cell[88] was used, the illustration is shown in Figure 3. Based on the temperature-jump time-resolved measurement of the FTIR, WAXD and SAXS, the phase transition behavior of PBA has been systemically investigated. The author directly traced the sequentially-occurring change of the different phases, and found out that it is not a solid-to-solid phase transition but the combined phenomena of the melting of the β-phase followed by the recrystallization to the high temperature α-phase.

1.2.2 Spherulite of PBA

Spherulites of semicrystalline polymeric materials are spherically symmetric crystal colonies which formation from viscous melts or solutions with enough supercooling degree ΔT ($\Delta T = T_m - T_c$).[89-91] Spherulites are polycrystalline aggregates composed by highly anisometric crystallites called subindividuals or subunits; through polarized optical microscopy (POM) observation, the spherulite will shows dark Maltese cross pattern (Figure 4(a)), this is due to the fact that all transparent crystals that are not cubic are birefringent. The morphologies and the growth rate of the spherulites are highly depending both on the polymeric materials themselves and the crystallization conditions. For example, crystal structure,[92-96] chiral of the polymer chains,[97,98] molecular weight,[99,100] crystallization temperature,[101-103] film thickness,[104,105] etc.

Among various morphologies, ring-banded spherulites have been attracting considerable attention for several decades. The ring-banded spherulite not only shows Maltese cross, but also shows alternately concentric light-dark rings by POM observation. The typical ring-banded spherulite is shown in Figure 4(b). Evidences show that the ring-banded pattern is originated from the continuous helicoidally twisted of the lamellar crystals along the growth direction of the banded spherulite, with just a few exceptions.[89,106,107] The mechanism of the lamellar twisting has been considered over the decades, three major ideas have been proposed until now, they are: (1) unbalanced surface stress effects of the lamellae;[97,98,108] (2) isochiral giant screw dislocations along the lamellar crystals;[108,109] (3) response to the compositional or mechanical fields in the melt near the interface that generated during the crystal growth process[110]. It should be noted that the present theories are still not enough to release all of the ambiguities about the formation of the ring-banded spherulites, these theories will be improved to more perfect in the future with more deeply studying and understanding of this fascinating phenomenon.

The banding phenomenon is usually found in the spherulites of chiral polymers, such as PHAs,[98,111] PLA,[112,113] poly(propylene oxide) (PPO),[114] etc. However, some of the achiral polymers, for example, PBA, can also crystallized into ring-banded spherulite under specific conditions. It was firstly reported by Gan et al.[60] at 2002 that when isothermal melt-crystallized PBA in the temperature range of 30–33 ℃, banded spherulites were formed, while when the crystallization temperature below 29 ℃ or above 34 ℃, only ringless spherulites could form. What

more interesting they found was that the temperature region at which the ring-banded spherulites formed was just similar with the region that α- and β-form crystals of PBA can crystallized together, which has already mentioned in the Section 1.2.1. However, the ringless PBA spherulites only contain pure α- or β-form crystals.

Since this particular phenomenon, it is reasonable for people to wonder what the relationship is between ring-banded morphology and the polymorphic crystals. Thus, many studies have been done about this "correlation" since 2002.[64,65,67,71,73,74,115] Zhao et al.[67] first investigated the banded PBA spherulites based on the different biodegradation behaviors of the two crystal forms and the results of atomic force microscopy (AFM); they suggested that the banded spherulites are composed of alternating edge-on and flat-on lamellae along the radial direction, and that the edge-on and flat-on domains are composed of β- and α-form crystals, respectively. On the contrary, the following research by Woo et al.[71] revealed that the ring-banded pattern had no relation with the polymeric crystals, since they found the banded pattern can be composed by even singly α-form crystals. More recently, Liu et al.[73] researched the effect of the different molecular weights on the morphologies of the PBA spherulite. Their results showed that either α or β crystals can form regular ring-banded spherulites. The research by Wang et al.[74] also suggested the similar result through analyzed the crystallization behavior of PBA blended with structurally similar acrylic polymers.

Thus, the evidences from previous studies have shown that the mixture of the two crystal forms is not the fundamental reason for the formation of the ring-banded PBA spherulites. Even though, this particular phenomenon of PBA still left a lot of unresolved problem. For example, what is the truly reason that when PBA crystallized by itself, the ring-banded pattern only appear with the coexistence of the two crystal forms, but when the system is crystallized by just either one crystal form, only ringless spherulite can be detected and what is the formation process of the ring-banded PBA spherulite with polymeric crystals? What is more, the banded pattern which is formed by a single crystal form or by mixed crystal forms at the same crystallization temperature appear very different band spacing,[73] which means that the coexistence of the two crystal forms may affect the ring-banded morphology. In addition, since the two crystal forms result in different mechanical properties and biodegradation behavior, their distribution will also affect the final performances of the PBA products. Accordingly, more systematically works about the relationship

between PBA spherulite and its polymeric crystals are still very necessary to be done.

In order to achieve that final goal, the first step for us to do should be finding out the distribution of polymeric crystals in the ring-banded spherulites of PBA. Until now, a vast majority of spherulite studies rely on POM. Interpretations of the POM images can provide important information about the structures of spherulites;[89] however, POM cannot give detailed information on the internal structures. Recent years, vibrational spectroscopy-based chemical imaging technique, for instance, Raman or FTIR imaging technique, has showed its potential in the research of polymer science, since it combines the information from both morphology and molecular structure. Therefore high spatial resolution Raman imaging technique was used to investigate the distribution of polymeric crystals, as well as the molecular chains orientation within the ring-banded PBA spherulites for the first time. Moreover, since there is no Raman studies on PBA, particularly, the polymorphic crystals of PBA, have been reported thus far. Therefore, in present thesis, Raman spectroscopy and Raman imaging were used to explore the PBA spherulites for the first time. This part will be discussed in detail in Chapter 3 of the present thesis.

2. Vibrational Spectroscopy-Based Chemical Imaging Technique and Its Application in Polymer Science

Vibrational spectroscopy-based chemical imaging technique, which has application in various academic and industries fields, is a very powerful tool for solving real-world issues.[116] Raman and FTIR imaging are the two typical branches of vibrational spectroscopy-based chemical imaging. Simply speaking, these imaging techniques are combining the advantages of digital imaging techniques and vibrational spectroscopy. The key points of chemical imaging based on Raman or FTIR spectroscopy are chemical specificity and the abundant information that stems from the full-range spectra.

Both of the IR and Raman spectroscopy are based on the fact that the chemical bonds between two or more atoms vibrate continually, such as stretching, bending, wagging, etc. When a “light”, or in other words, an electromagnetic radiation incident to a material, some of it will be absorbed when its frequency is resonant with the molecular vibration within the material. The vibrational energy of the molecular will be excited to a higher energy state by absorbing the light, and higher

energy state usually relaxes back to the lowest energy state quickly by releasing heat and/or light.[116]

Assuming that the groups of atoms in a molecule are not vibrationally coupled to the rest of the molecule, which means they have almost the same vibration frequencies in any molecule. Therefore, it is possible to associate a vibrational frequency with a particular chemical functional group.[116] The IR and Raman spectra are the absorbance and scattering spectra, respectively, and the laser source of the IR and Raman are infrared light and visible laser, respectively. The basic principle of the IR and Raman spectroscopy have been well published elsewhere.[116]

The semicrystalline polymer system is usually in spatially inhomogeneous state, for example, there should contain crystal and amorphous phases at the same time. If a polymer also shows polymorphic crystals behavior, the situation will become more complex. Since different phases will show different properties, such as mechanical property and biodegradability. Thus, fully understanding the distribution of different phases in the polymer system is very important to control and predict its final performance.

Since different phases or structures usually have their own molecule-specific band(s) in the IR or Raman spectrum. Then, the imaging instrument are used to collect IR or Raman spectra associate with the sample from every pixel of the region that is interested. The final chemical image is generated by calculating the relative value (intensity, intensity ratio, etc.) of the molecule-specific band at each pixel, and then drawing these values in the Cartesian coordinates.[116] The schematic of chemical imaging technique is shown in Figure 5.

FTIR imaging has been extensively applied in the research of polymer science in the recent two decades since it can collect full IR image which containing hundreds or thousands of IR spectra in a few minutes.[28,41,42,96,113,117-127] For example, Siesler group have done a lot of work on various of polymer blending system by using FTIR imaging;[28,41,122-125] Hekima and Morikawa investigated the inner molecular chains orientation within the stretched polymer fiber and different kinds of spherulites of polymeric materials by polarized FTIR imaging through their newly proposed multipolarization calculation method.[113,126,127] Using the same method, Hu and Tashiro studied the phase transition behavior from form-II to form-I in the melt-grown spherulites of isotactic polybutene-1 (*it*-PB-1) at 25 ℃.[96] Even though FTIR imaging technique has many advantages, its spatial resolution is just around 5 μm by normal mode, which limits the application

of IR imaging if the inhomogeneous part is very small.

Compared to FTIR imaging, Raman imaging can give much better spatial resolution (0.3 μm can be achieved), and it can also provide marked information about the molecular structure. Raman imaging instrument usually composed by a laser source, optical microscopy system, computer-controlled motorized sample stage and a CCD detector. Back-scattering is the most common mode for Raman imaging measurement, which means that during Raman experiment, the laser always focus on the surface or any another point along the thickness direction of the sample, and thus, only the thin laser focus plane of the sample will be measured. This feature makes Raman imaging can easily be used to measure the sample in not only two-dimensional (2D) plane but also three-dimensional (3D) space. Hence, Raman imaging has shown its powerful in recent decades and has been widely applied to investigate the distribution of different phase and structures in polymeric materials.[28,128-133] For example, Van Apeldorn et al.[130] studied about the intracellular degradation behavior and mechanism of the poly(lactic-co-glycolic acid) (PLGA) microsphere inside macrophages by using confocal Raman spectroscopy and imaging with spatial resolution of 1.5 μm; Chernenko et al.[132] investigated the intracellular drug-delivery and degradation of the biodegradable nanocarrier systems of poly(ε-caprolactone) (PCL) and PLGA;[132] Huan et al. researched about the phase behavior in poly(ethylene terephthalate)/high-density poly(ethylene) (PET/HDPE) polymer blends using high-spatial resolution Raman imaging.

In the third chapter of the present thesis, Raman imaging technique was chosen to investigate the complex distribution of inner physical structure within ring-banded PBA spherulites instead of FTIR imaging. That is mainly due to that spatial resolution of FTIR imaging is not enough to investigate such small band spacing of PBA spherulites efficiency.

3. Outline of Each Chapter

The outline of each chapter for the present thesis will be described as follows.

This thesis consists of three chapters.

Chapter 1: this chapter describes the evolution of the intra-molecular interaction within PHB chains and inter-molecular interaction between PHB chains and chloroform molecules during SEC of PHB in a PHB/chloroform solution by using time-solved ATR-FTIR spectroscopy; and the

crystal structure formation of PHB during SEC by using time-solved GI-WAXD. From ATR-FTIR, it is found that the PHB/chloroform solution was in a homogeneous state at first, and within the solution, there contains the intermolecular interaction between C=O groups of the PHB chains and the C−H groups of chloroform. With the evaporation of chloroform, phase separation started since the solution concentration reached the saturation point, and PHB started to separate from the solution. The separated PHB was in the mixture of intermediate and amorphous states, but no crystal structure formed due to the presence of chloroform. Moreover, no C=O···H−C interaction within PHB was formed, which in other others, hydrogen bonding was not exist within the intermediate structure. Subsequently, further evaporation induced a transition from intermediate to crystal structure and the formation of C=O···H−C intramolecular interactions within the latter. As the crystal structure developed, the intramolecular interaction changed from weak to strong due to the reduced intra-molecular distance within the lamella structure. The results of the GI-WAXD, it is suggested the presence of two kinds of intermediate structures with different order (less ordered and highly ordered). During SEC, the intermediate structures formed firstly, subsequently transforming into a crystal structure.

Chapter 2: the mechanism of the *β*-to-*α* phase transition of PBA was systematically investigated by using the techniques of the time-resolved measurements of the FTIR spectra as well as the simultaneous time-resolved WAXD/SAXS measurements in the quick and stable temperature-jump process. A majority of papers published so far reported that the phase transition from the *β*-form to the *α*-form occurs as the direct solid-to-solid process when the sample is heated up to the high temperature. However, the author found out that this phase transition was not a solid-to-solid phase transition but the melting of the *β*-phase into the amorphous phase and the subsequently occurred recrystallization of the amorphous phase into the *α*-form. The *α*-phase obtained by the melt-recrystallization of the original *β*-phase is different not only in the lamellar stacking structure but also in the degree of orderliness in the crystal lattice compared to the normal *α*-phase as judged from the SAXS and WAXD data.

Chapter 3: in this chapter, the author discussed the polymorphic crystals and the molecular chains orientation within the PBA spherulites in detail by using Raman spectroscopy and Raman imaging technique. Special attention has been paid to the so-called “ring-banded” PBA spherulites with out-layer ringless region that were isothermally crystallized at T_c = 31–33 ℃. The

characteristic Raman peaks for both α- and β-form crystal structures and the amorphous structure of PBA were observed for the first time. These peaks were employed to investigate the polymorphic crystal distribution through Raman imaging. It was found that the center and ring-banded regions contained both α- and β-form crystals, while the out-layer region contained only α-form crystals. The α- and β-form crystals can nucleate and grow in the same temperature range (31–33 ℃), and the relative content of these two crystal forms within the ring-banded spherulites show temperature dependence. The higher isothermal melt-crystallization temperature, the higher content of the α-form crystals within the ring-banded PBA spherulites. The molecular chains within the PBA spherulites are oriented almost perpendicular to the spherulite growth direction. However, the ring-banded domains have different orientations about the substrate plane; the molecular chains orient perpendicular to the substrate plane in the flat-on domains and parallel to the substrate plane in the edge-on domains

References

1. Staudinger, H. Über polymerisation. *Eur. J. Inorg. Chem.* **1920**, 53, 1073–1085.
2. Pan, P.; Inoue, Y. Polymorphism and isomorphism in biodegradable polyesters. *Prog. Polym. Sci.* **2009**, 34, 605–640.
3. Nair, L. S.; Laurencin, C. T. Biodegradable polymers as biomaterials. *Prog. Polym. Sci.* **2007**, 32, 762–798.
4. Lenz, R. W.; Marchessault, R. H. Bacterial Polyesters: Biosynthesis, Biodegradable Plastics and Biotechnology. *Biomacromolecules* **2005**, 6, 1–8.
5. Anderson, A. J.; Dawes, E. A. Occurrence, metabolism, metabolic role, and industrial uses of bacterial polyhydroxyalkanoates. *Microbiol. Rev.* **1990**, 54, 450–472.
6. Sato, H.; Nakamura, M.; Padermshoke, A.; Yamaguchi, H.; Terauchi, H.; Ekgasit, S.; Noda, I.; Ozaki, Y. Thermal Behavior and Molecular Interaction of Poly(3-hydroxybutyrate-co-3-hydroxyhexanoate) Studied by Wide-Angle X-ray Diffraction. *Macromolecules* **2004**, 37, 3763–3769.
7. Sato, H.; Murakami, R.; Padermshoke, A.; Hirose, F.; Senda, K.; Noda, I.; Ozaki, Y. Infrared Spectroscopy Studies of CH ··O Hydrogen Bondings and Thermal Behavior of Biodegradable Poly(hydroxyalkanoate). *Macromolecules* **2004**, 37, 7203–7213.
8. Cobntbekt, J.; Mabchessault, R. H. Physical properties of poly-β-hydroxybutyrate: IV. Conformational analysis and crystalline structure. *J. Mol. Boil.* **1972**, 71, 735–756.
9. Yokouchi, M.; Chatani, Y.; Tadokoro, H.; Teranishi, K.; Tani, H. Structural studies of polyesters: 5. Molecular and crystal structures of optically active and racemic poly(β-hydroxybutyrate). *Polymer* **1973**, 14, 267–272.
10. Bruckner, S.; Meille, S. V.; Malpezzi, L.; Cesaro, A.; Navarini, L.; Tombolini, R. The Structure of Poly($_D$-(**–**)-*β*-hydroxybutyrate). A Refinement Based on the Rietveld Method. *Macromolecules* **1988**, 21, 967–972.
11. Yokouchi, M.; Chatani, Y.; Tadokoro, H.; Teranishi, K.; Tani, H. Structural studies of polyesters: 5. Molecular and crystal structures of optically active and racemic poly(β-hydroxybutyrate). *Polymer* **1973**, 14, 267–272.
12. Orts, W. J.; Marchessault, R. H.; Bluhm, T. L.; Hamer, G. K. Observation of Strain-Induced

β Form in Poly(β-hydroxyalkanoates). *Macromolecules* **1990**, 23, 5368–5370.

13. Lambeek, G.; VORENKAP, E. J.; Schouten, A. J. Structural Study of Langmuir-Blodgett Mono-and Multilayers of Poly(β-hydroxyburyrate). *Macromolecules* **1995**, 28, 2023–2032.
14. Lageveen, R. G.; Huisman, G. W.; Preusting, H.; Ketelaar, P.; Eggink, G.; Witholt, B. Formation of polyesters by Pseudomonas oleovorans: effect of substrates on formation and composition of poly-(R)-3-hydroxyalkanoates and poly-(R)-3-hydroxyalkenoates. *Appl. Environ. Microb.* **1988**, 54, 2924–2932.
15. Abe, H.; Doi, Y.; Aoki, H.; Akehata, T. Solid-State Structures and Enzymatic Degradabilities for Melt-Crystallized Films of Copolymers of (R)-3-Hydroxybutyric Acid with Different Hydroxyalkanoic Acids. *Macromolecules* **1998**, 31, 1791–1797.
16. Marchessault, R. H.; Kawada, J. PHB Lamellar Single Crystals: Origin of the Splintered Texture. *Macromolecules* **2004**, 37, 7418–7420.
17. Padermshoke, A.; Sato, H.; Katsumoto, Y.; Ekgasit, S.; Noda, I.; Ozaki, Y. Crystallization behavior of poly(3-hydroxybutyrate-co-3-hydroxyhexanoate) studied by 2D IR correlation spectroscopy. *Polymer* **2004**, 45, 7159–7165.
18. Padermshoke, A.; Katsumoto, Y.; Sato, H.; Ekgasit, S.; Noda, I.; Ozaki, Y. Surface melting and crystallization behavior of polyhydroxyalkanoates studied by attenuated total reflection infrared spectroscopy. *Polymer* **2004**, 45, 6547–6554.
19. Zhang, J.; Sato, H.; Noda, I.; Ozaki, Y. Conformation Rearrangement and Molecular Dynamics of Poly(3-hydroxybutyrate) during the Melt-Crystallization Process Investigated by Infrared and Two-Dimensional Infrared Correlation Spectroscopy. *Macromolecules* **2005**, 38, 4274–4281.
20. Furukawa, T.; Sato, H.; Murakami, R.; Zhang, J.; Noda, I.; Ochiai, S.; Ozaki, Y. Raman microspectroscopy study of structure, dispersibility, and crystallinity of poly(hydroxybutyrate)/poly(L-lactic acid) blends. *Polymer* **2006**, 47, 3132–3140.
21. Sato, H.; Mori, K.; Murakami, R.; Ando, Y.; Takahashi, I.; Zhang, J.; Terauchi, H.; Hirose, F.; Senda, K.; Tashiro, K.; Noda, I.; Ozaki, Y. Crystal and Lamella Structure and C−H ··O=C Hydrogen Bonding of Poly(3-hydroxyalkanoate) Studied by X-ray Diffraction and Infrared Spectroscopy. *Macromolecules* **2006**, 39, 1525–1531.
22. Hu, Y.; Zhang, J.; Sato, H.; Futami, Y.; Noda, I.; Ozaki, Y. C−H ··O═C Hydrogen Bonding

and Isothermal Crystallization Kinetics of Poly(3-hydroxybutyrate) Investigated by Near-Infrared Spectroscopy. *Macromolecules* **2006**, 39, 3841–3847.

23. Mori, K.; Mukoyama, S.; Zhang, Y.; Sato, H.; Ozaki, Y.; Terauchi, H.; Noda, I.; Takahashi, I. Crystalline Lamellae and Surface Morphology of Biodegradable Polyhydroxyalkanoate Thin Films: Thermal Behavior and Comparison between Poly(3-hydroxybutyrate-co-3-hydroxyhexanoate) and Poly(3-hydroxybutyrate). *Macromolecules* **2008**, 41, 1713–1719.
24. Androsch, R. Surface structure of folded-chain crystals of poly(R-3-hydroxybutyrate) of different chain length. *Polymer* **2008**, 49, 4673–4679.
25. Sato, H.; Ando, Y.; Mitomo, H.; Ozaki, Y. Infrared Spectroscopy and X-ray Diffraction Studies of Thermal Behavior and Lamella Structures of Poly(3-hydroxybutyrate-co-3-hydroxyvalerate) (P(HB-co-HV)) with PHB-Type Crystal Structure and PHV-Type Crystal Structure. *Macromolecules* **2011**, 44, 2829–2837.
26. Guo, L.; Spegazzini, N.; Sato, H.; Hashimoto, T.; Masunaga, H.; Sasaki, S.; Takata, M.; Ozaki, Y. Multistep Crystallization Process Involving Sequential Formations of Density Fluctuations, "Intermediate Structures", and Lamellar Crystallites: Poly(3-hydroxybutyrate) As Investigated by Time-Resolved Synchrotron SAXS and WAXD. *Macromolecules* **2012**, 45, 313–328.
27. Di Lorenzo, M. L.; Gazzano, M.; Righetti, M. C. The Role of the Rigid Amorphous Fraction on Cold Crystallization of Poly(3-hydroxybutyrate). *Macromolecules* **2012**, 45, 5684–5691.
28. Unger, M.; Sato, H.; Ozaki, Y.; Fischer, D.; Siesler, H. W. Temperature-Dependent Fourier Transform Infrared Spectroscopy and Raman Mapping Spectroscopy of Phase-Separation in a Poly(3-hydroxybutyrate)-Poly(L-lactic acid) Blend. *Appl. Spectrosc.* **2013**, 67, 141–148.
29. Wang, H.; Tashiro, K. Reinvestigation of Crystal Structure and Intermolecular Interactions of Biodegradable Poly(3-Hydroxybutyrate) α-Form and the Prediction of Its Mechanical Property. *Macromolecules* **2016**, 49, 581–594.
30. Satkowski, M. M.; Melik, D. H.; Autran, J. P.; Green, P. R.; Noda, I.; Schechtman, L. A., In Biopolymers; Steinbüchel, A., Doi, Y., Eds.; Wiley-VCH: Wienheim, Germany, 2001.
31. Sato, H.; Dybal, J.; Murakami, R.; Noda, I.; Ozaki, Y. Infrared and Raman spectroscopy and quantum chemistry calculation studies of C–H···O hydrogen bondings and thermal behavior of biodegradable polyhydroxyalkanoate. *J. Mole. Struct.* **2005**, 744–747: 35-46.

32. Lotz, B. What can polymer crystal structure tell about polymer crystallization processes? *Eur. Phys. J. E* **2000**, 3, 185–194.
33. Cheng, S.; Li, C. Y.; Zhu, L. Commentary on polymer crystallization: Selection rules in different length scales of a nucleation process. *Eur. Phys. J. E* **2000**, 3, 195–197.
34. Strobl, G. From the melt via mesomorphic and granular crystalline layers to lamellar crystallites: A major route followed in polymer crystallization? *Eur. Phys. J. E* **2000**, 3, 165–183.
35. Strobl, G. Crystallization and melting of bulk polymers: new observations, conclusions and a thermodynamic scheme. *Prog. Polym. Sci.* **2006**, 31, 398–442.
36. Qiu, J.; Wang, Z.; Yang, L.; Zhao, J.; Niu, Y.; Hsiao, B. S. Deformation-induced highly oriented and stable mesomorphic phase in quenched isotactic polypropylene. *Polymer* **2007**, 48, 6934–6947.
37. Konishi, T.; Nishida, K.; Matsuba, G.; Kanaya, T. Mesomorphic Phase of Poly(butylene-2, 6-naphthalate). *Macromolecules* **2008**, 41, 3157–3161.
38. Zhang, J.; Duan, Y.; Domb, A. J.; Ozaki, Y. PLLA Mesophase and Its Phase Transition Behavior in the PLLA−PEG−PLLA Copolymer As Revealed by Infrared Spectroscopy. *Macromolecules* **2010**, 43, 4240–4246.
39. Stoclet, G.; Seguela, R.; Lefebvre, J.; Rochas, C. New insights on the strain-induced mesophase of poly($_{D, L}$-lactide): in situ WAXS and DSC study of the thermo-mechanical stability. *Macromolecules* **2010**, 43, 7228–7237.
40. Suttiwijitpukdee, N.; Sato, H.; Zhang, J.; Hashimoto, T. Effects of Intermolecular Hydrogen Bondings on Isothermal Crystallization Behavior of Polymer Blends of Cellulose Acetate Butyrate and Poly(3-hydroxybutyrate). *Macromolecules* **2011**, 44, 3467–3477.
41. Unger, M.; Sato, H.; Ozaki, Y.; Siesler, H. W. Crystallization Behavior of Poly(3-hydroxybutyrate) (PHB), Poly(ε-caprolactone) (PCL) and Their Blend (50:50 wt.%) Studied by 2D FT-IR Correlation Spectroscopy. *Macromol. Symp.* **2011**, 305, 90–100.
42. Lan, Q.; Li, Y. Mesophase-Mediated Crystallization of Poly(l-lactide): Deterministic Pathways to Nanostructured Morphology and Superstructure Control. *Macromolecules* **2016**, 49, 7387–7399.
43. Lan, Q.; Li, Y.; Chi, H. Highly Enhanced Mesophase Formation in Glassy Poly(l-lactide) at

Low Temperatures by Low-Pressure CO_2 That Provides Moderately Increased Molecular Mobility. *Macromolecules* **2016**, 49, 2262–2271.

44. Barham, P. J.; Keller, A.; Otun, E. L.; Holmes, P. A. Crystallization and morphology of a bacterial thermoplastic: poly-3-hydroxybutyrate. *J. Mater. Sci.* **1984**, 19, 2781–2794.
45. Barham, P. J. Nucleation behaviour of poly-3-hydroxy-butyrate. *J. Mater. Sci.* **1984**, 19, 3826–3834.
46. Bower, D. I.; Maddams, W. F. *The vibrational spectroscopy of polymers*; Cambridge University Press: Cambridge, 1992.
47. Zhang, J.; Sato, H.; Furukawa, T.; Tsuji, H.; Noda, I.; Ozaki, Y. Crystallization Behaviors of Poly(3-hydroxybutyrate) and Poly($_L$-lactic acid) in Their Immiscible and Miscible Blends. *The J. Phys. Chem. B* **2006**, 110, 24463–24471.
48. Huang, H.; Guo, W.; Chen, H. In situ FTIR and generalized 2D IR correlation spectroscopic studies on the crystallization behavior of solution-cast PHB film. *Anal. Bioanal. Chem.* **2011**, 400, 279–288.
49. Owen, A. J.; Heinzel, J.; Škrbić, Z; Divjaković, V. Crystallization and melting behaviour of PHB and PHB/HV copolymer. *Polymer* **1992**, 33, 1563–1567.
50. Xing, P.; Dong, L.; An, Y.; Feng, Z.; Avella, M.; Martuscelli, E. Miscibility and Crystallization of Poly(β-hydroxybutyrate) and Poly(p-vinylphenol) Blends. *Macromolecules* **1997**, 30, 2726–2733.
51. Liu, J.; Jungnickel, B. J. Crystallization and morphology of poly(vinylidene fluoride)/poly(3-hydroxybutyrate) blends. II. Morphology and crystallization kinetics by time resolved X-ray scattering. *J. Polym. Sci. Part B: Polym. Phys.* **2004**, 42, 974–985.
52. Sato, H.; Suttiwijitpukdee, N.; Hashimoto, T.; Ozaki, Y. Simultaneous Synchrotron SAXS/WAXD Study of Composition Fluctuations, Cold-Crystallization, and Melting in Biodegradable Polymer Blends of Cellulose Acetate Butyrate and Poly(3-hydroxybutyrate). *Macromolecules* **2012**, 45, 2783–2795.
53. Huang, H.; Hu, Z.; Chen, Y.; Zhang, F.; Gong, Y.; He, T.; Wu, C. Effects of Casting Solvents on the Formation of Inverted Phase in Block Copolymer Thin Films. *Macromolecules* **2004**, 37, 6523–6530.
54. Gong, Y.; Huang, H.; Hu, Z.; Chen, Y.; Chen, D.; Wang, Z.; He, T. Inverted to Normal

Phase Transition in Solution-Cast Polystyrene-Poly(methyl methacrylate) Block Copolymer Thin Films. *Macromolecules* **2006**, 39, 3369–3376.

55. Heinzer, M. J.; Han, S.; Pople, J. A.; Baird, D. G.; Martin, S. M. In Situ Measurement of Block Copolymer Ordering Kinetics during the Drying of Solution-Cast Films Using Small-Angle X-ray Scattering. *Macromolecules* **2012**, 45, 3471–3479.
56. Heinzer, M. J.; Han, S.; Pople, J. A.; Baird, D. G.; Martin, S. M. In Situ Tracking of Microstructure Spacing and Ordered Domain Compression during the Drying of Solution-Cast Block Copolymer Films Using Small-Angle X-ray Scattering. *Macromolecules* **2012**, 45, 3480–3486.
57. Siracusa, V.; Lotti, N.; Munari, A.; Dalla Rosa, M. Poly(butylene succinate) and poly(butylene succinate-co-adipate) for food packaging applications: Gas barrier properties after stressed treatments. *Polym. Degrad. Stab.* **2015**, 119, 35–45.
58. Someya, Y.; Sugahara, Y.; Shibata, M. Nanocomposites based on poly(butylene adipate-co-terephthalate) and montmorillonite. *J. Appl. Polym. Sci.* **2005**, 95, 386–392.
59. Brunner, C. T.; Baran, E. T.; Pinho, E. D.; Reis, R. L.; Neves, N. M. Performance of biodegradable microcapsules of poly(butylene succinate), poly(butylene succinate-co-adipate) and poly(butylene terephthalate-co-adipate) as drug encapsulation systems. *Colloid. Surface. B* **2011**, 84, 498–507.
60. Gan, Z.; Abe, H. Temperature-Induced Polymorphic Crystals of Poly (butylene adipate). *Macromol. Chem. Phys.* **2002**, 203, 2369–2374.
61. Pouget, E.; Almontassir, A.; Casas, M. T.; Puiggalí J. On the Crystalline Structures of Poly(tetramethylene adipate). *Macromolecules* **2003**, 36, 698–705.
62. Gan, Z.; Kuwabara, K.; Abe, H.; Iwata, T.; Doi, Y. Metastability and Transformation of Polymorphic Crystals in Biodegradable Poly(butylene adipate). *Biomacromolecules* **2004**, 5, 371–378.
63. Iwata, T.; Kobayashi, S.; Tabata, K.; Yonezawa, N.; Doi, Y. Crystal Structure, Thermal Behavior and Enzymatic Degradation of Poly(tetramethylene adipate) Solution-Grown Chain-Folded Lamellar Crystals. *Macromol. Biosci.* **2004**, 4, 296–307.
64. Gan, Z.; Kuwabara, K.; Abe, H.; Iwata, T.; Doi, Y. The role of polymorphic crystal structure and morphology in enzymatic degradation of melt-crystallized poly(butylene adipate) films.

Polym. Degrad. Stab. **2005**, 87, 191–199.

65. Wu, M. C.; Woo, E. M. Effects of α-form or β-form nuclei on polymorphic crystalline morphology of poly(butylene adipate). *Polym. Int.* **2005**, 54, 1681–1688.
66. Noguchi, K.; Kondo, H.; Ichikawa, Y.; Okuyama, K.; Washiyama, J. Molecular and crystal structure of poly(tetramethylene adipate) α form based on synchrotron X-ray fiber diffraction. *Polymer* **2005**, 46, 10823–10830.
67. Zhao, L.; Wang, X.; Li, L.; Gan, Z. Structural analysis of poly(butylene adipate) banded spherulites from their biodegradation behavior. *Polymer* **2007**, 48, 6152–6161.
68. Woo, E. M.; Chang, C.; Wu, M. C. A new crystal morphology of straight-stalk dendrites in blends of poly(butylene adipate) with amorphous poly(vinyl acetate). *Mater. Lett.* **2007**, 61, 3542–3546.
69. Yan, C.; Zhang, Y.; Hu, Y.; Ozaki, Y.; Shen, D.; Gan, Z.; Yan, S.; Takahashi, I. Melt Crystallization and Crystal Transition of Poly(butylene adipate) Revealed by Infrared Spectroscopy. *J. Phys. Chem. B* **2008**, 112, 3311–3314.
70. Frömsdorf, A.; Woo, E. M.; Lee, L.; Chen, Y.; Förster, S. Atomic Force Microscopy Characterization and Interpretation of Thin-Film Poly(butylene adipate) Spherulites with Ring Bands. *Macromol. Rapid Commun.* **2008**, 29, 1322–1328.
71. Woo, E. M.; Yen, K. C.; Wu, M. C. Analysis of multiple melting behavior of spherulites comprising ring-band shell/ringless core in polymorphic poly(butylene adipate). *J. Polym. Sci. Part B: Polym. Phys.* **2008**, 46, 892–899.
72. Yang, J.; Li, Z.; Pan, P.; Zhu, B.; Dong, T.; Inoue, Y. Temperature-dependent polymorphic crystalline structure and melting behavior of poly(butylene adipate) investigated by time-resolved FTIR spectroscopy. *J. Polym. Sci. Part B: Polym. Phys.* **2009**, 47, 1997–2007.
73. Liu, J.; Ye, H.; Xu, J.; Guo, B. Formation of ring-banded spherulites of α and β modifications in Poly(butylene adipate). *Polymer* **2011**, 52, 4619–4630.
74. Wang, L.; Lugito, G.; Woo, E. M.; Wang, Y. Phase behavior, polymorphism and spherulite morphology in Poly(1, 4-butylene adipate) interacting with two structurally similar acrylic polymers. *Polymer* **2012**, 53, 3815–3826.
75. Weng, M.; He, Y.; Qiu, Z. Effect of Uracil on the Isothermal Melt Crystallization Kinetics and Polymorphic Crystals Control of Biodegradable Poly(butylene adipate). *Ind. Eng. Chem.*

Res. **2012**, 51, 13862–13868.

76. Li, Q.; Zhou, J.; Chai, L.; Memon, J.; Ren, Z.; Li, H.; Sun, X.; Yan, S. The effect of the poly(vinyl phenol) sublayer on the melting behavior of poly(butylene adipate) crystals. *Polym. Chem.* **2014**, 5, 4293–4303.
77. Song, Y.; Ye, H.; Xu, J.; Hou, K.; Zhou, Q.; Lu, G. Stretch-induced bidirectional polymorphic transformation of crystals in poly(butylene adipate). *Polymer* **2014**, 55, 3054–3061.
78. Yang, J.; Chen, Y.; Qin, S.; Liu, J.; Bi, C.; Liang, R.; Dong, T.; Feng, X. Effects of Cyanuric Acid on Crystallization Behavior, Polymorphism, and Phase Transition of Poly(butylene adipate). *Ind. Eng. Chem. Res.* **2015**, 54, 8048–8055.
79. Mi, C.; Zhou, J.; Ren, Z.; Li, H.; Sun, X.; Yan, S. The phase transition behavior of poly(butylene adipate) in the nanoporous anodic alumina oxide. *Polym. Chem.* **2016**, 7, 410–417.
80. Sun, X.; Fang, Q.; Li, H.; Ren, Z.; Yan, S. Effect of Anodic Alumina Oxide Pore Diameter on the Crystallization of Poly(butylene adipate). *Langmuir* **2016**, 32, 3269–3275.
81. Fuller, C. S.; Erickson, C. L. An X-ray study of some linear polyesters. *J. Am. Chem. Soc.* **1937**, 59, 344–351.
82. Fuller, C. S.; Frosch, C. J. Further Investigation of the Chain Structure of Linear Polyesters. *J. Phys. Chem.* **1939**, 43, 323–334.
83. Fuller, C. S.; Frosch, C. J. X-ray investigation of the decamethylene series of polyesters. *J. Am. Chem. Soc.* **1939**, 61, 2575–2580.
84. Minke, R.; Blackwell, J. Polymorphic structures of poly(tetramethylene adipate). *J. Macromol. Sci., Part B: Phys.* **1979**, 16, 407–417.
85. Minke, R.; Blackwell, J. Single crystals of poly(tetramethylene adipate). *J. Macromol. Sci., Part B: Phys.* **1980**, 18, 233–255.
86. Sun, X.; Pi, F.; Zhang, J.; Takahashi, I.; Wang, F.; Yan, S.; Ozaki, Y. Study on the Phase Transition Behavior of Poly(butylene adipate) in its Blends with Poly(vinyl phenol). *J. Phys. Chem. B* **2011**, 115, 1950–1957.
87. Ratri, P. J.; Tashiro, K. Phase-transition behavior of a crystalline polymer near the melting point: case studies of the ferroelectric phase transition of poly(vinylidene fluoride) and the

β-to-α transition of trans-1, 4-polyisoprene. *Polym. J.* **2013**, 45, 1107–1114.

88. Tashiro, K., Measurement of the Physical Characteristics of Polymers by Vibrational Spectroscopy. Chalmers, J. M.; Griffiths, P. R., Chalmers, J. M.; Griffiths, P. R., Eds.; *Handbook of Vibrational spectroscopy*; John Wiley & Sons, Ltd: Chichester, 2002.
89. Crist, B.; Schultz, J. M. Polymer spherulites: A critical review. *Prog. Polym. Sci.* **2016**, 56, 1–63.
90. Shtukenberg, A. G.; Punin, Y. O.; Gunn, E.; Kahr, B. Spherulites. *Chem. Rev.* **2012**, 112, 1805–1838.
91. Gránásy, L.; Pusztai, T.; Tegze, G.; Warren, J. A.; Douglas, J. F. Growth and form of spherulites. *Phys. Rev. E* **2005**, 72, 011605.
92. Fu, Q.; Heck, B.; Strobl, G.; Thomann, Y. A Temperature-and Molar Mass-Dependent Change in the Crystallization Mechanism of Poly(1-butene): Transition From Chain-Folded to Chain-Extended Crystallization? *Macromolecules* **2001**, 34, 2502–2511.
93. Yamashita, M.; Hoshino, A.; Kato, M. Isotactic poly(butane-1) trigonal crystal growth in the melt. *J. Polym. Sci. Part B: Polym. Phys.* **2007**, 45, 684–697.
94. Yamashita, M. Regime II–III transition in isotactic polybutene-1 tetragonal crystal growth. *Polymer* **2014**, 55, 733-737.
95. Cavallo, D.; Gardella, L.; Portale, G.; Müller, A. J.; Alfonso, G. C. Kinetics of Cross-Nucleation in Isotactic Poly(1-butene). *Macromolecules* **2014**, 47, 870–873.
96. Hu, J.; Tashiro, K. Time-Resolved Imaging of the Phase Transition in the Melt-Grown Spherulites of Isotactic Polybutene-1 as Detected by the Two-Dimensional Polarized IR Imaging Technique. *J. Phys. Chem. B* **2016**, 120, 4689–4698.
97. Lotz, B.; Cheng, S. Z. D. A critical assessment of unbalanced surface stresses as the mechanical origin of twisting and scrolling of polymer crystals. *Polymer* **2005**, 46, 577–610.
98. Ye, H.; Wang, J.; Tang, S.; Xu, J.; Feng, X.; Guo, B.; Xie, X.; Zhou, J.; Li, L.; Wu, Q.; Chen, G. Surface Stress Effects on the Bending Direction and Twisting Chirality of Lamellar Crystals of Chiral Polymer. *Macromolecules* **2010**, 43, 5762–5770.
99. Umemoto, S.; Kobayashi, N.; Okui, N. Molecular weight dependence of crystal growth rate and its degree of supercooling effect. *J. Macromol. Sci., Part B* **2002**, 41, 923–938.
100. Umemoto, S.; Okui, N. Power law and scaling for molecular weight dependence of crystal

growth rate in polymeric materials. *Polymer* **2005**, 46, 8790–8795.

101. Barham, P. J.; Keller, A.; Otun, E. L.; Holmes, P. A. Crystallization and morphology of a bacterial thermoplastic: poly-3-hydroxybutyrate. *J. Mater. Sci.* **1984**, 19, 2781–2794.
102. Woo, E. M.; Wu, P. L.; Wu, M. C.; Yan, K. C. Thermal Behavior of Ring-Band versus Maltese-Cross Spherulites: Case of Monomorphic Poly(ethylene adipate). *Macromol. Chem. Phys.* **2006**, 207, 2232–2243.
103. Kajioka, H.; Taguchi, K.; Toda, A. Cellular Crystallization in Thin Melt Film of it-Poly(butene-1): An Implication to Spherulitic Growth From Bulk Melt. *Macromolecules* **2011**, 44, 9239–9246.
104. Chen, M.; Chen, C.; Ke, K.; Ho, R. Regime crystallization and banded spherulite of poly(trimethylene terephthalate). *J. Macromol. Sci., Part B* **2002**, 41, 1063–1078.
105. Nurkhamidah, S.; Woo, E. M. Unconventional Non-birefringent or Birefringent Concentric Ring-Banded Spherulites in Poly(L-lactic acid) Thin Films. *Macromol. Chem. Phys.* **2013**, 214, 673–680.
106. Woo, E. M.; Lugito, G. Origins of periodic bands in polymer spherulites. *Eur. Polym. J.* **2015**, 71, 27–60.
107. Woo, E.; Lugito, G. Cracks in Polymer Spherulites: Phenomenological Mechanisms in Correlation with Ring Bands. *Polymers* **2016**, 8, 329.
108. Keith, H. D.; Padden, F. J. Banding in Polyethylene and Other Spherulites. *Macromolecules* **1996**, 29, 7776–7786.
109. Toda, A.; Okamura, M.; Taguchi, K.; Hikosaka, M.; Kajioka, H. Branching and Higher Order Structure in Banded Polyethylene Spherulites. *Macromolecules* **2008**, 41, 2484–2493.
110. Schultz, J. M. Self-induced field model for crystal twisting in spherulites. *Polymer* **2003**, 44, 433–441.
111. Wang, Z.; Li, Y.; Yang, J.; Gou, Q.; Wu, Y.; Wu, X.; Liu, P.; Gu, Q. Twisting of Lamellar Crystals in Poly(3-hydroxybutyrate-co-3-hydroxyvalerate) Ring-Banded Spherulites. *Macromolecules* **2010**, 43, 4441–4444.
112. Lan, Q.; Yu, J.; Zhang, J.; He, J. Direct formation of banded spherulites in poly(l-lactide) from the glassy state: Unexpected synergistic role of chain structure and compressed CO_2. *Polymer* **2016**, 99, 662–670.

113. Hikima, Y.; Morikawa, J.; Hashimoto, T. Wavenumber Dependence of FT-IR Image of Molecular Orientation in Banded Spherulites of Poly(3-hydroxybutyrate) and Poly(L-lactic acid). *Macromolecules* **2013**, 46, 1582–1590.

114. Beekmans, L.; Hempenius, M. A.; Vancso, G. J. Morphological development of melt crystallized poly(propylene oxide) by in situ AFM: formation of banded spherulites. *Eur. Polym. J.* **2004**, 40, 893–903.

115. Zhao, L.; Kong, J.; Tian, X.; Zhang, J.; Qin, S. Isothermal crystallization of poly(L-lactide) and poly(butylene adipate) crystalline/crystalline blends. *Polym. J.* **2014**, 46, 323–329.

116. Sasic, S.; Ozaki, Y.; Eds.; *Raman, infrared, and near-infrared chemical imaging*; John Wiley & Sons, Inc.: Hoboken, NJ, 2011.

117. Snively, C. M.; Koenig, J. L. Application of Real Time Mid-Infrared FTIR Imaging to Polymeric Systems. 1. Diffusion of Liquid Crystals into Polymers. *Macromolecules* **1998**, 31, 3753–3755.

118. Snively, C. M.; Koenig, J. L. Fast FTIR imaging: A new tool for the study of semicrystalline polymer morphology. *J. Polym. Sci. Part B: Polym. Phys.* **1999**, 37, 2353–2359.

119. Ribar, T.; Bhargava, R.; Koenig, J. L. FT-IR Imaging of Polymer Dissolution by Solvent Mixtures. 1. Solvents. *Macromolecules* **2000**, 33, 8842–8849.

120. Ribar, T.; Koenig, J. L.; Bhargava, R. FTIR Imaging of Polymer Dissolution. 2. Solvent/Nonsolvent Mixtures. *Macromolecules* **2001**, 34, 8340–8346.

121. Kazarian, S. G.; Chan, K. A. FTIR Imaging of Polymeric Materials Under High-Pressure Carbon Dioxide. *Macromolecules* **2004**, 37, 579–584.

122. Vogel, C.; Wessel, E.; Siesler, H. W. FT-IR Spectroscopic Imaging of Anisotropic Poly(3-hydroxybutyrate)/Poly(lactic acid) Blends with Polarized Radiation. *Macromolecules* **2008**, 41, 2975–2977.

123. Vogel, C.; Wessel, E.; Siesler, H. W. FT-IR Imaging Spectroscopy of Phase Separation in Blends of Poly(3-hydroxybutyrate) with Poly(L-lactic acid) and Poly(ε-caprolactone). *Biomacromolecules* **2008**, 9, 523–527.

124. Unger, M.; Morita, S.; Sato, H.; Ozaki, Y.; Siesler, H. W. Variable-Temperature Fourier Transform Infrared Spectroscopic Investigations of Poly(3-Hydroxyalkanoates) and Perturbation-Correlation Moving-Window Two-Dimensional Correlation Analysis. Part I:

Study of Non-Annealed and Annealed Poly(3-Hydroxybutyrate) Homopolymer. *Appl. Spectrosc.* 2009, 63, 1027–1033.

125. Unger, M.; Sedlmair, J.; Siesler, H. W.; Hirschmugl, C. 3D FT-IR imaging spectroscopy of phase-separation in a poly(3-hydroxybutyrate)/poly(L-lactic acid) blend. *Vib. Spectrosc.* **2014**, 75, 169–172.
126. Hikima, Y.; Morikawa, J.; Hashimoto, T. FT-IR Image Processing Algorithms for In-Plane Orientation Function and Azimuth Angle of Uniaxially Drawn Polyethylene Composite Film. *Macromolecules* **2011**, 44, 3950–3957.
127. Hikima, Y.; Morikawa, J.; Hashimoto, T. Imaging of Two-Dimensional Distribution of Molecular Orientation in Poly(ethylene oxide) Spherulite Using IR Spectrum and Birefringence. *Macromolecules* **2012**, 45, 8356–8362.
128. Schaeberle, M. D.; Karakatsanis, C. G.; Lau, C. J.; Treado, P. J. Raman Chemical Imaging: Noninvasive Visualization of Polymer Blend Architecture. *Anal. Chem.* **1995**, 67, 4316–4321.
129. Fernandez, M. R.; Merino, J. C.; Gobernado-Mitre, M. I.; Pastor, J. M. Molecular and Lamellar Orientation of α-and β-Transcrystalline Layers in Polypropylene Composites by Polarized Confocal Micro-Raman Spectroscopy: Raman Imaging by Static Point Illumination. *Appl. Spectrosc.* **2000**, 54, 1105–1113.
130. van Apeldoorn, A. A.; Van Manen, H.; Bezemer, J. M.; de Bruijn, J. D.; van Blitterswijk, C. A.; Otto, C. Raman Imaging of PLGA Microsphere Degradation Inside Macrophages. *J. Am. Chem. Soc.* **2004**, 126, 13226–13227.
131. Huan, S.; Lin, W.; Sato, H.; Yang, H.; Jiang, J.; Ozaki, Y.; Wu, H.; Shen, G.; Yu, R. Direct characterization of phase behavior and compatibility in PET/HDPE polymer blends by confocal Raman mapping. *J. Raman Spectrosc.* **2007**, 38, 260–270.
132. Chernenko, T.; Matthäus, C.; Milane, L.; Quintero, L.; Amiji, M.; Diem, M. Label-Free Raman Spectral Imaging of Intracellular Delivery and Degradation of Polymeric Nanoparticle Systems. *Acs Nano* **2009**, 3, 3552–3559.
133. Martin, J.; Bourson, P.; Dahoun, A.; Hiver, J. M. The β-spherulite Morphology of Isotactic Polypropylene Investigated by Raman Spectroscopy. *Appl. Spectrosc.* **2009**, 63, 1377–1381.

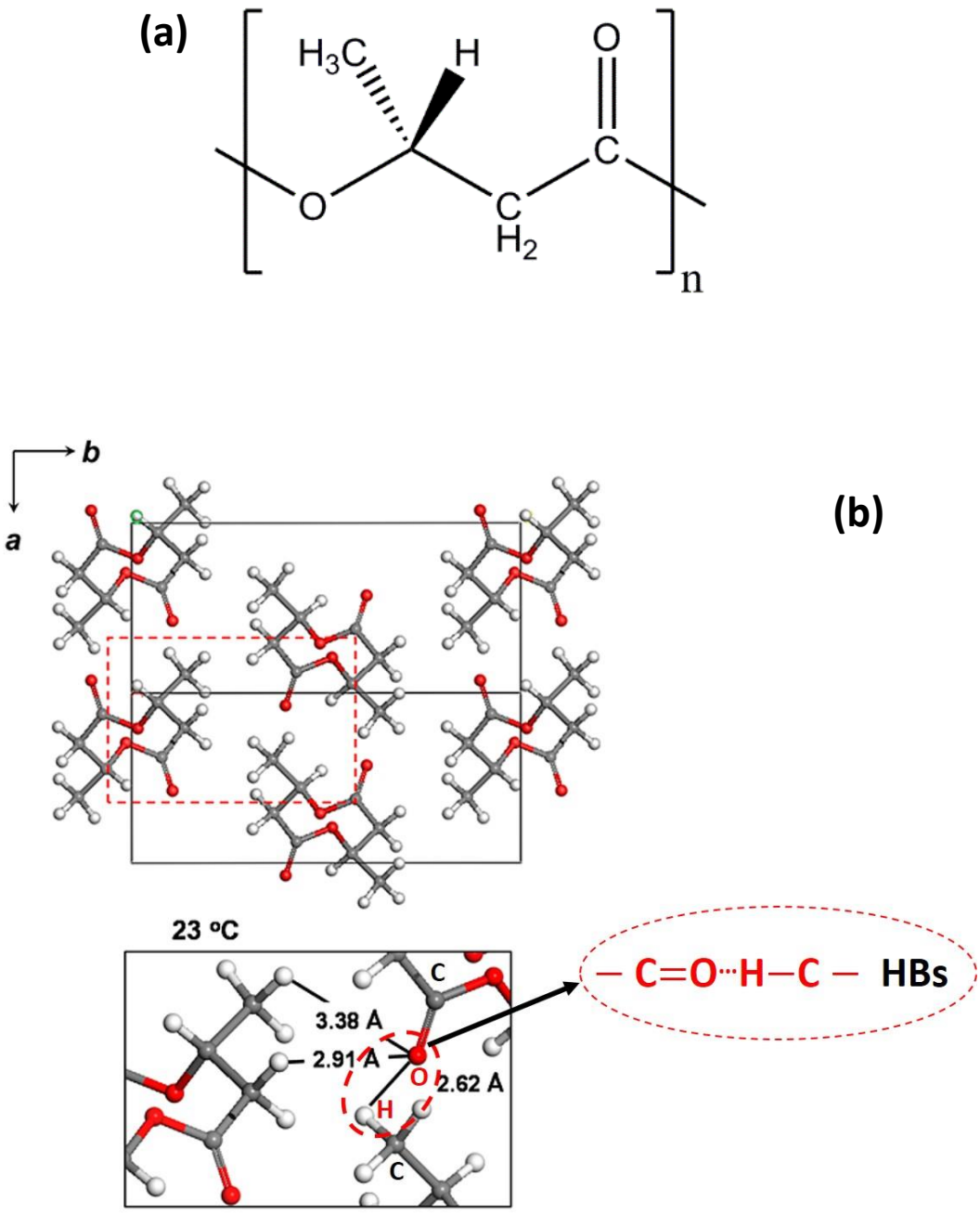

Figure 1. The chemical structure of PHB (a) and the α-form crystal structure of PHB with HBs (b) ((b) is reproduced from ref 29 with permission. Copyright 2016 American Chemical Society).

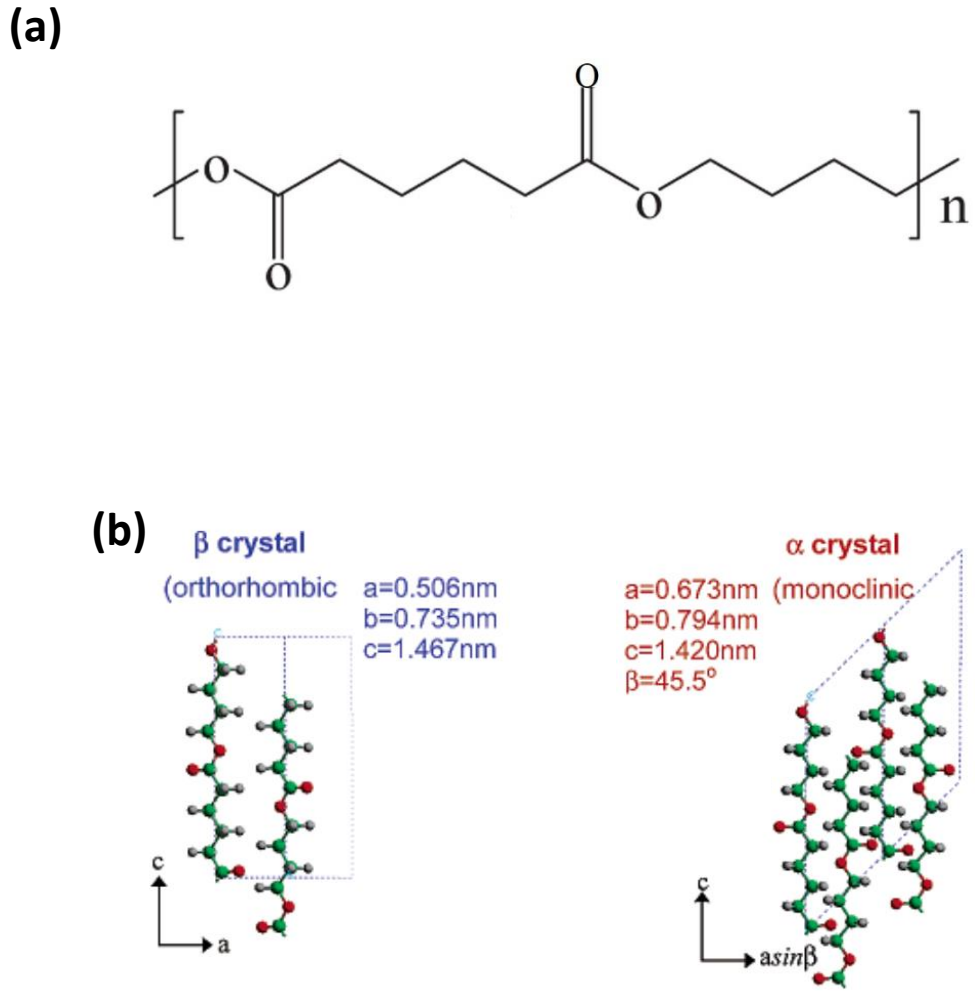

Figure 2. The chemical structure of PBA (a) and the α- and β-form crystal structure of PBA (b) ((b) is reproduced from ref 62 with permission. Copyright 2004 American Chemical Society).

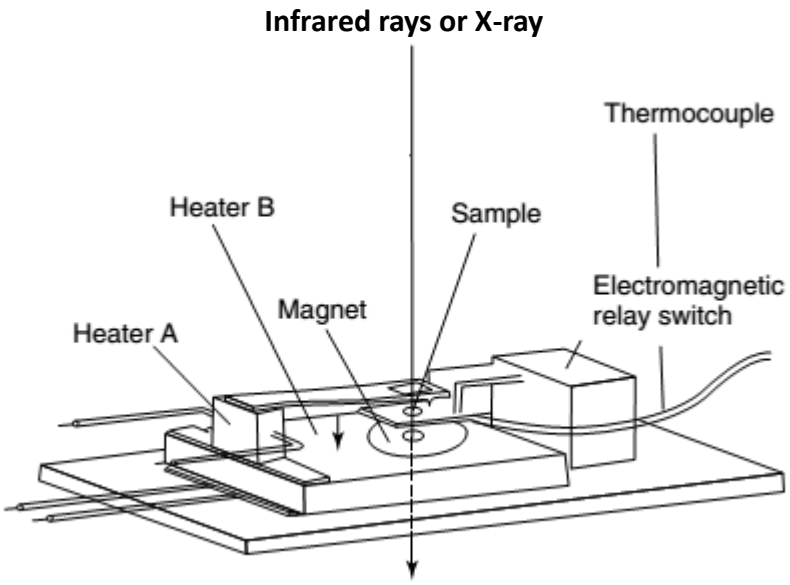

Figure 3. Illustration of temperature jump cell for time-resolved FTIR and WAXD/SAXS measurements (Reproduced from ref 88 with permission. Copyright 2002 John Wiley & Sons).

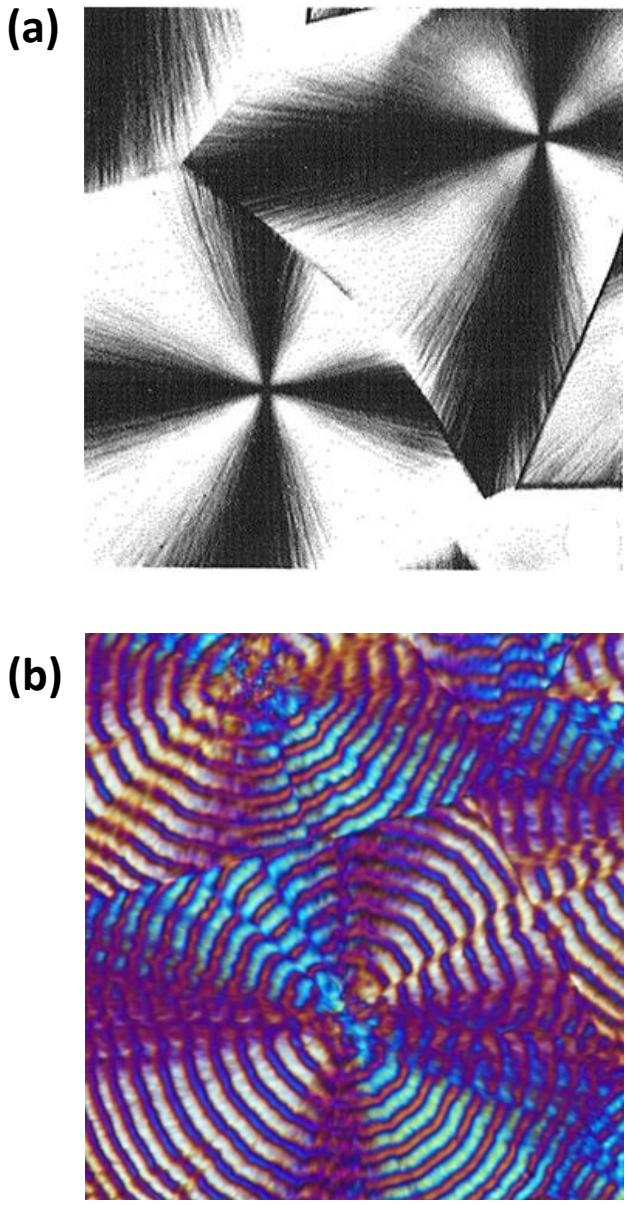

Figure 4. Dark Maltese cross pattern of the typical spherulite (a) (Reproduced from ref 89 with permission. Copyright 2015 Elsevier Ltd.) and the typical ring-banded spherulite (b).

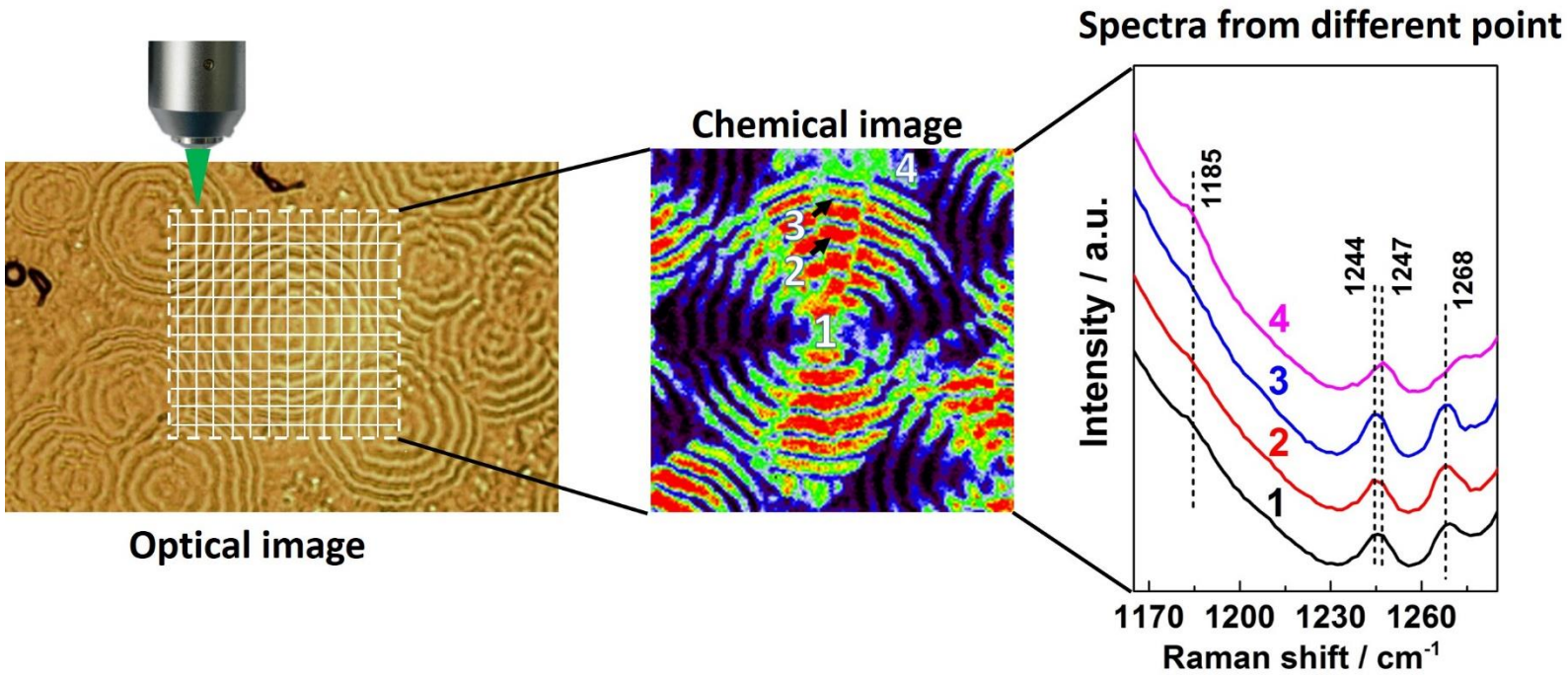

Figure 5. Schematic of chemical imaging technique

Chapter 1

Higher-Order Structure Formation of a Poly(3-hydroxybutyrate) Film during Solvent Evaporation

ABSTRACT

Solvent evaporation crystallization (SEC) of poly(3-hydroxybutyrate) (PHB) in a PHB/chloroform solution was investigated by time-resolved attenuated total reflection Fourier-transform infrared (ATR-FTIR) spectroscopy and grazing incidence wide angle X-ray diffraction (GI-WAXD). The ATR-FTIR investigation reveals that the PHB/chloroform solution was in a homogeneous state at first, and with the evaporation of chloroform, the separated PHB from the chloroform solvent was in the mixture of intermediate and amorphous states, but no crystal structure formed due to the presence of chloroform. Subsequently, further evaporation induced a transition from intermediate to crystal structure and the formation of C=O···H−C intramolecular interactions within the latter. As the crystal structure developed, the intra-molecular interaction changed from weak to strong due to the reduced intra-molecular distance within the lamella structure. The results of the GI-WAXD investigation suggest the presence of two kinds of intermediate structures with different order (less ordered and highly ordered). During SEC, the intermediate structures formed first, subsequently transforming into a crystal structure.

Introduction

Crystallization is the most important step during crystal structure formation of semicrystalline polymers.[1–5] For polymer materials, a crystalline state is a highly stable state with low free energy. Different crystallization pathways can yield different crystal structures, which is reflected in the polymorphic behavior of polymers. For example, poly(L-lactic acid) (PLA) has four different crystalline modifications (α, α', β, γ); the α and α' forms are obtained by crystallization from amorphous states at temperatures higher and lower than 120 ℃,[6,7] respectively, while the β and γ forms are prepared using a high draw ratio at high temperature and epitaxial crystallization,[8-11] respectively. The formation of final crystal structure involves the transformation of the molecular chain package from an amorphous state to a crystalline state. During this process, the molecular structure passes many states since long molecular chains are highly entangled,[12] and every macromolecular chain has to pass selections on different length and time scales.[13,14] Therefore, investigations of structural changes during crystallization are very important for understanding the growth mechanism of polymer polymorphisms.

Being different from crystallization from pure polymers system, such as cold and melt crystallization, solvent evaporation crystallization (SEC) is in general more complex.[15–21] For a polymer solution, the solvent molecules usually exhibit some interactions with polymer chains,[22] and phase separation occurs during solvent evaporation when the concentration reaches a saturation point. A SEC polymer film is usually formed in a very short time, so that *in situ* synchrotron radiation X-ray has usually been used to investigate this process.[16,19,20,23–25]

Heinzer et al.[23] studied the spacing change of hexagonally packed cylinders in a poly(styrene-*b*-butadiene) copolymer film during solvent drying by *in situ* grazing incidence small-angle X-ray scattering (GI-SAXS) measurements. They found that the above spacing increases on solvent evaporation, with the segregation of blocks increasing first. When the solution concentration reaches a critical point, the spacing decreases due to the loss of solvent. Using same method, Ogawa et al.[24] studied the structural development of symmetric poly(styrene-*b*-2-vinylpyridine) block copolymers thin films during spin-coating. They suggested that the microstructure of poly(styrene-*b*-2-vinylpyridine) is first created from randomly distributed spherical micelles forming a body-centered cubic (BCC) lattice, with further evaporation inducing a transition from

spheres in the BCC lattice to cylindrical structures.

Compared to X-ray analysis, it is well known that Fourier-transform infrared (FTIR) spectroscopy is more suitable for investigating the conformational and local molecular environments changes of polymers.[26–28] Therefore, time-resolved FTIR spectroscopy has been extensively used to investigate the crystallization of semicrystalline polymers.[7,29–31] However, to ensure better signal-to-noise ratio (SNR), IR spectra are usually obtained using 64 or 128 scans at 2–4 cm^{-1} resolution. Thus, it takes about 1–2 min to obtain one spectrum. Therefore, FTIR investigations of solvent evaporation crystallization are difficult. Due to this limitation, to the best of our knowledge, no reports on FTIR characterization of SEC exist.

During the last two decades, biodegradable polymers have attracted considerable interest. Among them, poly(3-hydroxybutyrate) (PHB) has been extensively studied,[32–37] since it has mechanical properties similar to those of conventional synthetic polymers.[38–41] The α crystal modification of PHB is the most common form, and its helical chain is packed as an orthorhombic unit cell, $P2_12_12_1$-D^4_2, with dimensions of a = 5.76 Å, b = 13.20 Å, and c = 5.96 Å.[42–44] Based on IR and X-ray crystallographic studies, Sato et al. suggested the existence of weak hydrogen bonding between the carbonyl and methyl groups (C=O···H−C) in the unit cell. The distance between them is 2.62 Å,[44] which is shorter than the sum of van der Waals radii of O and H atoms, 2.72 Å. The FTIR investigation of Sato et al. [45] showed that the asymmetric CH_3 stretching band appears at an abnormally high frequency (3009 cm^{-1}), providing more evidence for the C=O···H−C hydrogen bonding. Very recently, Wang and Tashiro[44] studied the crystal structure and intermolecular interactions of the α-form of PHB in detail, confirming the existence of C=O···H−C hydrogen bonding.

PHB is also a good model for investigating polymer crystallization behavior due to its exceptional purity and low nucleation density.[46,47] Therefore, it was chosen as a candidate to investigate SEC in this work. Until now, studies on the crystallization of PHB have been mainly concerned with melt crystallization (around 110 ℃).[34,37,48] However, no related studies on the cold crystallization of PHB at lower temperature (e.g., room temperature) exist, probably due to the T_g (glass transition temperature) of PHB is relatively low (around 5 ℃) and the cold crystallization of PHB at room temperature is very fast, therefore, it is little bit difficult to carry out such measurement. Therefore, investigating the SEC of PHB is very meaningful. In this research, SEC

studies are carried out at room temperature (25 ℃), even though this temperature is higher than the T_g of PHB, the crystallization from an amorphous state can still be traced very clearly due to the presence of solvent. It should be noticed that by SEC, PHB can form only one kind of crystal structure (α-form) from amorphous state, changing SEC condition will not change the crystallization process and the final crystal structure.

In the present study, the author focus on such two points: (1) the structure change of PHB from molecular level during SEC; (2) the multi molecular interaction change between PHB and chloroform and within PHB crystal structure during SEC. Attenuated total reflection Fourier-transform infrared (ATR-FTIR) spectroscopy was used to investigate the SEC of a PHB/chloroform solution. To overcome the conflict between high IR signal-to-noise ratio and high evaporation rate of chloroform, a glass tube was used to hold the PHB/chloroform solution (Figure 1). This can slow down the evaporation rate due to the reduction of exposed area and increase the chloroform concentration in vapor on the solution surface. Therefore, the PHB/chloroform solution in the glass tube provided enough time for FTIR measurements during SEC. ATR-FTIR spectroscopy can be used to investigate the SEC of the PHB/chloroform solution in detail, especially in terms of the formation of intermediate structures and hydrogen bonding. Moreover, time-resolved *in situ* grazing incidence wide angle X-ray diffraction (GI-WAXD) was also used to support the results of ATR-FTIR.

Experimental Section

Materials and Sample Preparation

Bacterially synthesized PHB with a number-average molecular weight of M_n = 42000 g/mol was purchased from Sigma-Aldrich Chemical Co., Ltd., and was used without further purification. A PHB/chloroform solution was prepared by dissolving PHB powder in hot chloroform at 80 ℃ to produce a homogeneous solution with a concentration of 5 wt.%.

Time-Resolved *In Situ* ATR-FTIR Measurements

Time-resolved *in situ* ATR-FTIR measurement of the PHB/chloroform solution were carried out during SEC using a Thermo Nicolet Magna 6700 Fourier-transform FTIR spectrometer with a liquid nitrogen-cooled mercury-cadmium-telluride (MCT) detector. The IR spectra were collected using a PIKE MIRacle (WI, USA) single reflection ATR cell with a 45 °ZnSe ATR crystal, which was connected to a dry air supply for purging and aligned for the measurements. Figure 1-1 shows a picture (Figure 1-1(a)) and a scheme (Figure 1-1(b)) of the ATR accessories used. A glass tube was used to hold the PHB/chloroform solution in the ATR cell. Each IR spectrum was obtained at room temperature (25 ℃) by co-adding 32 scans at a spectral resolution of 2 cm^{-1}. There was no interval time between the collection of two adjacent spectra. The 0 min point was defined as the time when the addition of the PHB/chloroform solution into the glass tube was finished. The amount of the added solution was about 200 μL, and it took 160 min to complete the SEC of PHB in this experiment. It should be noted that the time required for completing SEC does not have a real physical meaning, since it depends on the amount of solution. Actually, SEC is polymer weight fraction dependent, but it is difficult to simultaneously measure (by gravimetrically method) that change during the spectral measurement, necessitating the use of time instead of polymer weight fraction change.

Time-Resolved *In Situ* GI-WAXD Measurements

Time-resolved *in situ* GI-WAXD measurements were performed using an X-ray diffractometer (Nanoviewer, Rigaku Co., Japan). The system consisted of a rotating anode X-ray generator (Cu K_α, 40 kV, 30 mA) and a specifically designed confocal X-ray mirror with three slit optic collimators and a two-dimensional (2D) detector (Pilatus 100K, Dectris, Switzerland). A Si

(100) wafer was used as a substrate. The SEC of PHB in chloroform was investigated using GI-WAXD by placing a 50 μL drop of the above solution onto the substrate. Each WAXD pattern was acquired using a 5s exposure, with no interval time between subsequent data collections. The angle of incidence was fixed to be 0.19 °, which corresponds to 1.14 times of the critical angle for total reflection (θ_c), indicating that the incident X-way fully illuminate the surface region of the sample as well as the deeply-buried interfacial region. The camera distance was chosen to be 131 mm, allowing the (020) and (110) reflections to be measured simultaneously with sufficient angular resolution.

Results and Discussion

Structure Evolution of PHB during SEC Studied by ATR-FTIR Spectroscopy

Figure 1-2 shows the IR spectra and their second derivatives in the C−H stretching region (a), C=O stretching region (b), and C−Cl stretching region (c) of pure PHB and chloroform. The corresponding assignments are summarized in Table 1-1. Chloroform shows only two bands, at 3020 and 742 cm^{-1} (Figures 1-2(a) and (c)). Attention should be paid to the PHB bands at 1722 and 3009 cm^{-1}, which are characteristic of the crystalline state (Figures 1-2(a) and (b)). The frequency of these bands indicates the existence of C=O···H−C hydrogen bonding in crystalline PHB.[34,44,45] Bands at 1738 and 1748 cm^{-1} are due to the C=O stretching modes of different PHB conformations in the main chain[34,45] or to differently ordered[49] amorphous parts of PHB. The bands at 2974, 2934, and 2874 cm^{-1} are assigned to CH_3, CH_2 asymmetric, and CH symmetric stretching modes in the crystalline region, respectively,[36] while the band at 2998 cm^{-1} exists both in the crystalline and amorphous regions (Figure 1-2(a)).[34] During the crystallization of PHB, these IR bands show sequential changes, which can be used to track the molecular structure change of PHB during SEC.

Figures 1-3(a) and (b) show time-dependent variations of IR spectra in the 3050–2800 and 1770–1680 cm^{-1} regions during the SEC of PHB, respectively. The yellow and blue regions in Figure 1-3(a) stand for the C=O stretching bands of PHB in the amorphous and crystalline regions, respectively. Figure 1-4 shows changes in the amorphous (a) and crystalline (b) C=O stretching bands of the PHB/chloroform solution during SEC. SEC prior to the appearance of the crystal C=O band (1722 cm^{-1}) is discussed first. Based on Figure 1-4(a), the changes in the amorphous PHB C=O stretching band (denoted C=O (amorphous)) can be divided into two regions, depending on the absorbance and wavenumber changes: time range Δt_1, from 0 to 117 min, and time range Δt_2, from 117 to 146 min. In the first time range, the wavenumber and absorbance of C=O (amorphous) do not change much. Chloroform is good solvent for PHB, and it is reasonable to consider that intermolecular interactions exists between PHB molecular chains and chloroform molecules (denoted as *inter*).[50] Jacquel et al.[49] studied the solubility of polyhydroxyalkanoates (PHAs) in different solvents. They found that among tetrachloromethane, chloroform, dichloromethane, and

1,2-dichloroethane, chloroform and dichloromethane exhibited high solubilizing properties for PHAs, while tetrachloromethane and 1,2-dichloroethane exhibited lower solubilizing properties. The carbon atom in solvent molecules with high PHA solubilizing properties should carry at least one chlorine atom and one hydrogen atom. These high solubilizing properties can be explained by a polar interaction between the chloride atom and the carbonyl group carbon, together with the fact that the electron-deficient hydrogen atom of the halogenated compound is linked to the carbonyl group of the polymer [see Figure 4 in ref 50].

Figure 1-5(a) and (b) shows IR spectra of the PHB/chloroform solution in the C=O (amorphous) stretching region and the chloroform CH_3 asymmetric stretching band region during Δt_1, respectively. The absorbance of C=O (amorphous) increases with time due to chloroform evaporation, but the wavenumber remains constant at around 1739 cm^{-1} (Figures 1-4(a) and 5(a)). Similar behavior is also observed for the CH_3 asymmetric stretching band region of chloroform. These results imply that even though the PHB concentration increases due to solvent evaporation, the *inter* changes little. In the other words, the PHB/chloroform solution is still homogenous, and no phase separation takes place.

Time range Δt_2. This time range shows a spectral variation clearly different from that of Δt_1 in terms of both absorbance and wavenumber. It can be seen from Figure 1-4(a) that the wavenumber shows a red shift from 1739 to 1735 cm^{-1}, while the absorbance keeps increasing. These spectral changes can also be seen in the raw spectra (Figure 1-6(a)). It is interesting to note that the changes of absorbance and wavenumber for Δt_2 are not linear, and that there is a sudden increase in absorbance starting from 127 min. After 132 min, the absorbance curve enters another linear change region. Similarly to the absorbance change, the wavenumber also shows a discrete red shift between 127 and 132 min. Therefore, Δt_2 can be divided into three ranges: 117–127, 127–132, and 132 – 146 min. The wavenumber is related to the local chemical environment. For the PHB/chloroform solution during SEC, changes of the latter may be very complex due to the occurring phase separation. Therefore, to investigate the structural changes of PHB in the 117–146 min interval, second derivatives of IR spectra are used, as shown in Figure 1-6(a). Two sudden change points, 127 and 132 min, are indicated by red and blue broken lines, respectively (Figure 1-6(a)).

<1> 117 - 127 min. The second derivative spectrum at 117 min in Figure 1-6(a) features two bands at around 1741 and 1727 cm^{-1}. The former band is due to the C=O (amorphous) of PHB, while the new band at 1727 cm^{-1} is present in neither pure PHB nor pure chloroform spectrum. As discussed above for Δt_1, the solution is still homogeneous, with no phase separation and nucleation taking place. Thus, no crystal structure is formed. Therefore, this new peak of the PHB/chloroform system may reflect *inter* C=O. In the 117–127 min interval, the 1741 cm^{-1} band becomes stronger and is shifted to lower frequency, while the intensity of the 1727 cm^{-1} band slightly increases. The absorbance increase in this range is due to the increase of PHB concentration (Figure 1-5(a)). However, the reason behind the hardly detectable concentration change in the Δt_1 range may be due to the sensitivity of the FTIR instrument, since even though chloroform undergoes extensive evaporation, the solution is still dilute, and the amount of PHB on the surface of the ATR crystal does not change much. Thus, the absorbance of PHB changes little.

<2> 127 - 132 min. In this time range, the absorbance shows an abnormal increase (Figure 1-4(a)). If the solution is still homogeneous, and only the concentration changes, the rate of absorbance increase should be equal to that in the 117–127 min range. Therefore, it is very likely that other processes happen in this time domain. It can be seen from Figure 1-6(a) that in the 127–132 min range a band at around 1731 cm^{-1} gradually becomes more distinct, while the one at 1727 cm^{-1} becomes less distinct. In the spectrum recorded at 132 min, the 1731 cm^{-1} band shows up more clearly. The weaker 1727 cm^{-1} band indicates that the amount of *inter* C=O decreases. In other words, the interaction between chloroform and PHB starts to gradually disappear. This means that the amount of chloroform is not sufficient to completely dissolve PHB. Therefore, PHB starts to separate out from chloroform (phase separation). It is reasonable to speculate that the IR absorbance of PHB separated out from chloroform is stronger than that of PHB in solution. Therefore, the absorbance in Figure 1-4(a) shows a sudden increase from 127 min onwards.

The most interesting finding in this time domain is that a new band appears at 1731 cm^{-1}. Since this band shows up after phase separation occurs, it is not due to the interaction between PHB and chloroform. In our previous research, the author also observed the 1731 cm^{-1} band during the isothermal crystallization of PHB from melt.[34,48] This band was assigned to an intermediate structure between the amorphous and crystalline states of PHB following the concept proposed by

Strobl[51], since the intensity of the 1731 cm^{-1} band tends to decrease as the intensity of the crystalline band around 1722 cm^{-1} increases. The results in Figure 1-6(b) show that the intensity of the 1731 cm^{-1} band decreases, while that of the crystalline band at 1722 cm^{-1} increases, which is similar to the results of previous studies.[34,48] Therefore, the author assign the 1731 cm^{-1} band to the intermediate structure. However, contrary to the previous results, the 1731 cm^{-1} band (e.g., in the spectrum at 132 min) does not appear simultaneously with the 1722 cm^{-1} band.

It should be noted that the so-called crystalline band of PHB at 1722 cm^{-1} is the crystalline C=O stretching band featuring intramolecular interactions (denoted *intra*) within PHB, and this band starts to appear just after secondary crystallization. During the introduction period, only the 1732 cm^{-1} band (due to the C=O stretching mode without *intra*) shows complex change.[48] Therefore, studying the intermediate structure of PHB is very important for understanding the crystallization process. However, the isolated intermediate structure is difficult to form during melt crystallization of bulk PHB, since the crystal with *intra* has a lower energy than the intermediate state, and the transformation of the latter into the former is very fast and spontaneous. However, in the present study, the intermediate state is relativity stable during SEC. This may be due to the presence of chloroform solvent, which weakly interacts with PHB to loosen the crystal structure of the latter. In other words, the distance between CH_3 and C=O groups in the molecular chain of PHB may become longer than the van der Waals separation between the O and H atoms (2.72 Å), thus excluding the formation of *intra*. Therefore, only the amorphous and intermediate structures appear before *intra*.

<3> 132 - 146 min. In this time domain, the increase in absorbance becomes slower than in the 127–132 min interval. Since the latter is a transition region between the 117–127 min and 132–146 min intervals, complex changes (e.g., phase separation) start to happen between 127–132 min. Therefore, the absorbance increase is faster between 127–132 min than between 117–127 min and 132–146 min. A similar trend is also observed for the wavenumber changes. Figure 1-6(a) reveals that the 1731 cm^{-1} band becomes stronger in the 132–146 min interval, and that the 1739 cm^{-1} band shows no frequency shift compared to the 117–127 min and 127–132 min intervals. However, the intensity of the 1727 cm^{-1} band continually decreases. This information indicates that the phase separation continues with the evaporation of chloroform in the 132–146 min region, but the rate of phase separation is lower than that in the 127–132 min interval, since most of the PHB has

already separated out between 127–132 min. However, chloroform can still affect the structure of PHB, and the crystal structure with *intra* does not appear.

The 1722 cm^{-1} band starts to appear from 146.5 min, as shown in Figure 1-6(b). The absorbance and wavenumber changes between 147.5–160 min are shown in Figure 1-4(b) (since the absorbance at 146.5 and 147 min are difficult to read from the raw IR spectra, the absorbance in Figure 1-4(b) is plotted starting from 147.5 min). The crystallization process is almost complete after 153 min, as shown by the black broken dotted line in Figure 1-4(b). Figure 1-4(b) shows that the wavenumber is shifted to lower frequency (from 1722 to 1720 cm^{-1}), accompanied by an increase of absorbance intensity between 146.5–153 min. This change can also be seen from the second derivative spectra in this time domain, as shown in Figure 1-7. The low frequency shift of the 1722 cm^{-1} band is due to the *intra* becoming stronger during crystallization. This behavior is easy to understand, since the formation of *intra* involves the creation of C=O···H−C hydrogen bonds in PHB, where the distance between the crystal lattice planes is becoming shorter. With closer packing of the crystal lattice planes, the distance between the C=O and CH_3 groups becomes shorter, so that *intra* becomes stronger during 146.5–153 min.

The IR and corresponding second-derivative spectra of the 3040–2950 cm^{-1} CH stretching region during SEC in the 146.5–153 min interval are shown in Figure 1-8. The three bands at 3008, 2997, and 2976 cm^{-1} are assigned to the CH_3 asymmetric stretching modes of PHB,[34] with their intensities increasing concomitantly with that of the 1722 cm^{-1} band (Figure 1-7). The 3008 cm^{-1} band is due to the weak C=O···H−C hydrogen bonds[44] and shows a shift to higher frequency from 3008 to 3010 cm^{-1}, presenting additional evidence of the *intra* becoming stronger during SEC.

Structure Evolution of PHB during SEC Studied by Time-Resolved *In Situ* GI-WAXD

Time-resolved *in situ* GI-WAXD was used in the present study to support the results of ATR-FTIR. Since GI-WAXD measurements cannot employ the glass tube used in the latter measurements for lowering the evaporate rate of chloroform, a PHB/chloroform solution was directly dropped on a Si substrate, letting the solvent evaporate at room temperature. Subsequently, GI-WAXD measurements were carried out.

Time-resolved evolution of two-dimensional GI-WAXD patterns during SEC of the PHB/chloroform solution is shown in Figure 1-9. No diffraction pattern of PHB is observed before

50 s, and the diffraction profile of crystalline PHB appears after 55 s (not always clear in the 2D pattern in Figure 1-9, see Figure 1-10(a)). The diffraction arcs of the (020) and (110) lattice planes of PHB[44] become more distinct with the evaporation of chloroform starting from 75 s (as shown by the white arrows in Figure 1-9(c)). Since each diffraction arc is continuous, there is no preferred orientation within the film. Time-resolved GI-WAXD profiles of the (020) reflection during SEC between 0–300 s integrated from 2D diffraction patterns are shown in Figure 1-10(a). It can be seen from the latter figure that the diffraction profiles are very broad and unsymmetrical, implying the presence of more than one diffraction peak.

To quantitatively investigate the SEC of PHB, diffraction profiles of the (020) reflection were deconvoluted assuming a Gaussian shape of the underlying peaks. Figures 1-10(b) and (c) depict two typical curve fitting results of the diffraction profiles at 75 and 100 s, respectively. Four peaks are present at $2\theta \approx 12.96°$, $13.21°$, $13.68°$ and $14.21°$. The diffraction arc at $2\theta \approx 14.21°$, indicated by the black arrow in Figure 1-10(a), is clearly separated from the (020) diffraction arc, as can be seen in Figure 1-10(d). Therefore the above ghost peak does not arise from the (020) lattice plane and necessitates future research. It is very interesting that three peaks overlap in the (020) diffraction region, with their relative intensity also changing during SEC. From the relative intensity change and diffraction angle, it is reasonable to assign the peak at $2\theta \approx 13.68°$ to the crystalline PHB. Meanwhile, the intensities of the other two diffraction peaks at $2\theta \approx 12.96°$ and $13.21°$ decrease with time. Their lattice plane distance is slightly larger than the one of the crystal structure, so it is reasonable to assign them to intermediate structures. Very recently, Khasanah et al.[50] found that ultra-thin PHB films contain stable intermediate structures, and the GI-WAXD diffraction profile of the (020) lattice plane is overlapped by two peaks, assigned to the intermediate and highly-ordered structures.

The two kinds of intermediate structure observed in this study may also be due to their different order (the reason why only one intermediate structure was reported by Khasanah et al., but two are reported in this study may be due to the different confinement in ultrathin and thin films); the lower angle one arises from the less ordered intermediate structure (*inter, L*), whereas the higher angle one is due to the highly-ordered intermediate structure (*inter, H*). One may wonder about the controversy between the GI-WAXD and ATR-FTIR observations in this study: the IR spectra indicate the presence of only one intermediate state (1731 cm^{-1} band), whereas the GI-

WAXD results show two kinds of intermediate states. The reason for this controversy may be ascribed to the different principles of IR and WAXD, which are sensitive to changes of the dipole moment and the crystal lattice, respectively. Therefore, IR spectra usually reflect different conformations of polymers, whereas WAXD is usually used to investigate ordered structures having three-dimensional periodicity, such as crystals. Therefore, one possibility is that the two intermediate structures possess similar conformations. To find the true reason, it is crucial to conduct simultaneous GI-WAXD and ATR-FTIR measurements.

Time-resolved fractions of less ordered intermediate structure ($X_{inter,\ L}(t)$), highly-ordered intermediate structure ($X_{inter,\ H}(t)$), and crystalline structure ($X_{Crys}(t)$) during SEC between 75–100 s are shown in Figure 1-11. Even though the diffraction peaks of crystalline PHB appeared after 55 s, their intensity was very low, and the noise level was high. Therefore, it was impossible to successfully carry out curve-fitting of the profiles in the 55–70 s domain. Thus, the plot starts at 75 s in Figure 1-11. The fraction of each part was calculated based on the curve-fitting result using the following equation (using $X_{inter,\ L}(t)$ as an example):

$$X_{inter,\ L}(t)\ \% = \frac{A_{inter,\ L}}{A_{inter,\ L} + A_{inter,\ H} + A_{Crys}} \times 100 \qquad (1\text{-}1)$$

where $A_{inter,\ L}$ is the diffraction peak area of *inter, L*. From Figure 1-11 (at 75 s), X_{Crys} is calculated to be around 30%, whereas $X_{inter,\ L}$ and $X_{inter,\ H}$ are around 25 and 45%, respectively. With the progress of SEC, X_{Crys} increases to about 41% and $X_{inter,\ L}$ and $X_{inter,\ H}$ decrease to about 8% and 21%, respectively, at 80 s. Starting from 85 s, X_{Crys}, $X_{inter,\ L}$, and $X_{inter,\ H}$ are stable around 70, 8, and 22%, respectively. It should be noted that GI-WAXD could not detect scattering due to the amorphous region in this study, so the transition from amorphous to intermediate and then to crystalline structure cannot be reflected. These changes very clearly indicate the existence of an intermediate structure in the PHB/chloroform solution system, which can transform into crystalline structure during SEC. Moreover, based on the behavior observed from 75 to 85 s, it is reasonable to speculate that the pure intermediate structure is formed before the onset of crystalline structure formation. This also agrees with the ATR- FTIR results of the present study.

Conclusion

Solvent evaporation crystallization of a PHB/chloroform solution was investigated at room temperature by time-resolved ATR-FTIR and GI-WAXD. A glass tube was used to hold the solution, slowing down the evaporation rate of chloroform during ATR-FTIR measurements. The SEC in the ATR-FTIR measurement can be divided into the following 5 steps: <1> only the PHB concentration increases with time, and the solution is still homogeneous; <2> the concentration is beyond the saturation point of the PHB/chloroform solution. Phase separation starts to occur and PHB begins to separate out from the chloroform solvent. The separation of PHB produces a mixture of intermediate and amorphous structures; <3> PHB continues to separate out from solution as chloroform evaporates, but the rate of phase separation is lower than between step <2>; <4> *intra* starts to appear in the crystal structure of PHB, becoming stronger as crystallization progresses; <5> the IR absorbance and wavenumber of the *intra* C=O stretching band show almost no change, indicating that the SEC is complete.

Time-resolved GI-WAXD measurements were performed by casting the PHB/chloroform solution on a Si substrate. The diffraction arcs of PHB during SEC were very broad. The curve fitting procedure revealed that the diffraction peak of the (020) lattice plane contained three overlapping peaks, attributable to the less ordered intermediate, highly-ordered intermediate, and crystalline structures. During SEC, the intermediate structure was formed first, subsequently transforming into the crystalline structure.

References

1. Mandelkern, L.; *Crystallization of polymers*; McGraw-Hill: New York, 1964.
2. Wunderlich, B.; *Macromolecular Physics*; Academic Press: New York, 1980; Vol. 3.
3. Sharples, A.; *Introduction to Polymer Crystallization*; Edward Arnold Ltd.: London, 1966.
4. Armitstead, K.; Goldbeck-Wood, G. *Polymer crystallization theories*. Adv. Polym. Sci. 1992, 100, pp 219−312.
5. Reiter, G.; Strobl, G. R.; *Progress in Understanding Polymer Crystallization*; Springer-Verlag: Berlin, 2007.
6. Zhang, J.; Duan, Y.; Sato, H.; Tsuji, H.; Noda, I.; Yan, S.; Ozaki, Y. Crystal Modifications and Thermal Behavior of Poly(l-lactic acid) Revealed by Infrared Spectroscopy. *Macromolecules* **2005**, 38, 8012–8021.
7. Zhang, J.; Tsuji, H.; Noda, I.; Ozaki, Y. Weak Intermolecular Interactions during the Melt Crystallization of Poly(l-lactide) Investigated by Two-Dimensional Infrared Correlation Spectroscopy. *J. Phys. Chem. B* **2004**, 108, 11514–11520.
8. Hoogsteen, W.; Postema, A. R.; Pennings, A. J.; Ten Brinke, G.; Zugenmaier, P. Crystal Structure, Conformation and Morphology of Solution-Spun Poly($_L$-lactide) Fibers. *Macromolecules* **1990**, 23, 634–642.
9. Eling, B.; Gogolewski, S.; Pennings, A. J. Biodegradable materials of poly ($_L$-lactic acid): 1. Melt-spun and solution-spun fibers. *Polymer* **1982**, 23, 1587–1593.
10. Puiggali, J.; Ikada, Y.; Tsuji, H.; Cartier, L.; Okihara, T.; Lotz, B. The frustrated structure of poly ($_L$-lactide). *Polymer* **2000**, 41, 8921–8930.
11. Cartier, L.; Okihara, T.; Ikada, Y.; Tsuji, H.; Puiggali, J.; Lotz, B. Epitaxial crystallization and crystalline polymorphism of polylactides. *Polymer* **2000**, 41, 8909–8919.
12. Porter, R. S.; Johnson, J. F. The entanglement concept in polymer systems. *Chem. Rev.* **1966**, 66, 1–27.
13. Lotz, B. What can polymer crystal structure tell about polymer crystallization processes? *Eur. Phys. J. E* **2000**, 3, 185–194.
14. Cheng, S.; Li, C. Y.; Zhu, L. Commentary on polymer crystallization: Selection rules in different length scales of a nucleation process. *Eur. Phys. J. E* **2000**, 3, 195–197.

15. Lee, M.; Park, J. K.; Lee, H.; Lane, O.; Moore, R. B.; McGrath, J. E.; Baird, D. G. Effects of block length and solution-casting conditions on the final morphology and properties of disulfonated poly(arylene ether sulfone) multiblock copolymer films for proton exchange membranes. *Polymer* **2009**, 50, 6129–6138.
16. Heinzer, M. J.; Han, S.; Pople, J. A.; Baird, D. G.; Martin, S. M. In Situ Measurement of Block Copolymer Ordering Kinetics during the Drying of Solution-Cast Films Using Small-Angle X-ray Scattering. *Macromolecules* **2012**, 45, 3471–3479.
17. Gong, Y.; Huang, H.; Hu, Z.; Chen, Y.; Chen, D.; Wang, Z.; He, T. Inverted to Normal Phase Transition in Solution-Cast Polystyrene-Poly(methyl methacrylate) Block Copolymer Thin Films. *Macromolecules* **2006**, 39, 3369–3376.
18. Yuan, Y.; Shu, J.; Liu, P.; Zhang, Y.; Duan, Y.; Zhang, J. Study on π–π Interaction in H- and J-Aggregates of Poly(3-hexylthiophene) Nanowires by Multiple Techniques. *J. Phys. Chem. B* **2015**, 119, 8446–8456.
19. Zhao, W.; Liu, F.; Wei, X.; Chen, D.; Grason, G. M.; Russell, T. P. Formation of H* Phase in Chiral Block Copolymers: Morphology Evolution As Revealed by Time-Resolved X-ray Scattering. *Macromolecules* **2013**, 46, 474–483.
20. Toolan, D. T. W.; Isakova, A.; Hodgkinson, R.; Reeves-McLaren, N.; Hammond, O. S.; Edler, K. J.; Briscoe, W. H.; Arnold, T.; Gough, T.; Topham, P. D.; Howse, J. R. Insights into the Influence of Solvent Polarity on the Crystallization of Poly(ethylene oxide) Spin-Coated Thin Films via in Situ Grazing Incidence Wide-Angle X-ray Scattering. *Macromolecules* **2016**, 49, 4579–4586.
21. Huang, H.; Hu, Z.; Chen, Y.; Zhang, F.; Gong, Y.; He, T.; Wu, C. Effects of Casting Solvents on the Formation of Inverted Phase in Block Copolymer Thin Films. *Macromolecules* **2004**, 37, 6523–6530.
22. Rubinstein, M.; Colby, R. *Polymers physics*; Oxford: UK, 2003.
23. Heinzer, M. J.; Han, S.; Pople, J. A.; Baird, D. G.; Martin, S. M. In Situ Tracking of Microstructure Spacing and Ordered Domain Compression during the Drying of Solution-Cast Block Copolymer Films Using Small-Angle X-ray Scattering. *Macromolecules* **2012**, 45, 3480–3486.
24. Ogawa, H.; Takenaka, M.; Miyazaki, T.; Fujiwara, A.; Lee, B.; Shimokita, K.; Nishibori, E.;

Takata, M. Direct Observation on Spin-Coating Process of PS-b-P2VP Thin Films. *Macromolecules* **2016**, *49*, 3471–3477.

25. Shimokita, K.; Miyazaki, T.; Ogawa, H.; Yamamoto, K. Development of a simultaneous measurement system for SAXS-WAXD and the thickness of coating films during film formation by solvent evaporation. *J. Appl. Crystallogr.* **2014**, 47, 476–481.
26. Chalmers, J. M. Spectra–Structure Correlations: Polymer Spectra. Chalmers, J. M.; Griffiths, P. R., Chalmers, J. M.; Griffiths, P. R., Eds.; *Handbook of Vibrational Spectroscopy*; John Wiley & Sons, Ltd: Chichester, 2002.
27. Krimm, S.; *Infrared Spectra of High Polymers*; Springer: Berlin, 1960, pp 51−172.
28. Bower, D. I.; Maddams, W. F.; *The vibrational spectroscopy of polymers*; Cambridge University Press: New York, 1992.
29. Zhang, J.; Duan, Y.; Shen, D.; Yan, S.; Noda, I.; Ozaki, Y. Structure Changes during the Induction Period of Cold Crystallization of Isotactic Polystyrene Investigated by Infrared and Two-Dimensional Infrared Correlation Spectroscopy. *Macromolecules* **2004**, 37, 3292–3298.
30. Yan, C.; Zhang, Y.; Hu, Y.; Ozaki, Y.; Shen, D.; Gan, Z.; Yan, S.; Takahashi, I. Melt Crystallization and Crystal Transition of Poly(butylene adipate) Revealed by Infrared Spectroscopy. *J. Phys. Chem. B* **2008**, 112, 3311–3314.
31. Tashiro, K.; Ueno, Y.; Yoshioka, A.; Kobayashi, M. Molecular Mechanism of Solvent-Induced Crystallization of Syndiotactic Polystyrene Glass. 1. Time-Resolved Measurements of Infrared/Raman Spectra and X-ray Diffraction. *Macromolecules* **2001**, 34, 310–315.
32. Barham, P. J.; Keller, A.; Otun, E. L.; Holmes, P. A. Crystallization and morphology of a bacterial thermoplastic: poly-3-hydroxybutyrate. *J. Mater. Sci.* **1984**, 19, 2781–2794.
33. Furuhashi, Y.; Imamura, Y.; Jikihara, Y.; Yamane, H. Higher order structures and mechanical properties of bacterial homo poly(3-hydroxybutyrate) fibers prepared by cold-drawing and annealing processes. *Polymer* **2004**, 45, 5703–5712.
34. Zhang, J.; Sato, H.; Noda, I.; Ozaki, Y. Conformation Rearrangement and Molecular Dynamics of Poly(3-hydroxybutyrate) during the Melt-Crystallization Process Investigated by Infrared and Two-Dimensional Infrared Correlation Spectroscopy. *Macromolecules* **2005**, 38, 4274–4281.
35. Murakami, R.; Sato, H.; Dybal, J.; Iwata, T.; Ozaki, Y. Formation and stability of β-structure

in biodegradable ultra-high-molecular-weight poly(3-hydroxybutyrate) by infrared, Raman, and quantum chemical calculation studies. *Polymer* **2007**, 48, 2672–2680.

36. Sato, H.; Ando, Y.; Dybal, J.; Iwata, T.; Noda, I.; Ozaki, Y. Crystal Structures, Thermal Behaviors, and C−H ··O═C Hydrogen Bondings of Poly(3-hydroxyvalerate) and Poly(3-hydroxybutyrate) Studied by Infrared Spectroscopy and X-ray Diffraction. *Macromolecules* **2008**, 41, 4305–4312.
37. Guo, L.; Spegazzini, N.; Sato, H.; Hashimoto, T.; Masunaga, H.; Sasaki, S.; Takata, M.; Ozaki, Y. Multistep Crystallization Process Involving Sequential Formations of Density Fluctuations, "Intermediate Structures", and Lamellar Crystallites: Poly(3-hydroxybutyrate) As Investigated by Time-Resolved Synchrotron SAXS and WAXD. *Macromolecules* **2012**, 45, 313–328.
38. Doi, Y.; Kitamura, S.; Abe, H. Microbial Synthesis and Characterization of Poly(3-hydroxybutyrate-co-3-hydroxyhexanoate). *Macromolecules* **1995**, 28, 4822–4828.
39. Chiellini, E.; Solaro, R. *Recent Advances in Biodegradable Polymers and Plastics*; Wiley-VCH: Weinheim, 2003.
40. Vert, M. Aliphatic Polyesters: Great Degradable Polymers That Cannot Do Everything. *Biomacromolecules* **2005**, 6, 538–546.
41. Bastioli, C. *Handbook of Biodegradable Polymers*; Rapra Technology Limited: Shawbury, U.K., 2005.
42. Cobntbekt, J.; Mabchessault, R. H. Physical properties of poly-β-hydroxybutyrate: IV. Conformational analysis and crystalline structure. *J. Mol. Biol.* **1972**, 71, 735–756.
43. Yokouchi, M.; Chatani, Y.; Tadokoro, H.; Teranishi, K.; Tani, H. Structural studies of polyesters: 5. Molecular and crystal structures of optically active and racemic poly (β-hydroxybutyrate). *Polymer* **1973**, 14, 267–272.
44. Wang, H.; Tashiro, K. Reinvestigation of Crystal Structure and Intermolecular Interactions of Biodegradable Poly(3-Hydroxybutyrate) α-Form and the Prediction of Its Mechanical Property. *Macromolecules* **2016**, 49, 581–594.
45. Sato, H.; Murakami, R.; Padermshoke, A.; Hirose, F.; Senda, K.; Noda, I.; Ozaki, Y. Infrared Spectroscopy Studies of CH ··O Hydrogen Bondings and Thermal Behavior of Biodegradable Poly(hydroxyalkanoate). *Macromolecules* **2004**, 37, 7203–7213.
46. Barham, P. J.; Keller, A.; Otun, E. L.; Holmes, P. A. Crystallization and morphology of a

bacterial thermoplastic: poly-3-hydroxybutyrate. *J. Mater. Sci.* **1984**, 19, 2781–2794.

47. Barham, P. J. Nucleation behaviour of poly-3-hydroxy-butyrate. *J. Mater. Sci.* **1984**, 19, 3826-3834.
48. Suttiwijitpukdee, N.; Sato, H.; Zhang, J.; Hashimoto, T. Effects of Intermolecular Hydrogen Bondings on Isothermal Crystallization Behavior of Polymer Blends of Cellulose Acetate Butyrate and Poly(3-hydroxybutyrate). *Macromolecules* **2011**, 44, 3467–3477.
49. Jacquel, N.; Lo, C. W.; Wu, H. S.; Wei, Y. H.; Wang, S. S. Solubility of polyhydroxyalkanoates by experiment and thermodynamic correlations. *AIChE J.* **2007**, 53, 2704–2714.
50. Khasanah; Reddy, K. R.; Ogawa, S.; Sato, H.; Takahashi, I.; Ozaki, Y. Evolution of Intermediate and Highly Ordered Crystalline States under Spatial Confinement in Poly(3-hydroxybutyrate) Ultrathin Films. *Macromolecules* **2016**, 49, 4202-4210.
51. Strobl, G. R. *The physics of polymers*; Springer: Berlin, 1997.

Table 1-1: Assignment for Major IR Absorbance Bands of PHB and Chloroform.

IR frequencies (cm^{-1})	assignments	IR frequencies (cm^{-1})	assignments
3020	CH_3 asymmetric stretching mode in chloroform	1738	C=O stretching mode in PHB (A)
3009	CH_3 asymmetric stretching mode in PHB (C)	1731	C=O stretching mode in PHB (I)
2998	CH_3 asymmetric stretching mode in PHB	1722	C=O stretching mode in PHB (C)
2974	CH_3 asymmetric stretching mode in PHB (C)	1686	C=O stretching mode in PHB (C)
2934	CH_2 asymmetric stretching mode in PHB (C)	742	C−Cl stretching mode in chloroform
2874	CH symmetric stretching mode in PHB (C)		
1748	C=O stretching mode in PHB (A)		

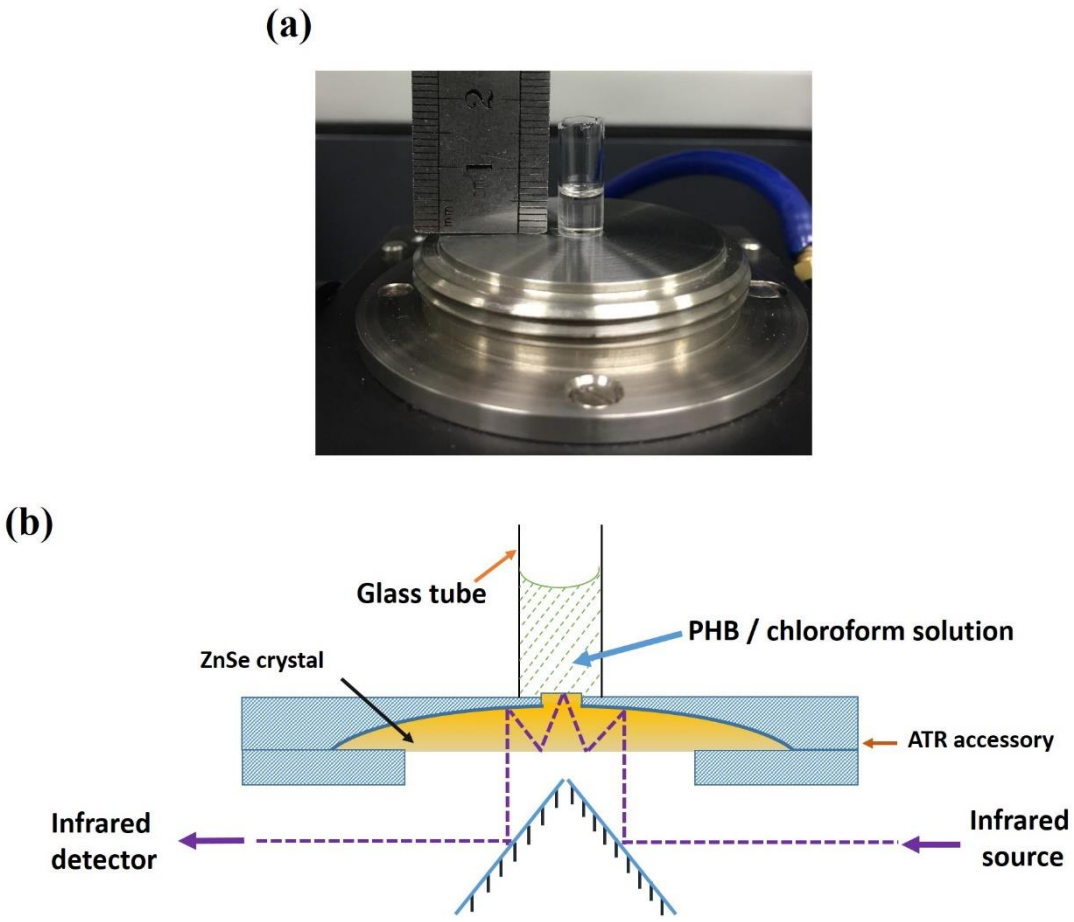

Figure 1-1: The picture (a) and the schema (b) of the ATR accessory during measurement.

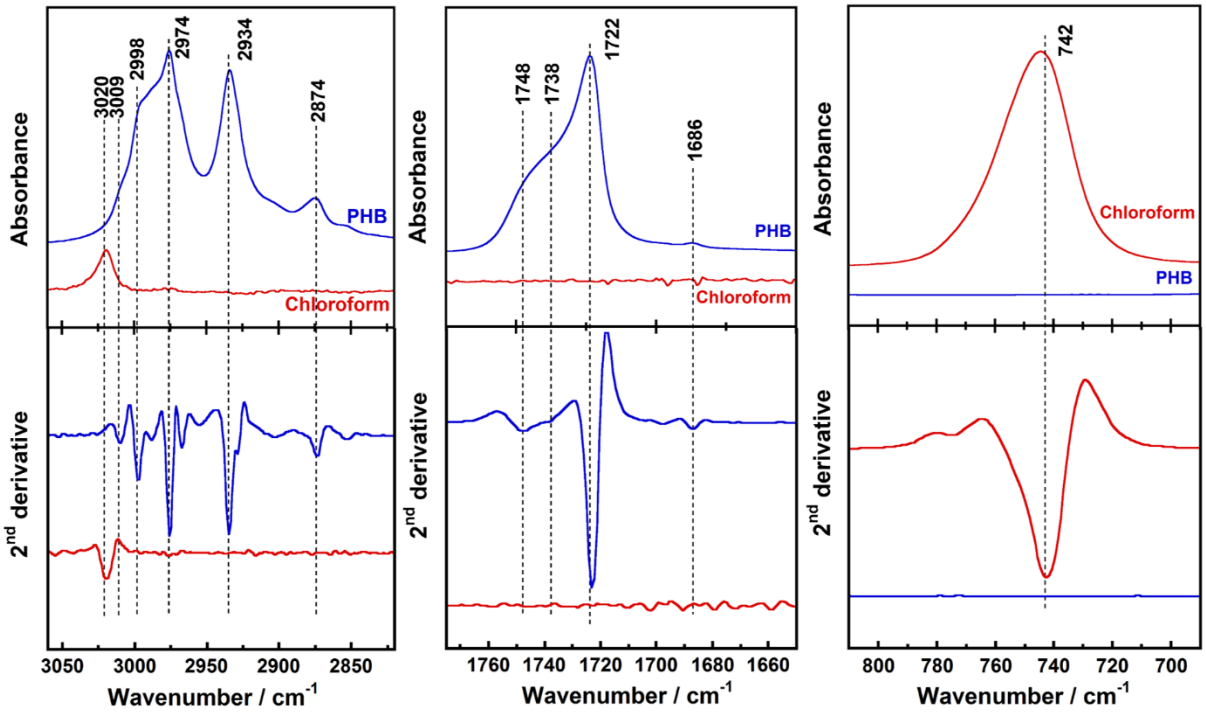

Figure 1-2: ATR-FTIR spectra (top panels) and their second derivatives spectra (bottom panels) in the C−H stretching region (a), C=O stretching region (b) and C−Cl stretching region (c) of pure PHB and chloroform.

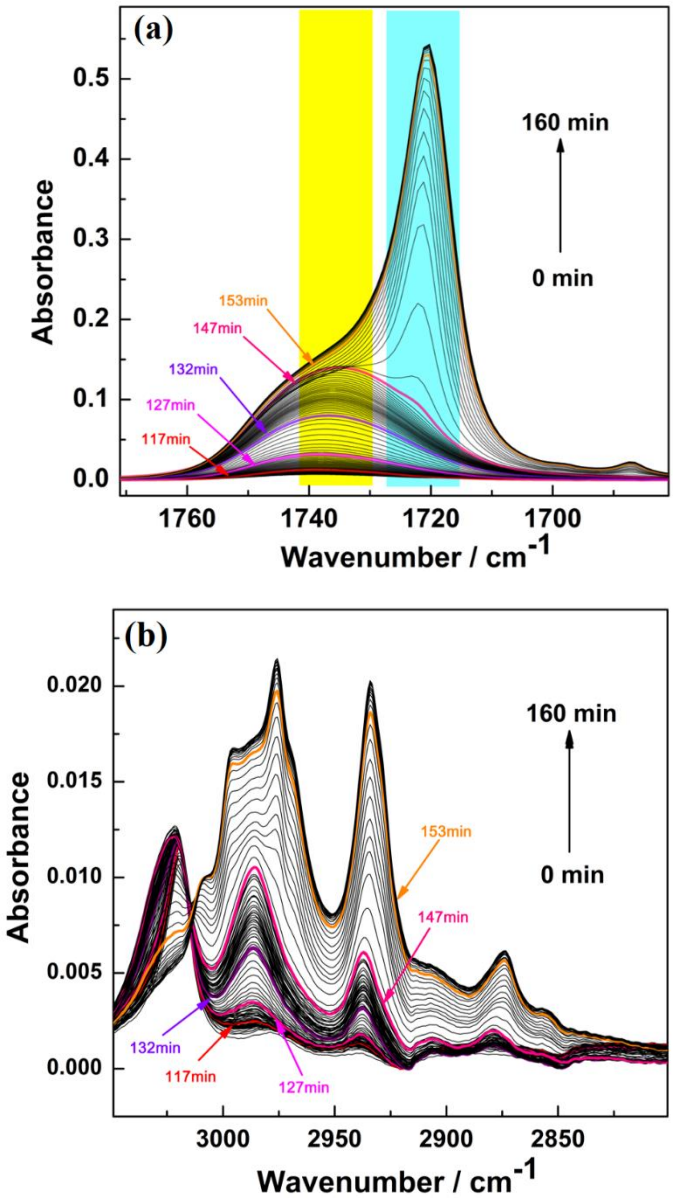

Figure 1-3: ATR-FTIR spectra in the C=O stretching region (a) and C−H stretching region (b) from 0 to 160 min during SEC.

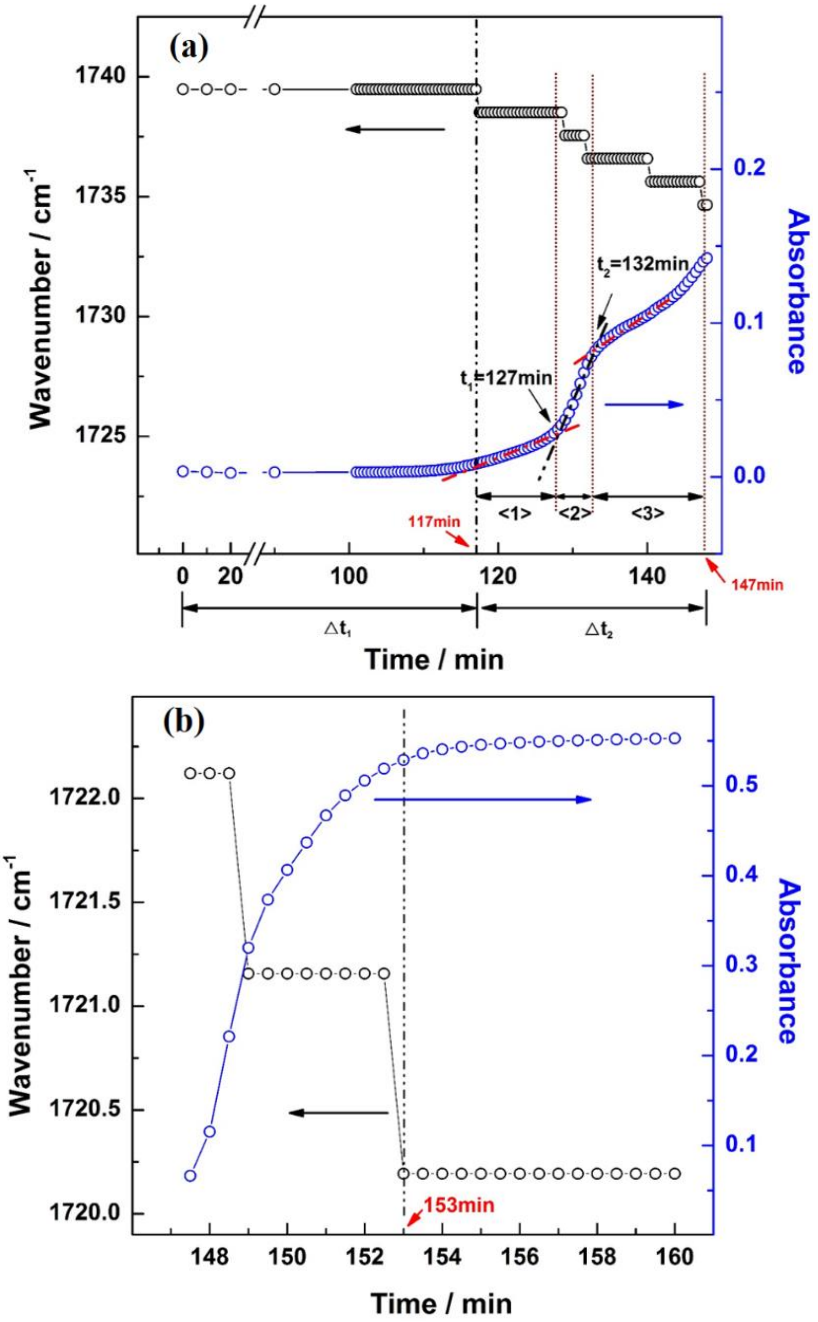

Figure 1-4: ATR-FTIR absorbance and wavenumber change of amorphous (a) and crystal (b) C=O stretching bands of PHB/chloroform solution with time during SEC.

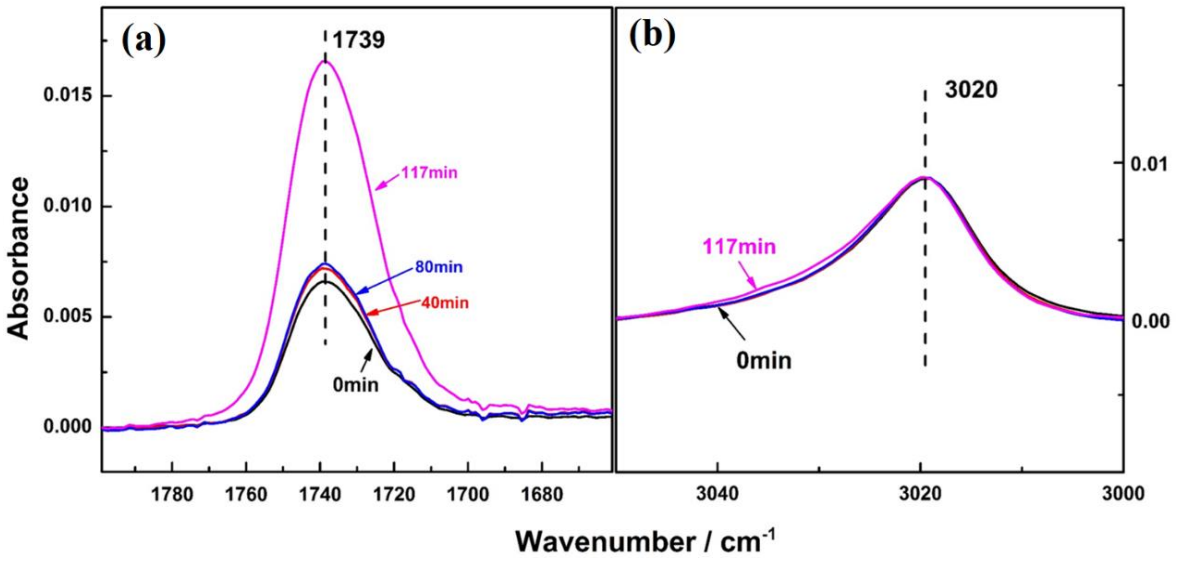

Figure 1-5: ATR-FTIR spectra of the C=O (amorphous) (a) and C-H stretching band in chloroform (b) during Δt_1.

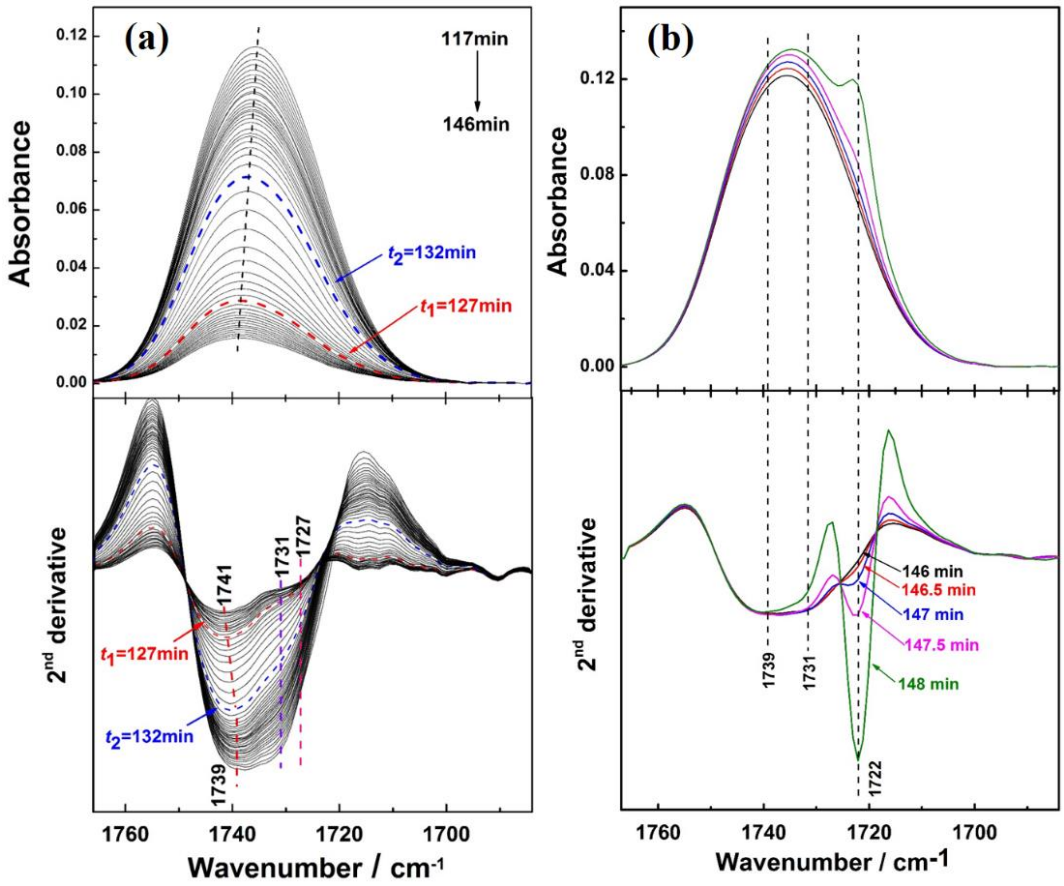

Figure 1-6: ATR-FTIR spectra (top panels) and their second derivatives spectra (bottom panels) in the C=O stretching band region of PHB during 117-146 min (a) and 146-148 min (b).

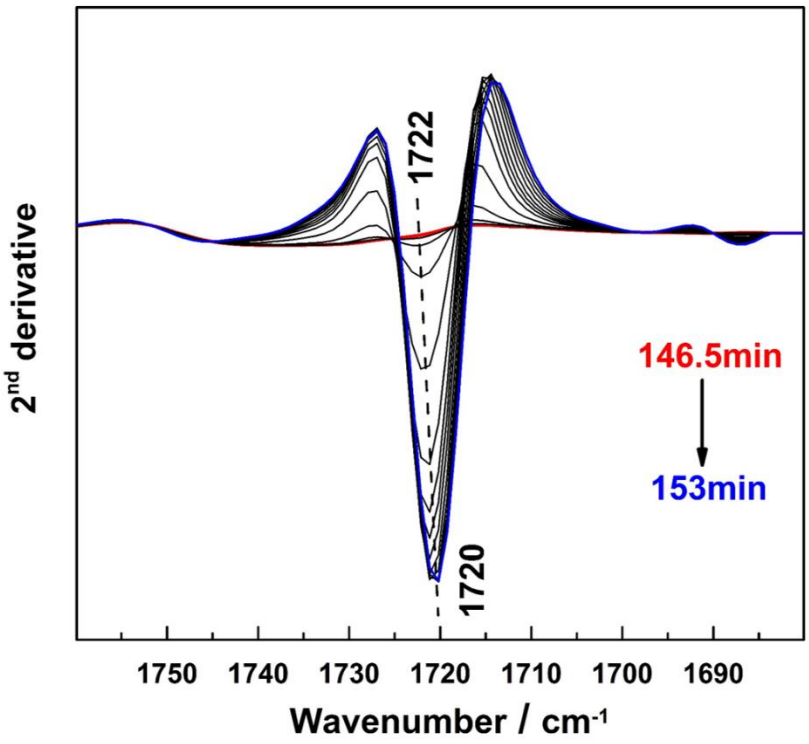

Figure 1-7: Second derivative spectra in C=O stretching band region of PHB during 146.5-153 min.

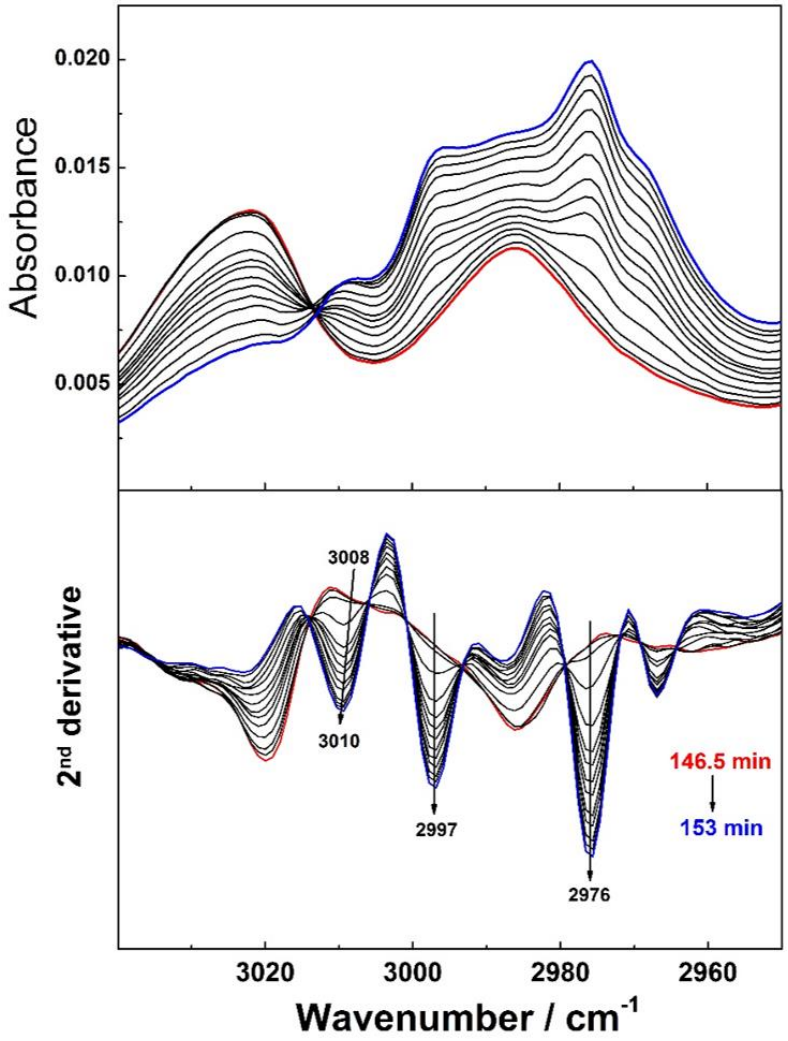

Figure 1-8: ATR-FTIR spectra (top panels) and their second derivatives spectra (bottom panels) in the C−H stretching region of PHB/chloroform solution during SEC from 146.5 to 153 min.

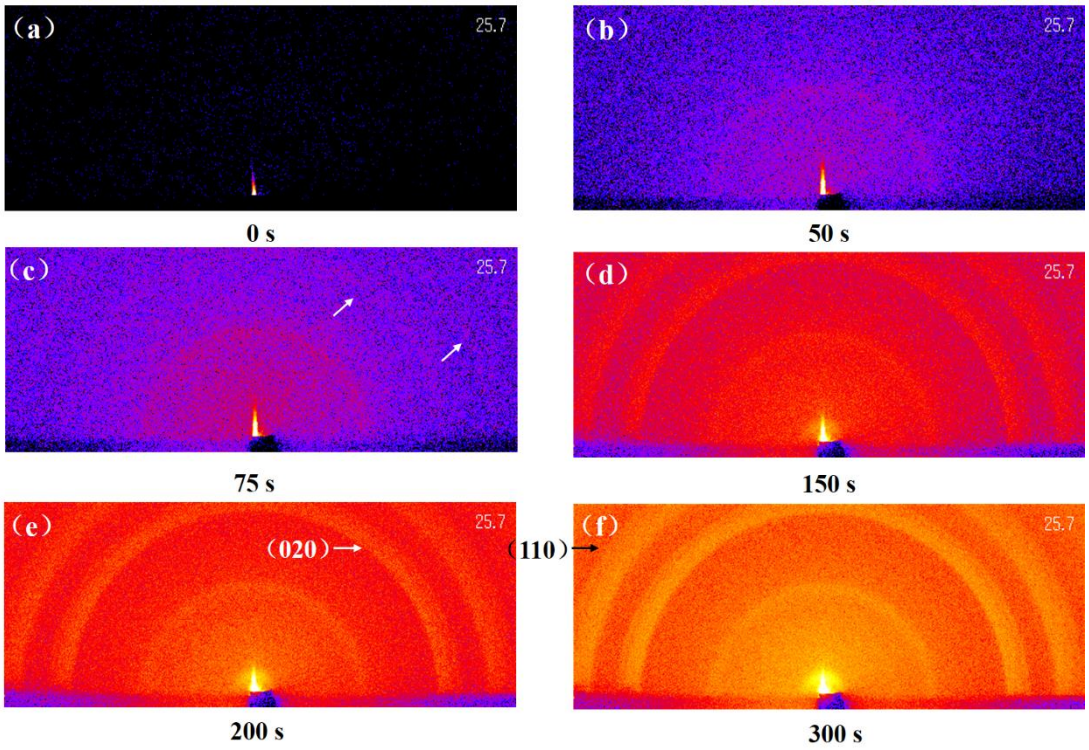

Figure 1-9: Time-resolved two-dimensional GI-WAXD patterns of PHB/chloroform solution during SEC at 0s (a), 50 s (b), 75 s (c), 150 s (d), 200 s (e) and 300 s (f).

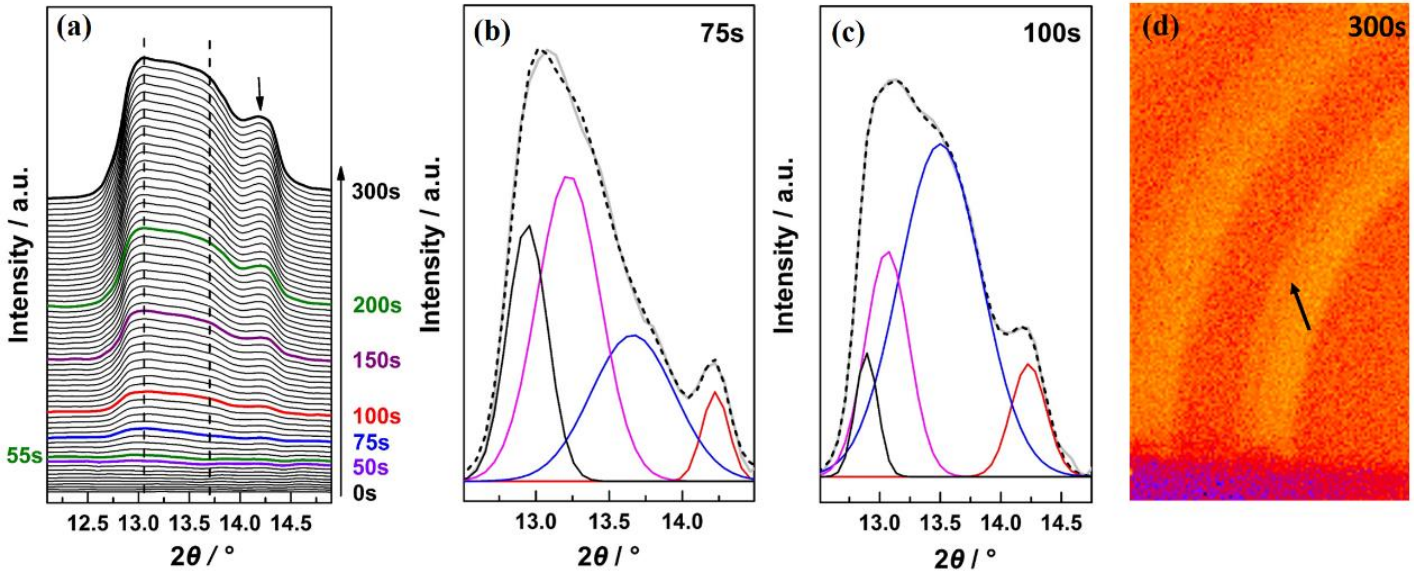

Figure 1-10: Time-resolved GI-WAXD profiles of PHB/chloroform solution during SEC from 0 to 300 s (a). Enlarged GI-WAXD pattern of PHB/chloroform solution during SEC at 300 s (b). Decomposition of the diffraction profiles at 75 s (c) and 100 s (d) (grey solid line) into less ordered intermediate structure (black solid line); highly-ordered intermediate structure (purple solid line); crystal (blue solid line); ghost diffraction (red solid line), the reconstructed diffraction profile (dotted line) was obtained by summing the diffraction of the elemental peaks.

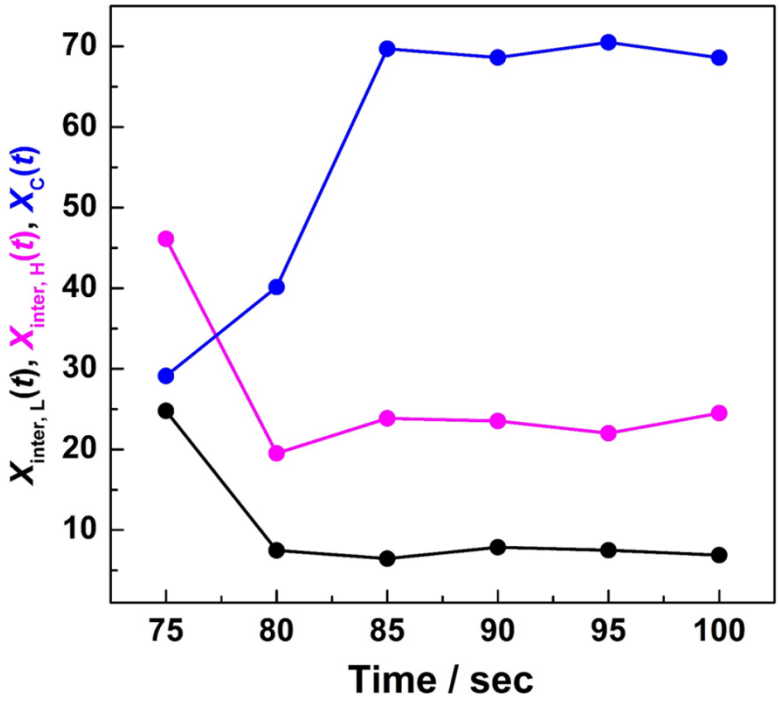

Figure 1-11: Percentage fraction of the less ordered intermediate structure (black solid symbols line), highly-ordered intermediate structure (purple solid symbols line) and crystal (blue solid symbols line) as a function of time.

Chapter 2

Reinvestigation of the β-to-α Crystal Phase Transition of Poly(butylene adipate) by the Time-Resolved X-ray Scattering and FTIR Spectral Measurements in the Temperature-Jump Process

ABSTRACT

Poly(butylene adipate) (PBA) exhibits the two types of crystal modification, the α and β forms, depending on the sample preparation conditions. They show the different degree of biodegradability. A majority of papers published so far reported that the phase transition from the β-form to the α-form occurs as the direct solid-to-solid process when the sample is heated up to the high temperature of around 55 ℃. The author have reinvestigated this β-to-α phase transition by performing the temperature-jump time-resolved measurement of the FTIR, WAXD, and SAXS measurements. This transition has been found to be not a solid-to-solid phase transition but the combined phenomena of the melting of the β-phase followed by the recrystallization to the high-temperature α-phase.

Introduction

Recently, environmental issues become severe all around the world. Especially, so-called "plastic pollution", which is caused by such synthetic polymers as polyethylene (PE), polystyrene (PS), poly(vinyl chloride) (PVC), etc., has given serious problems since they cannot be degraded naturally. The usage of a biodegradable polymer may be a good idea to reduce the above issues. After the concept of synthetic biodegradable polymers was first introduced in 1980s,[1] they have attracted more attention. The most important property for biodegradable polymers is their biodegradability, the degree of which is dependent on not only the chemical structure but also the crystal modification of the polymer.[2-4] Among the family of biodegradable polymers, poly(butylene adipate) (PBA, $-[-O(CH_2)_4OOC(CH_2)_4CO-]_n-$) and its copolymers have received substantial interest in the past two decades or so.[5-11]

PBA has been reported to crystallize into two kinds of crystal forms designated as α-form and β-form.[12-17] Gan et al.[18] demonstrated that a film of the α-crystal form has a faster degradation rate than that of the β-crystal form. The mixture of the α and β crystal forms showed the lowest degradation rate. In this way, the difference of the crystal structure (and the related morphology) between the α and β forms is very important for the control of the biodegradability. The crystal structure of PBA was reported by several research groups.[12-17,19] The α-form is characterized by its chain conformation of the planar zigzag type, and these chains are packed in the monoclinic unit cell with the dimensions of a = 6.73 Å, b = 7.94 Å, c (fiber period) = 14.20 Å and β= 45.5°, while the β-form of the planar zigzag chain conformation takes the orthorhombic unit cell with the dimensions of a = 5.06 Å, b = 7.35 Å and c (fiber period) = 14.67 Å.

The isothermal crystallization behavior of PBA was first studied by Gan et al.[20] They found that the pure β-form is formed below 29 ℃, while the pure α-form is formed above 31 ℃, and these two crystals are formed simultaneously at 30±1 ℃. It has been found also that the β-form crystal transforms spontaneously into the a-form by storing at room temperature.[21] The β-form was considered to be the kinetically preferable crystal, while the a-form is the thermodynamically more stable.[19]

The thermal treatment of the crystal modification of PBA was studied by focusing on the β-to-α phase transition behavior.[19,20,22-26] From the differential scanning calorimeter (DSC) and wide-

angle X-ray diffraction (WAXD) results, Gan et al.[19] suggested that this process is a solid-to-solid phase transition since it can occur even when the annealing temperature is lower than the T_m of the original β-form crystal. On the contrary, on the basis of the temperature-dependent Fourier-transform infrared (FTIR) spectral measurement, Li et al.[26] found out that the β-form crystals still remain after annealing at 45 ℃ for a long time. They suggested that the heat-treated β-form has the higher stability and that it may be from the recrystallization of the original β-form crystals. From the significant drop of the crystallinity during the phase transition, they suggested also that the β-to-α phase transition is a melt-recrystallization process.

In general, the phase transition of the crystalline polymers usually occurs over a relatively wide temperature region.[27] By the conventional temperature-dependent X-ray or vibrational spectroscopic measurements, it is sometimes difficult to judge whether the phase transition occurs by the direct solid-to-solid mechanism or by the process of the melt of the low-temperature phase followed by the recrystallization to the high-temperature phase. The crystallite size in the semicrystalline polymer distributes over a wide range and so the T_m itself distributes correspondingly. The smaller crystallites are melted at a lower temperature, and they are crystallized again on the surface of the larger crystallites. If the thermodynamically more-stable crystal phase can exist there, the crystallization of the once-melted region may occur with the appearance of the thermodynamically stable phase, which is named often the melt-recrystallization.

Because of such a complicated structural situation of crystalline polymer, it is quite difficult to distinguish the above-mentioned two transition processes (the solid-to-solid transition or the melt-recrystallization) on the basis of the conventional and easier temperature-dependent measurement of the X-ray diffraction and/or vibrational spectral data. Even the DSC thermogram might become ambiguous to choose the correct transition mechanism definitely because the endothermic and exothermic peaks are broad and overlapped together.

The key point of tracing the concretely occurring structural change during the phase transition is to clarify the sequentially occurring phenomena at the different timings. Ratri and Tashiro[27] performed the temperature-jump experiment for this purpose. The principle is as follows. The temperature is changed quite quickly from a low temperature to a preset high temperature, and then it is kept at the latter value constantly. During this process the IR spectra or X-ray diffraction data are measured at as short and constant time interval as possible. If the time resolution is high

enough to separate the various sequentially occurring phenomena, we can know the structural changes of the individual stages. They performed this type of experiment for the high-temperature phase transitions of poly(vinylidene fluoride) [PVDF] form I and *trans*-1,4-polyisoprene.[27] For example, in the case of PVDF form I, the form I crystals disappeared at first and the amorphous phase started to appear after the temperature jump to near the T_m, and then the form III (or V) crystal appeared at a later timing along with the decrease of the amorphous phase. This experiment revealed clearly the form I transforms to the melt state at first then followed by the recrystallization into the form III at a temperature immediately below the T_m of form III. This time-dependent temperature-jump experiment gave an answer for the long-time unsolved problem whether the polar-to-nonpolar phase transition (or ferroelectric phase transition) of the PVDF crystal form I can be observed in the temperature region below the T_m or not.[28]

In the present study, therefore, on the basis of the temperature-jump experiments of the time-resolved FTIR and X-ray scattering measurements, the author have been challenged to reveal the above-mentioned problem about the phase transition behavior of PBA. As will be described below, the author have found that the β-to-α phase transition is not a simple solid-to-solid process, but the β-form is melted once to the amorphous phase and then recrystallization occurs into the α-form. The thus-obtained α-phase was found to be different from the α-form obtained by slow cooling from the melt to the room temperature in such a point of crystalline regularity and crystallite size. In other words, the α-phase obtained from the β-phase at a high temperature may be named the "high-temperature α-phase".

Experimental Section

Materials

PBA with MW = 12000 g/mol was purchased from Polysciences, Inc., and was used without further purification. A PBA solution with a concentration of 1 wt % was prepared by dissolving PBA chips in hot chloroform to make a homogeneous solution. For FTIR and simultaneous WAXD/DSC measurements, the samples were prepared by casting from the solutions on a KBr single crystal plate and an Al substrate at room temperature, respectively. After fully dried, the sample was directly used for FTIR or simultaneous WAXD/DSC measurements. This is to ensure that no phase transition occurs before the measurements, since as mentioned in the Introduction, the phase transition of PBA can occur even by storing it at room temperature. The author also compared the FTIR spectra for the samples with and without keeping in a vacuum oven; both of them did not show any chloroform absorbance. The sample thus prepared was designated hereafter as "the as-cast" film.

For the time-dependent simultaneous WAXD/small-angle X-ray scattering (SAXS) measurements, the sample was prepared by casting a PBA/chloroform solution on a microscope glass slide at room temperature first, and then the film was peeled off after it was completely dried. The film was cut to several pieces and set into a sample holder. A polyimide film was used to seal on the two sides of the sample holder.

For the WAXD/SAXS experiments at room temperature, the original β-form crystal sample was used the as-cast film directly; the original α-form crystal sample was prepared by melting PBA chips on a hot stage at 80 ℃ for 5 min to erase heat history first[22] and then quenched into a water bath at 35 ℃ to induce the isothermal crystallization.

FTIR Measurements

Temperature-dependent FTIR spectra were measured using a Thermo Nicolet 6700 FTIR spectrometer equipped with a liquid-nitrogen-cooled mercury cadmium telluride (MCT) detector. The as-cast film was set into a temperature controller CHINO (model SU) and heated from room temperature to 70 ℃ at 1 ℃/min. During heating, FTIR spectra were measured at every one degree at a 2 cm^{-1} spectral resolution, and a total of 64 scans were accumulated for each IR spectral

measurement.

For time-dependent FTIR measurements, a Varian FTS 7000 rapid-scanning FTIR spectrometer equipped with a liquid-nitrogen-cooled MCT detector was used. The as-cast film was set into a homemade optical cell for the temperature-jump measurement.[27,29] The temperature was changed quickly from room temperature to 55 ℃ at the heating rate 180 ℃/min and then kept constantly at 55 ℃ for a long time, during which the FTIR spectra were measured at every 2 s interval with resolution of 2 cm^{-1}.

The decomposition of the overlapped FTIR spectral bands was put forward using a GRAMS software (Thermo Fisher Scientific, Inc.).

Simultaneous WAXD/DSC Measurements

A Rigaku (Tokyo, Japan) X-ray diffractometer RINT-TTR III was used for the simultaneous measurement of WAXD and DSC in the heating–cooling–reheating processes from the ambient temperature. The sample temperature was changed linearly by controlling the heater and liquid nitrogen gas. The incident X-ray beam used was Cu Kα radiation (λ = 1.5418 Å) from the X-ray generator (50 kV and 300 mA). The X-ray diffraction patterns were measured in the 2θ (diffraction/scattering angle) range of 17 °–26 °, and scan speed was 15 °/min. The thermal program employed is depicted in Figure A1-1 of the Appendix 1. The diffraction profiles were obtained at every 1 ℃.

Time-Resolved Simultaneous WAXD/SAXS Measurements.

Time-resolved simultaneous WAXD/SAXS measurements were performed using a Rigaku Nanoviewer X-ray diffractometer. A two-dimensional (2D) detector (Pilatus 300K, Dectris, Switzerland) was used to detect the WAXD patterns, and the SAXS patterns were recorded using a two-dimensional (2D) detector (Pilatus 100K, Dectris, Switzerland) at 684.1 mm distance from the sample. The system consisted of a rotating anode X-ray generator (Cu Kα, 40 kV, 20 mA) and a specially designed confocal X-ray mirror with three slit optic collimators.

The measurements were performed with the temperature-jump cell used for the time-dependent FTIR measurements under the same conditions. The WAXD/SAXS patterns were recorded at every 3 min.

Results and Discussion

Temperature-Dependent IR Spectral Measurement

Temperature-dependent FTIR spectra of the as-cast PBA film in the 1000–700 cm^{-1} region are shown in Figure 2-1. The characteristic bands of the α and β forms as well as the amorphous phase are listed in Table 2-1. The IR spectrum at 30 ℃ is that of the pure β-form crystal. The typical β-form bands are detected at 930, 910, and 735 cm^{-1}. When the temperature increased to around 50 ℃, the β-form gradually transformed into the α-form as known from the decrease of the intensity of the 930 cm^{-1} β-form band and the shift of the bands at 910 and 735 cm^{-1} to 909 and 734 cm^{-1}, which are intrinsic to the α-form bands. By heating to a higher temperature, the α-form bands disappeared, and the IR spectra changed to those of the melt. The spectral data tell us that the phase transition is observed to take place at around 55 ℃ during the heating process, consistent with the previous studies.[23,24]

The clearer results were obtained also from the simultaneous WAXD/DSC measurements during the heating process, as shown in Figure 2-2. With temperature increase, the diffraction peaks β(110) and β(020) at 2θ = 21.4 ° and 24.5 °, respectively, shifted toward to the lower angle due to the thermal expansion of the unit cell, and then disappeared totally at around 55 ℃, where the diffraction peaks of the α-form started to appear at 2θ = 21.7 °(α(110)) and 22.3 °(α(110)), and coexisted with the β-form peaks and then stayed alone at higher temperature. These α-form peaks disappeared above 60 ℃ due to the melting.

In this way, both of the temperature-dependent IR spectra and WAXD profiles collected in the heating process indicated that the β-to-α phase transition took place below the T_m of the α-phase. As shown in Figure 2-2, the DSC thermogram revealed the existence of the two endothermic peaks. It is difficult to interpret this DSC data on the basis of the simple β-to-α phase transition scheme. Such a transition scheme as the melt of the original β-phase followed by the recrystallization into the α-phase may be possible. If our interpretation is reasonable, we should detect the evolution of the amorphous signals in the heating process. However, as mentioned in the Introduction, this prediction is difficult to check by the normal continuous heating experiments carried out in Figures 2-1 and 2-2.

Temperature-Jump Measurements

Therefore, we need to perform the so-called temperature-jump measurement for this purpose. Figure 2-3 shows the IR spectra of PBA during the temperature-jump experiment. The temperature was jumped from 26.5 to 55 ℃ at a heating rate of 180 ℃/min and kept at 55 ℃ constantly. The IR bands of the β-form at 930, 910, and 735 cm^{-1} almost disappeared in the heating process as seen in Figures 2-3(a) and (c). However, the important point is that the amorphous bands at 745 and 760 cm^{-1} increased in intensity in parallel to the disappearance of the β-form bands, and no IR bands of the α-form appeared even after the temperature reached at 55 ℃. The α-form bands at 909 and 734 cm^{-1} were found to appear quite slowly after long time of the temperature jump, as shown in Figures 2-3(b) and (d). To make this process more clearly, the integrated intensity was estimated for the IR bands of the β, α, and amorphous phases and plotted against time as shown in Figure 2-4 The integrated absorbance of amorphous (745 and 760 cm^{-1}), β-form (735 cm^{-1}) and α-form (734 cm^{-1}) bands was obtained by decomposition of the IR spectra in the region of 770–720 cm^{-1}. Immediately after the temperature was jumped to 55 ℃, the β-form bands at 930 and 735 cm^{-1} disappeared at first and the integrated intensity for the amorphous phase bands increased conspicuously. The α-form bands appeared about 40 min later and the amorphous bands decreased in intensity again.

The similar temperature-jump experiment was performed for the simultaneous time-resolved WAXD/SAXS measurement. Figures 2-5(a) and (b) show the time dependence of the WAXD profiles measured in the temperature-jump procedure and WAXD profiles of the original α- and β-form measured at room temperature, respectively. Although the profile itself is quite noisy because the thin film was used for the measurement so that the temperature changed quickly and homogeneously over through the sample cross section. In Figure 2-5(a), the starting sample was of the β-phase. After the temperature jump, the β-form diffraction peaks disappeared immediately, and the broad amorphous halo peak was detected instead. The α-phase peaks started to appear at around 40 min after the jump.

From both of the experimental data of IR and X-ray diffraction, we can conclude that the apparently solid-to-solid transition from the β-to-α phase occurs actually through such a mechanism as the melt of the β-phase followed by the recrystallization to the α-phase.

The higher-order structural change during the phase transition process was deduced from the SAXS data analysis, which was obtained at the same time as the WAXD data during the temperature-jump experiment. As can be seen in Figure 2-5(c), the original β-form crystal showed the broad peak at around q = 0.049 Å^{-1}, where q is the scattering vector and defined as $q = (4\pi/\lambda)\sin\theta$. It should be noticed that this broad peak disappeared totally immediately after the temperature jump, and the new peak appeared at around q = 0.033 Å^{-1}. This new peak increased the intensity with the passage of time. By referring to the above-mentioned WAXD profiles in Figure 2-5(a), this new peak can be assigned to that of the α-form crystal. However, when compared with the SAXS data of the normally prepared pure α and β forms measured at room temperature (Figure 2-5(d)), the SAXS peak position of the α-phase obtained at 55 ℃ by the temperature jump from the β-phase is different from that of the original α-phase prepared by melt-quenching method (q = 0. 055 Å^{-1}).

The illustration of the stacked lamellar structure is shown in Figure 2-6. The structure parameters were estimated by calculating the correlation function $K(z)$ from the SAXS data, where $K(z)$ is defined as[30]

$$K(z) = \langle [c_e(z') - \langle c_e \rangle][\langle c_e(z+z') - \langle c_e \rangle \rangle] \rangle \propto 2\int_0^\infty I(q)\, q^2 cos(qz) dq \qquad (2\text{-}1)$$

The $c_e(z)$ and $\langle c_e \rangle$ are the electron density c_e at the position z along the lamellar stacking direction and the averaged electron density, respectively. The $\langle\ \rangle$ is the statistic ensemble average. The illustration of the stacked lamellar structure and the electron density distribution along the stack normal are shown in Figures 2-6(a) and (b), respectively. The evolution of the long period (LP) and the averaged lamellar thickness $\langle d \rangle$ of the stacked lamellar structure are obtained from the various particular positions in the correlation function curves as shown in Figure 2-6(c). Since the crystallinity of the sample used here was less than 50%, the correlation function gave the thickness of the crystalline lamellae, not that of the amorphous region. The change of the scattering invariant Q during the β-to-α phase transition was calculated as follows:

$$Q = \int_0^\infty I(q)\, q^2 dq \qquad (2\text{-}2)$$

The Q value is related to the degree of crystallinity X_c as $Q \propto X_c(1 - X_c)$, where the X_c is the 1D crystallinity defined as $X_c = \langle d \rangle / LP$.

Figures 2-7(a–c) show the time evolution of Q, LP and $\langle d \rangle$. The Q is the Fourier transform of the scattering intensity of every particle within the sample; the evolution of Q is only related to the fluctuation of the electron density. Which means during the phase transition of PBA, the evolution of Q is only related to the relative amount of the amorphous and crystalline component, which in another word, crystallinity. The Q of the β-phase became almost 0 immediately after the temperature jump. After 32 min, the Q of the α-phase increased gradually, which corresponds well to the result obtained from the time-dependent IR and WAXD analyses. The averaged lamellar thickness $\langle d \rangle$ and long period LP of the recrystallized α-phase are larger than those of the original β-phase. The $<d>$ and LP of the α-phase did not change remarkably with the passage of time once after the α-phase appeared from the melt. The 1D crystallinity X_c is almost the same before and after the transition process between the β and α phases, as shown in Figure 2-7(d). From the increment of Q value and the constancy of the 1D crystallinity X_c during the phase transition process, we may be able to assume that the number of the α-form lamellae increased gradually once when the α-form lamellae started to appear. But such a geometrical relation between $<d>$ and LP as X_c ($= <d>/LP$) was kept almost unchanged. This is not inconsistent with the increasing content of the α-form as detected in Figures 2-4 and 2-5.

It should be noted that the β-to-α phase transition mechanism *via* the molten state is not affected by the difference in the annealing temperature of the starting sample. In fact, we performed the similar temperature-jump experiment at 50 ℃ also, which was just below the T_m of the as-cast β-phase. The result is shown in Figure A1-2 in the Appendix 1. The melt-recrystallization phase transition phenomenon was detected as similarly to the above-mentioned case at 55 ℃.

Normal α-Phase and High-Temperature α-Phase

The SAXS data told us that the α-phase obtained through the melt-recrystallization at a high temperature shows the different higher-order structure from that of the α-form prepared by quenching the melt (Figure 2-7(c)) and (d)). The lamellar thickness and long period of the stacked lamellae are larger for the recrystallized high-temperature α-form crystals than those of the melt-quenched α-form crystals. As seen in Figure 2-8, the half-widths of the WAXD (110) and (020) diffraction peaks were found to be appreciably larger for the high-temperature α-form in the

temperature region of 50–60 ℃ (the WAXD profiles during the second heating process are shown in Figure A1-3 in Appendix 1). Therefore, we may have such an imagination for the recrystallized α-form existing at a high temperature that this crystal is more or less disordered in the chain packing mode although the thickness of the lamellae is larger. We may call this high-temperature α-phase the structurally disordered phase.

Conclusion

In the present study, the author have solved the long-term controversial problem about the β-to-α phase transition mechanism of PBA by using the techniques of the time-resolved measurements of the FTIR spectra as well as the simultaneous time-resolved WAXD/SAXS measurements in the quick and stable temperature-jumping measurements. From both the FITR and WAXD results, the direct phase transition of the β-phase to the α-phase does not occur but the transition occurs at the two stages; the melting of the β-phase into the amorphous phase and the subsequently occurred recrystallization of the amorphous phase into the α-form. The α-phase obtained by the melt-recrystallization of the original β-phase is different in the lamellar stacking structure and also in the degree of orderliness in the crystal lattice as judged from the SAXS and WAXD data analysis.

The PBA is one of the most representative biodegradable polymers. The degree of biodegradability depends on the two types of the crystal modification: the α and β phases. The control of the morphology or higher-order structure is affected sensitively by the generation of these crystal modifications. The basic knowledge about the crystalline phase transition behavior of the two types of crystal forms of PBA, which is revealed in the present research, will be useful for the development of PBA as a biodegradable environmentally friendly polymer material.

References

1. Vroman, I.; Tighzert, L. Biodegradable polymers. *Materials* **2009**, 2, 307–344.
2. Göpferich, A. Mechanisms of polymer degradation and erosion. *Biomaterials* **1996**, 17, 103–114.
3. Iwata, T. Crystal structure and biodegradation of aliphatic polyester crystals. *Macromol. Chem. Phys.* **1999**, 200, 2429–2442.
4. Zhao, L.; Wang, X.; Li, L.; Gan, Z. Structural analysis of poly(butylene adipate) banded spherulites from their biodegradation behavior. *Polymer* **2007**, 48, 6152–6161.
5. Takiyama, E.; Fujimaki, T. "bionolle", Biodegradable Plastic through Chemical Synthesis. *Stud. Polym. Sci.* **1994**, 150–174.
6. Nikolic, M. S.; Djonlagic, J. Synthesis and characterization of biodegradable poly(butylene succinate-co-butylene adipate)s. *Polym. Degrad. Stab.* **2001**, 74, 263–270.
7. Lindström, A.; Hakkarainen, M. Environmentally friendly plasticizers for poly(vinyl chloride)—Improved mechanical properties and compatibility by using branched poly(butylene adipate) as a polymeric plasticizer. *J. Appl. Polym. Sci.* **2006**, 100, 2180–2188.
8. Tserki, V.; Matzinos, P.; Pavlidou, E.; Panayiotou, C. Biodegradable aliphatic polyesters. Part II. Synthesis and characterization of chain extended poly(butylene succinate-co-butylene adipate). *Polym. Degrad. Stab.* **2006**, 91, 377–384.
9. Ren, J.; Fu, H.; Ren, T.; Yuan, W. Preparation, characterization and properties of binary and ternary blends with thermoplastic starch, poly(lactic acid) and poly(butylene adipate-co-terephthalate). *Carbohydr. Polym.* **2009**, 77, 576–582.
10. Anthierens, T.; Billiet, L.; Devlieghere, F.; Du Prez, F. Poly(butylene adipate) functionalized with quaternary phosphonium groups as potential antimicrobial packaging material. *Innovative. Food Sci. Emerging. Technol.* **2012**, 15, 81–85.
11. Tang, Y.; Xu, J.; Guo, B. Polymorphic Behavior and Enzymatic Degradation of Poly(butylene adipate) in the Presence of Hexagonal Boron Nitride Nanosheets. *Ind. Eng. Chem. Res.* **2015**, 54, 1832–1841.
12. Fuller, C. S.; Erickson, C. L. An X-ray study of some linear polyesters. *J. Am. Chem. Soc.* **1937**, 59, 344–351.

13. Fuller, C. S.; Frosch, C. J. X-ray investigation of the decamethylene series of polyesters. *J. Am. Chem. Soc.* **1939**, 61, 2575–2580.
14. Fuller, C. S.; Frosch, C. J. Further Investigation of the Chain Structure of Linear Polyesters. *J. Phys. Chem.* **1939**, 43, 323–334.
15. Fuller, C. S. The Investigation of Synthetic Linear Polymers by X-rays. *Chem. Rev.* **1940**, 26, 143–167.
16. Minke, R.; Blackwell, J. Polymorphic structures of poly(tetramethylene adipate). *J. Macromol. Sci., Part B: Phys.* **1979**, 16, 407–417.
17. Minke, R.; Blackwell, J. Single crystals of poly(tetramethylene adipate). *J. Macromol. Sci., Part B: Phys* **1980**, 18, 233–255.
18. Gan, Z.; Kuwabara, K.; Abe, H.; Iwata, T.; Doi, Y. The role of polymorphic crystal structure and morphology in enzymatic degradation of melt-crystallized poly(butylene adipate) films. *Polym. Degrad. Stab.* **2005**, 87, 191–199.
19. Gan, Z.; Kuwabara, K.; Abe, H.; Iwata, T.; Doi, Y. Metastability and Transformation of Polymorphic Crystals in Biodegradable Poly(butylene adipate). *Biomacromolecules* **2004**, 5, 371–378.
20. Gan, Z.; Abe, H. Temperature-Induced Polymorphic Crystals of Poly(butylene adipate). *Macromol. Chem. Phys.* **2002**, 203, 2369–2374.
21. Kai, W.; Zhu, B.; He, Y.; Inoue, Y. Crystallization of poly(butylene adipate) in the presence of nucleating agents. *J. Polym. Sci., Part B: Polym. Phys.* **2005**, 43, 2340–2351.
22. Woo, E. M.; Yen, K. C.; Wu, M. C. Analysis of multiple melting behavior of spherulites comprising ring-band shell/ringless core in polymorphic poly(butylene adipate). *J. Polym. Sci., Part B: Polym. Phys.* **2008**, 46, 892–899.
23. Yan, C.; Zhang, Y.; Hu, Y.; Ozaki, Y.; Shen, D.; Gan, Z.; Yan, S.; Takahashi, I. Melt Crystallization and Crystal Transition of Poly(butylene adipate) Revealed by Infrared Spectroscopy. *J. Phys. Chem. B* **2008**, 112, 3311–3314.
24. Sun, X.; Pi, F.; Zhang, J.; Takahashi, I.; Wang, F.; Yan, S.; Ozaki, Y. Study on the Phase Transition Behavior of Poly(butylene adipate) in its Blends with Poly (vinyl phenol). *J. Phys. Chem. B* **2011**, 115, 1950–1957.
25. Sun, X.; Liu, J.; Takahashi, I.; Yan, S. Melting and β to α transition behavior of β-PBA and

the β-PBA/PVPh blend investigated by synchrotron SAXS and WAXD. *RSC Adv.* **2014**, 4, 39101–39109.

26. Li, Q.; Zhou, J.; Chai, L.; Memon, J.; Ren, Z.; Li, H.; Sun, X.; Yan, S. The effect of the poly(vinyl phenol) sublayer on the melting behavior of poly(butylene adipate) crystals. *Polym. Chem.* **2014**, 5, 4293–4303.
27. Ratri, P. J.; Tashiro, K. Phase-transition behavior of a crystalline polymer near the melting point: case studies of the ferroelectric phase transition of poly(vinylidene fluoride) and the β-to-α transition of trans-1, 4-polyisoprene. *Polym. J.* **2013**, 45, 1107–1114.
28. Tashiro, K. Crystal Structure and Phase Transition of PVDF and Related Copolymers, In *Ferroelectric Polymers: Chemistry, Physics, and Technology*; Nalwa, H. S., *Ed.*; Marcel Dekker Inc.: New York, 1995; Chapter 2, pp 63–182.
29. Yoshioka, A.; Tashiro, K. Thermally-and solvent-induced crystallization kinetics of syndiotactic polystyrene viewed from time-resolved measurements of infrared spectra at the various temperatures (1) estimation of glass transition temperature shifted by solvent absorption. *Polymer* **2003**, 44, 6681–6688.
30. Strobl, G. R. *The Physics of Polymers: Concepts for Understanding Their Structures and Behavior*; Springer: Berlin, 2007.

Table 2-1. Assignments for IR Absorbance Bands of PBA in the Region of 1000–700 cm^{-1}

assignments	wavenumber (cm^{-1})
β-form crystal	930
	911
	735
α-form crystal	909
	734
amorphous	760
	745

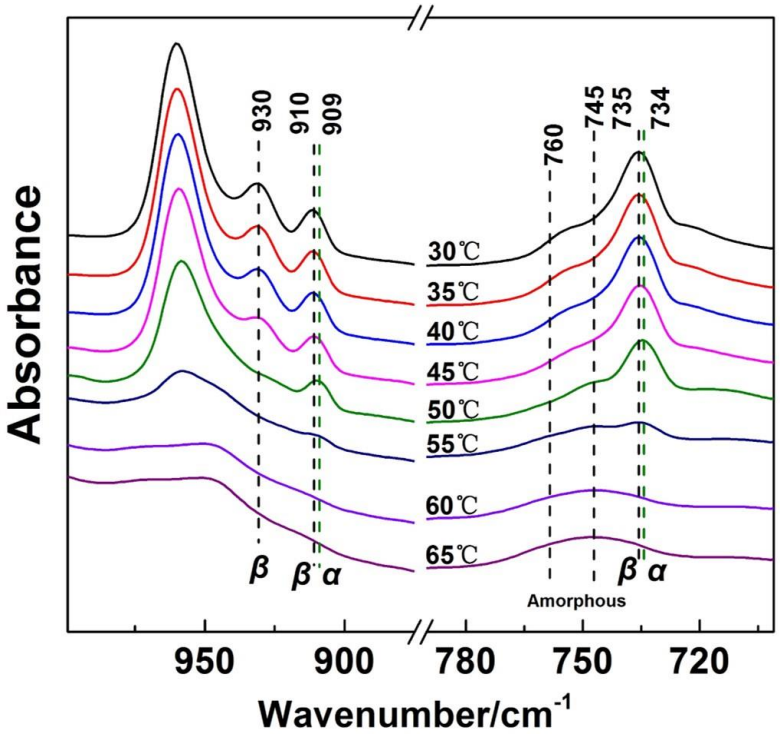

Figure 2-1. Temperature-dependent FTIR spectra of PBA as-cast film in the region of 1000–700 cm^{-1} over a temperature range of 25–70 ℃ at a heating rate of 1 ℃/min.

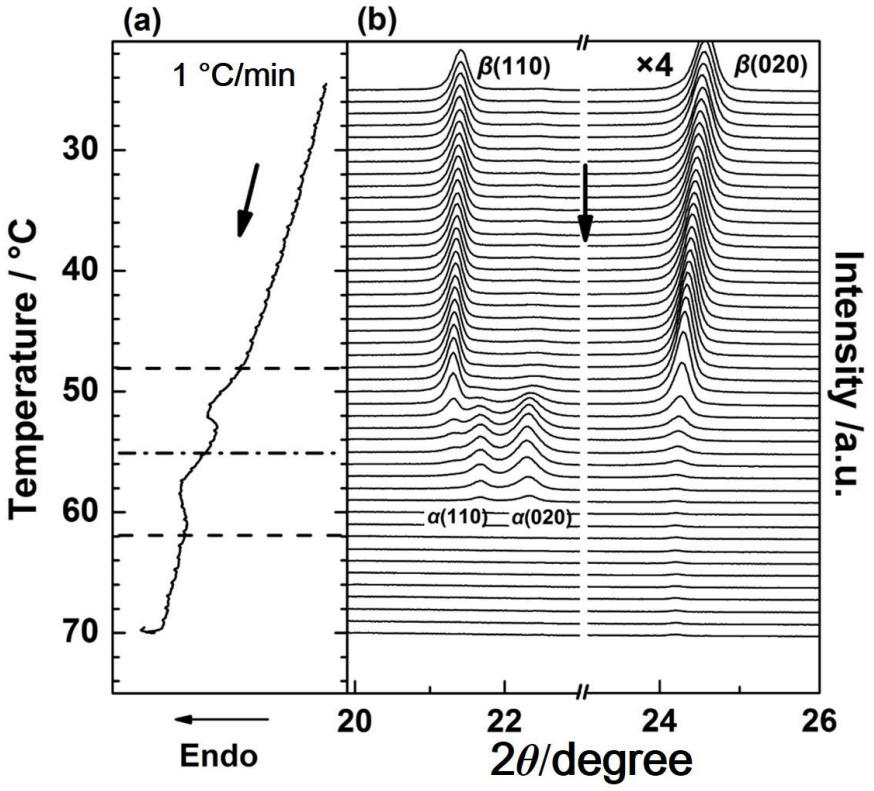

Figure 2-2. Simultaneous measurements of (a) DSC curve and (b) WAXD profiles of the as-cast film during first heating process from 25 to 70 ℃ at a heating rate of 1 ℃/min.

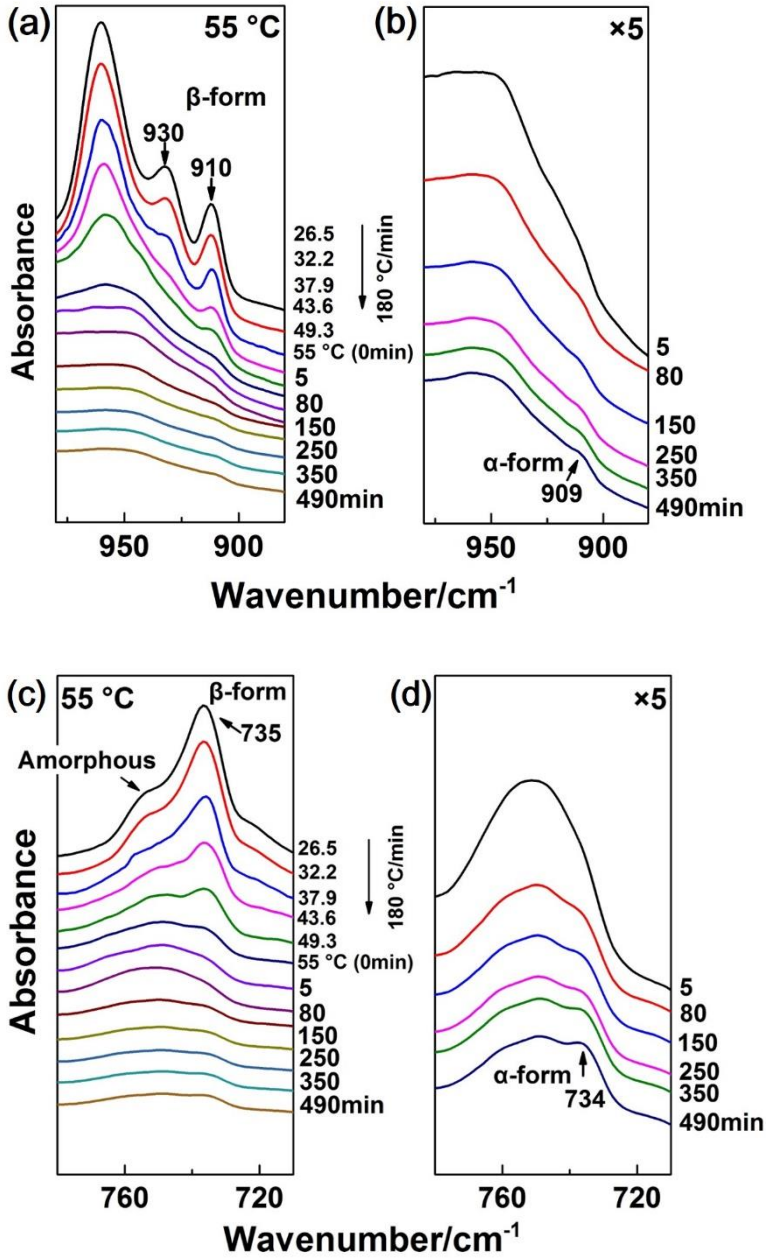

Figure 2-3. Temperature-jump time-dependent FTIR spectra for the as-cast PBA film at 55 ℃ in the region of (a) and (b) 980–850 cm^{-1} and (c) and (d) 790–700 cm^{-1}.

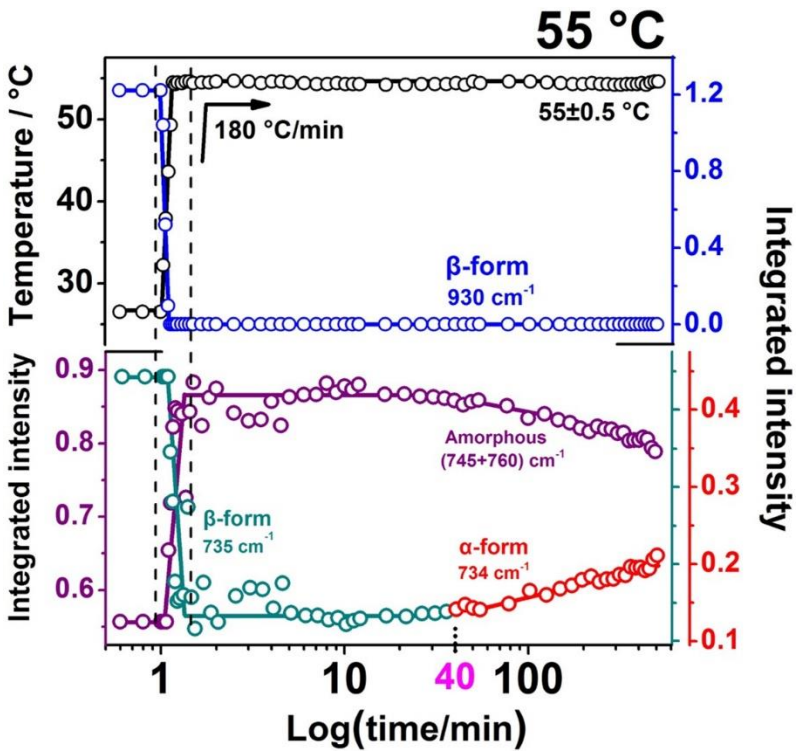

Figure 2-4. Temperature-jump time-dependent FTIR absorbance for the as-cast PBA film at 55 ℃ estimated for the IR bands of the *β*, *α*, and amorphous phases. The temperature of the sample was raised steeply to 55 ℃ at around 1 min after the start of the IR measurement and kept there at the fluctuation of 0.5 ℃. The increasing rate of the temperature was 180 ℃/min. The IR band of the *β*-form decreased quickly as the temperature was increased rapidly and became quite weak when the temperature reached at 55 ℃. On the other hand, the amorphous band intensity increased in parallel and was kept almost constant for a while. About 40 min later after the temperature jump, the intensity of the amorphous band started decreasing and the *α*-form IR band started to appear and increased.

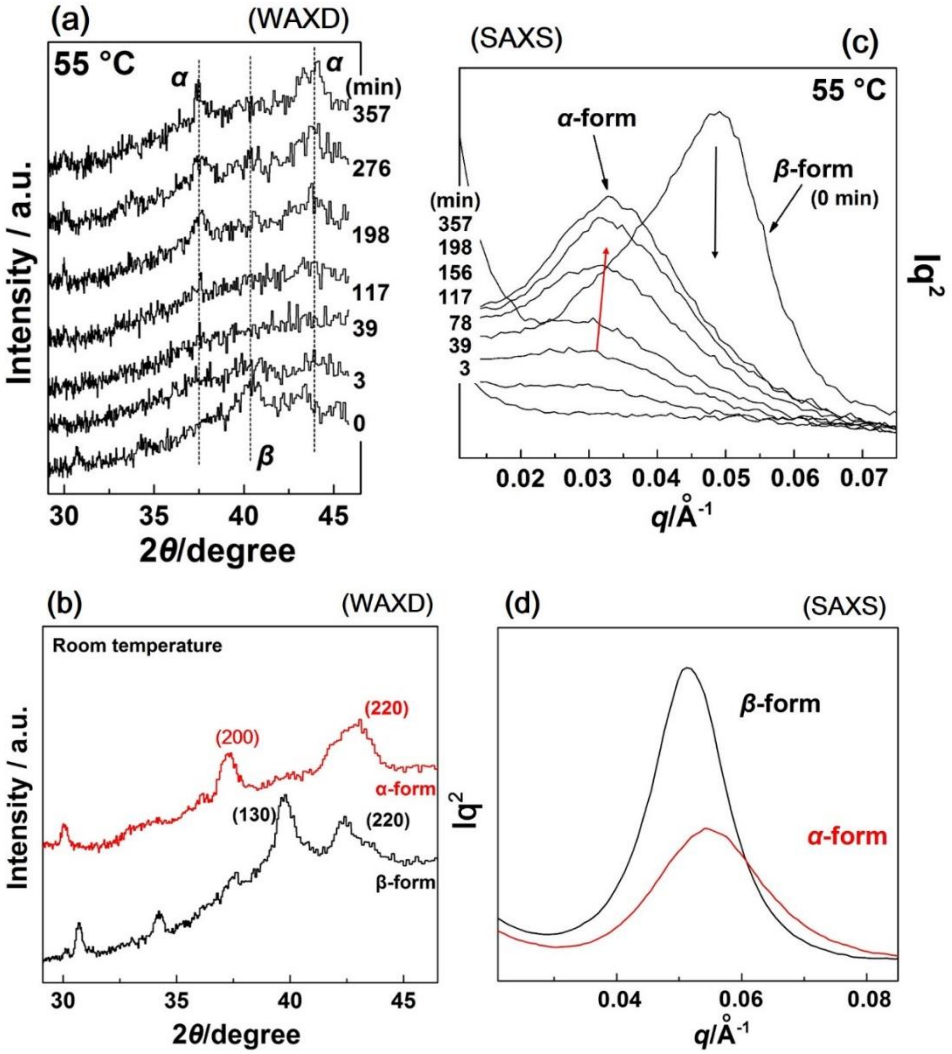

Figure 2-5. Temperature-jump time-dependent (a) WAXD and (b) SAXS profiles for PBA as-cast film at 55 ℃; (c) WAXD and (d) SAXS profiles for PBA with original β- or α-form crystals.

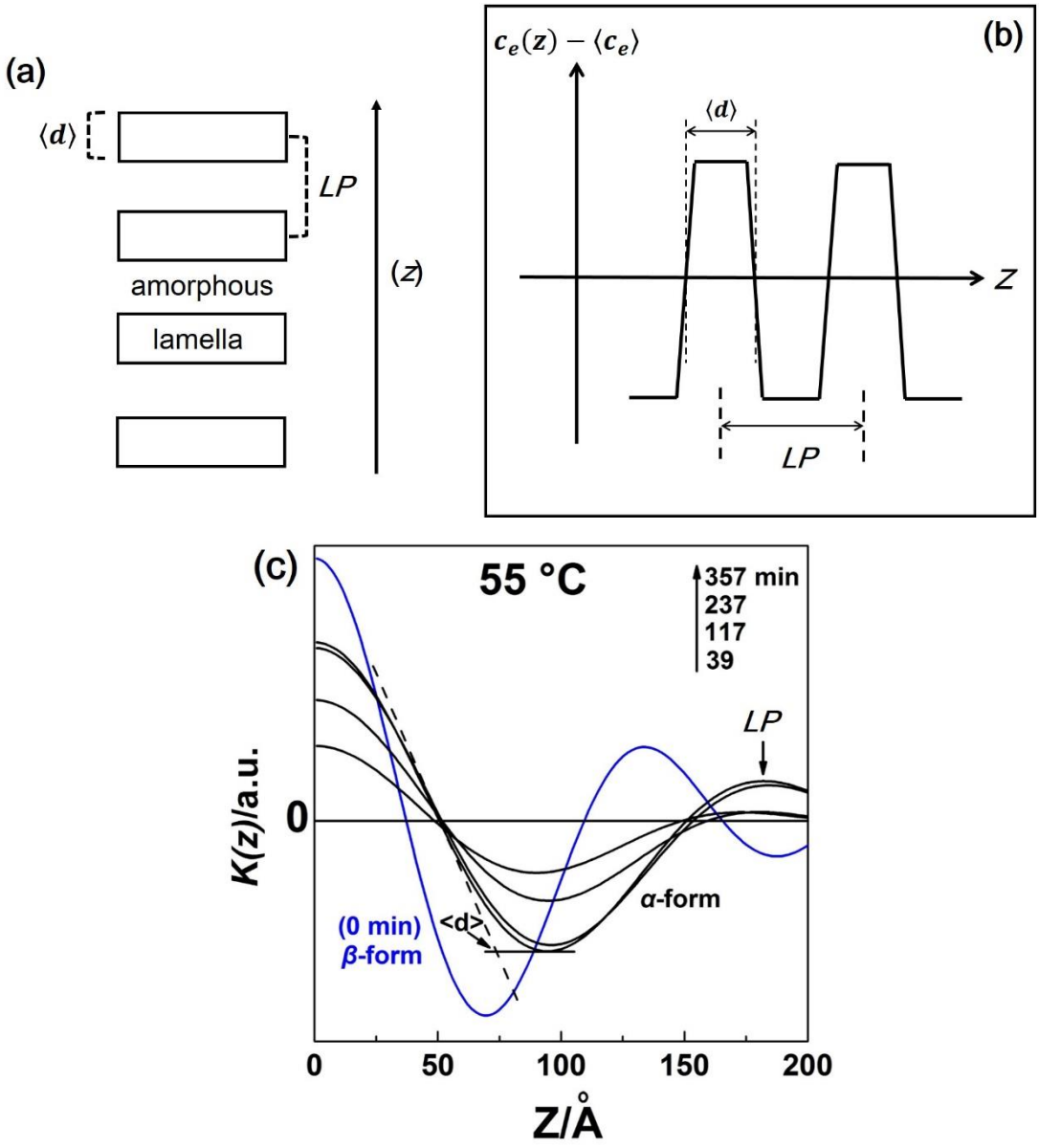

Figure 2-6. (a) Illustration of the stacked lamellae structure. (b) A model of electron density distribution along the stack normal. (c) The time dependence of the correlation functions calculated for the as-cast PBA film at 55 ℃.

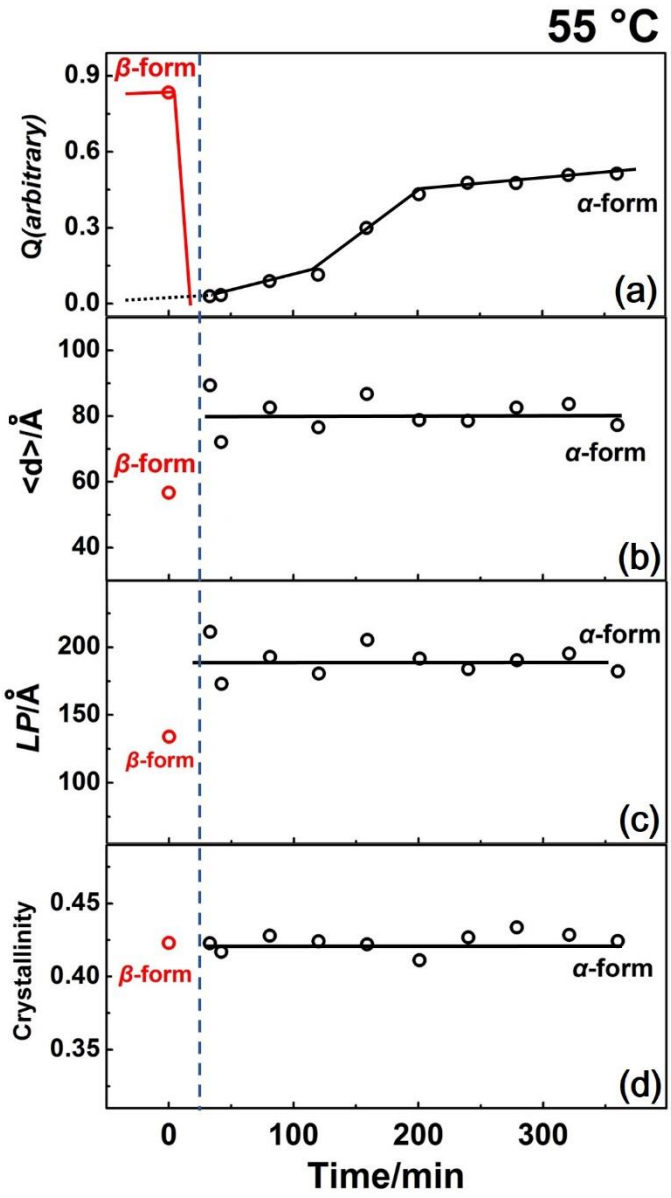

Figure 2-7. Temperature-jump time-dependent evolution of (a) scattering invariant Q, (b) average lamellar thickness $\langle d \rangle$, (c) long period (LP), and (d) the apparent 1-dimensional (1D) crystallinity.

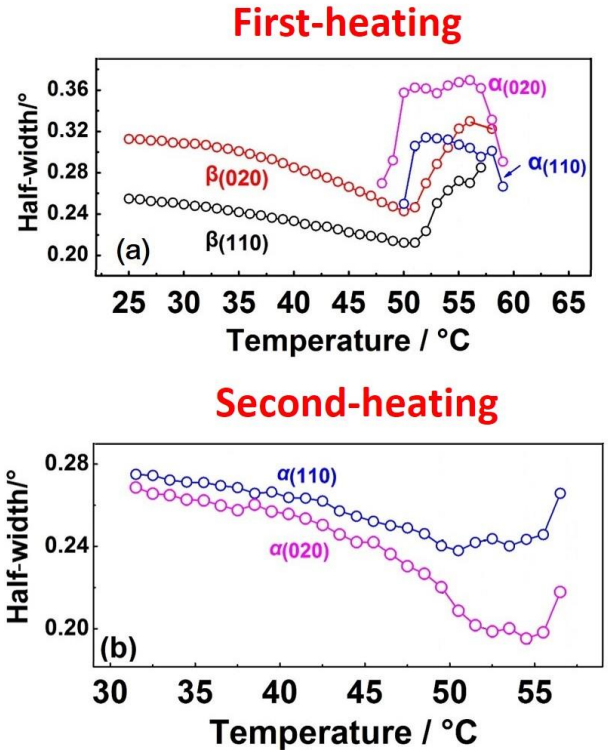

Figure 2-8. Half-width evolution of (a) β(110), β(020), α(110), and α(020) during first heating process and (b) α(110) and α(020) in the second heating process.

Appendix 1

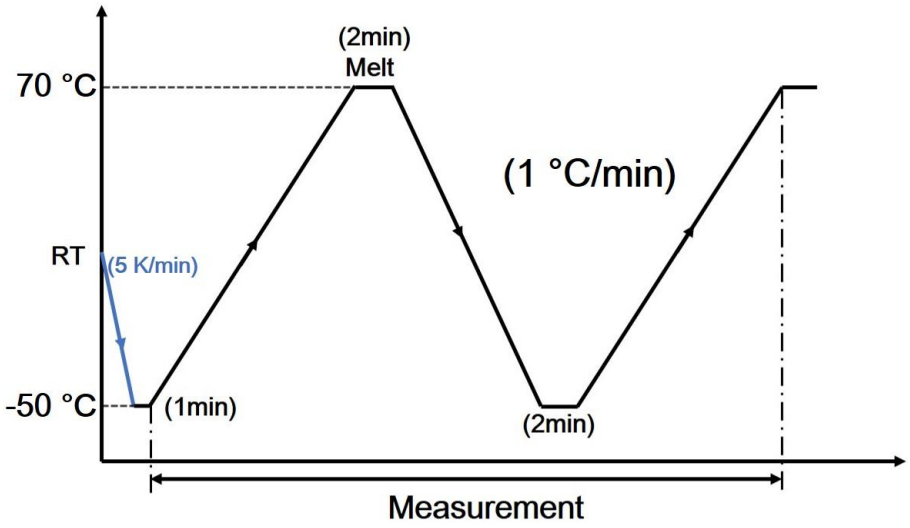

Figure A1-1. Thermal program used for the DSC-WAXD simultaneous measurements of the as-cast film.

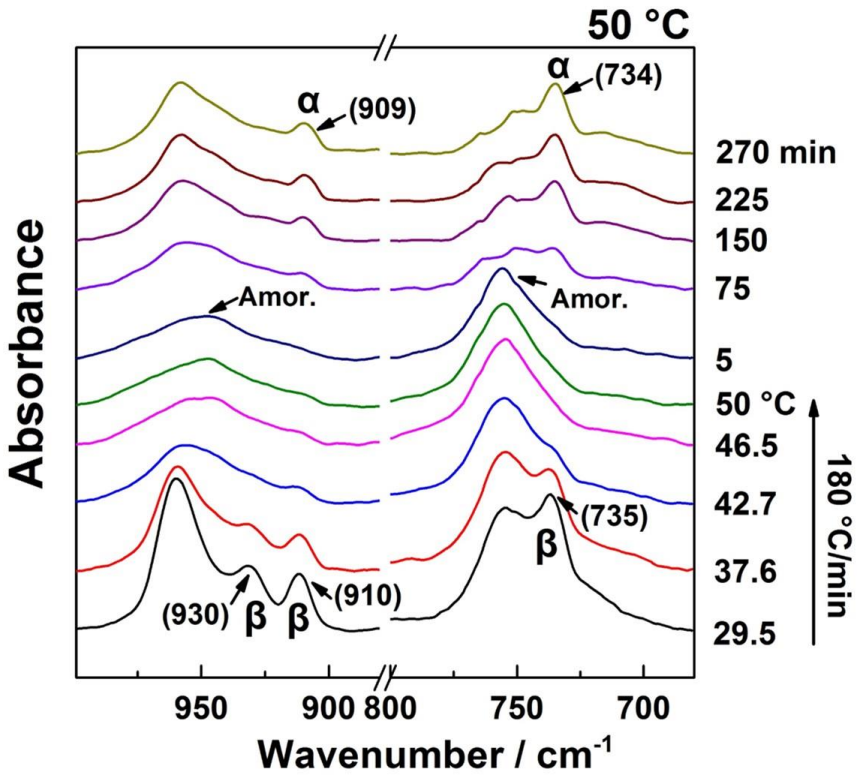

Figure A1-2. Temperature-jump time-dependent FTIR spectra for the as-cast PBA film at 50 ℃ in the region of 1000–680 cm^{-1}.

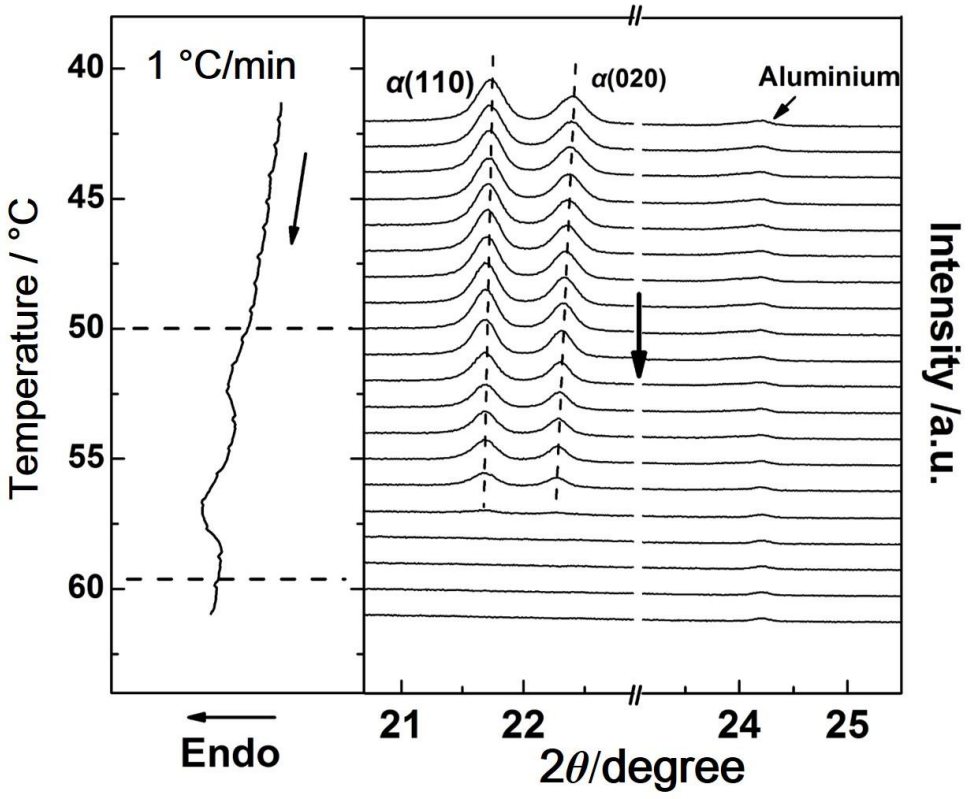

Figure A1-3. Simultaneous measurements of (a) DSC curve and (b) WAXD profiles for the as-cast film during second heating process from 40 to 70 ℃ at a heating rate of 1 ℃/min.

Chapter 3

Distribution of Polymorphic Crystals in the Ring-Banded Spherulites of Poly(butylene adipate) Studied Using High-Resolution Raman Imaging

ABSTRACT

Poly(butylene adipate) (PBA), an important biodegradable polymer, can crystallize into a particular type of ring-banded spherulite, in each of which two crystal forms, α and β, coexist. However, the distribution of the polymorphic crystals and the molecule chain orientation within the ring-banded PBA spherulites are still unclear. To determine these, Raman spectroscopy and high spatial resolution Raman imaging were used. Characteristic Raman peaks were identified for both the α and β forms and for amorphous structure. Using these peaks, the author investigated the polymorphic crystal distribution and molecular chain orientation within the spherulites through Raman imaging. The two crystal forms are found to be unevenly distributed in the center, ring-banded and out-layer ringless region. The results of this study also suggested that the two crystal forms can nucleate and grow in the same temperature range (31–33 ℃), but the relative content of the α-form in the ring-banded region becomes higher with the higher crystallization temperature. Polarized Raman images for the ring-banded spherulite shows both bow-tie and ring-banded patterns, which means that the molecular chains in the ring-banded region orient not only about the radial direction of the spherulites but also about the substrate plane. The present study shows that Raman imaging is a very powerful technique in polymer crystal structure research.

Introduction

Spherulites have spherically symmetric crystal colonies, and spherulitic morphologies are the most common crystal morphologies.[1-4] For polymeric materials, spherulites are usually formed when they are crystallized from viscous melts[5-9] or deposited from a solution.[10,11] Some polymers can form different spherulite patterns under different crystallization conditions.[12-17] In the case of poly(butylene adipate) (PBA, $-[-O(CH_2)_4OOC(CH_2)_4CO-]_n-$; see Figure A2-1 in the Appendix 2), it can form ring-banded or ringless spherulites when isothermally crystallized at different temperatures from the melt.[17-19]

PBA is a representative biodegradable synthetic linear aliphatic polyester that has good tensile properties and potential applications as an ecofriendly material.[20-22] Two polymorphs of PBA can develop depending on the crystallization conditions;[23-27] the α-form is characterized by an axially compressed planar zigzag conformation and is packed as a monoclinic unit cell, while the β-form with a planar zigzag conformation, is packed as an orthorhombic unit cell. Isothermal crystallization behavior of PBA from the melt was first reported by Gan et al.[24] They found out that the pure β-form is formed below 29 ℃, while the pure α form is formed above 31 ℃, and that both crystal structures form simultaneously (a mixture of α- and β-form crystals) at 30 ±1 ℃. What is more interesting is that the formation of the ring-banded PBA spherulites and the formation of mixed crystals occur in similar temperature ranges,[19] which means that the α- and β-form crystals will have some distributions within the ring-banded spherulites system. However, pure α- or β-form crystals can only form ringless pattern. Therefore, the following questions arise: how are these two crystal forms distributed and how do PBA molecular chains orient within the spherulite system? Note that the microstructures of PBA play a significant role in its properties, such as its mechanical properties and biodegradability. Therefore, it is essential to answer these questions.

The relationship between the ring-banded pattern, polymorphic crystals, and lamellar orientation of PBA has been studied extensively.[17-19,28-30] Evidence has shown that the mixture of the two crystal forms is not the fundamental reason for the formation of the ring-banded PBA spherulites.[17,28] However, since the ring-banded PBA spherulite consists of two types of crystal forms, it is reasonable to speculate that the distribution and relative content of the α- and β-form crystals will affect the mechanical properties and biodegradability of PBA. Thus, investigating the

distribution of the two types of crystal forms is of utmost importance. Moreover, PBA is also a unique model for studying the ring-banded spherulite system with polymorphic crystals. To our knowledge, only one study has suggested that the α- and β-form crystals were alternately distributed in the ring-banded region.[19] However, they did not provide any direct evidence.

Periodic ring-banded spherulites have been attracting considerable attention for several decades owing to their unique morphological features,[1,2,31] and a vast majority of spherulite studies rely on polarized optical microscopy (POM). Interpretations of the Maltese cross, the concentric rings, and light-scattering patterns can provide important information about the structures of spherulites;[2] however, POM cannot give detailed information on the internal structures. Vibrational spectroscopy and X-ray crystallography can yield more information about crystal structures, such as the conformation and the orientation of the chain polymer molecules and crystal system. In fact, there have already been many studies on PBA crystal structures in which these methods were used.[23-27,32-36] However, the conventional vibrational spectroscopy and X-ray analysis can only give average information about the sample as a whole, which does not provide enough spatial information for a deep exploration of the ring-banded spherulites.

If we could directly "see" the molecular orientation and the distribution of the polymorphic crystals, a better understanding of the ring-banded PBA spherulite will be achieved. Chemical imaging techniques, which combine macro morphology with micro molecular information should be a powerful tool for this purpose. In recent years, chemical imaging techniques have been utilized more in research about polymer science and engineering,[37-50] and Fourier transform infrared spectroscopic (FTIR) imaging is used in the majority of these studies since it can be easily proceed. However, FTIR imaging is not always suitable for studies on ring-banded spherulites. This is because the spatial resolution of FTIR imaging is usually around 5.5 μm,[42,44,47,48,51] but the band spacing of ring-banded spherulites for some polymers is very small, such as that of PBA, which is around 4–5 μm.[52] Therefore, FTIR imaging does not always have sufficient resolution to allow concave and convex structures within the ring-banded spherulites to be distinguished from each other. In addition, in the FTIR spectrum of PBA, only the β-form crystal has a clearly characteristic peak (at around 930 cm^{-1}),[33,35] while the α-form crystal does not, so FTIR imaging cannot clearly reveal the distribution of the polymorphic crystals of PBA.

Compared to FTIR imaging, Raman imaging can give much better spatial resolution (0.3 μm

in present research), and it can also provide marked information about the molecular structure.[52-56] Unger et al.[55] investigated the phase-separation behavior in a poly(3-hydroxybutyrate) (PHB) and poly(L-lactic acid) (PLLA) blend by Raman and FTIR imaging. They found that the size of the PHB-rich domains from Raman imaging was only about 1–20 μm at 25 ℃, while a result of 50 μm was obtained from FTIR imaging. The fact that Raman imaging has better spatial resolution than FTIR imaging was responsible for the differences in these results. Likewise, Martin et al.[56] successfully distinguished the spherulites with α- or β-form crystals of isotactic polypropylene (iPP) within one iPP slice by Raman imaging with spatial resolution of about 1 μm.

Thus, Raman imaging is very suitable for investigating PBA spherulites. However, to the best of our knowledge, no detailed Raman studies on PBA, particularly, the polymorphic crystals of PBA, have been reported thus far. Therefore, in present study, Raman spectroscopy and Raman imaging were used to explore the PBA spherulites for the first time. The following interesting points were achieved from the present study. (1) Both α- and β-form crystals, as well as the amorphous structure, have their own characteristic Raman peaks. (2) The α- and β-form crystals of PBA are unevenly distributed within the center, ring-banded and out-layer ringless region; in the center and ring-banded region, the two crystal forms are coexisted, while the α-form crystals are dominated in the out-layer ringless region. The two crystal forms grow together when the ring-banded spherulites are formed, but their relative content shows temperature dependence in the center and ring-banded region. (3) The molecular chains in the crystalline domains within the spherulites are not only all oriented perpendicular to the radial direction of the spherulites, but they display periodical orientation changes with regard to the substrate plane as well. This corresponds to the results from previous studies that a ring-banded PBA spherulite arises from the twisting of the lamellar structure along the radial growth direction of the spherulite.

Experimental Section

Materials and Sample Preparation

PBA (molecular weight (MW) = 12000 g/mol) was purchased from Polysciences, Inc. and used without further purification. A homogeneous solution with a concentration of 1 wt % was prepared by dissolving PBA in hot chloroform. PBA films were prepared by casting the solution on microscope glass slides for Raman imaging measurements and POM observation or on Si (100) wafers for wide-angle X-ray diffraction (WAXD) at room temperature (RT). After most of the solvent had evaporated, the glass slides and Si wafers were covered with cover glasses, and then melted on a hot stage at 80 ℃ for 5 min to erase any memory effects.[57] The melted sample was then immersed promptly and isothermally crystallized in a water bath that was at the desired temperature. After spherulite growth, the samples were quickly cooled in ice water and stored in a refrigerator until Raman imaging, POM, and WAXD measurements were performed. All the above measurements were carried out after gently removed the cover glass on the top-surface of the PBA film. The thickness of the PBA films was ~10 μm. The PBA spherulites that were grown at different temperatures are designated hereafter as "PBA*X*," where *X* represents the isothermal crystallization temperature; for example, PBA28 indicates PBA spherulites grown in a water bath at 28 ℃.

For temperature-dependent Raman measurements, a PBA film was prepared by casting the PBA chloroform solution on a cover glass.

POM, WAXD, and Raman Measurements

The PBA spherulites that were crystallized at different temperatures were observed at room temperature using an optical microscope (Olympus BX50, Japan) equipped with a crossed polarizer and a 530 nm sensitive tint (full-wave) plate (U-TP530, Olympus, Japan) as well as a digital camera system (DP21, Olympus, Japan) to take polarized optical micrographs. WAXD profiles were recorded at room temperature on a Rigaku SmartLab with Cu Kα_1 radiation (λ = 1.5418 Å); the scan rate was 3 °/min and the step size was 0.05 °.

Temperature-dependent Raman measurements were performed at different temperatures using a Horiba LabRAM HR-800 Raman spectrophotometer with holographic grating of 1800

grooves/mm and equipped with a 514.5 nm Ar ion laser, a charge-coupled device (CCD) detector, and a 100×/0.9 numerical aperture (NA) objective lens. Raman spectra were obtained with an exposure time of 10 s and an effective laser power of 5 mW. The spectral resolution was 0.5 cm^{-1}. The temperature was controlled using an Oxford MercuryiTC system, and the sample was placed inside an optical microscopy variable-temperature cryostat (Microstat He2, Oxford). The Raman spectrum of pure β-form PBA crystals was obtained by measuring the as-cast sample directly at room temperature, and then the sample was heated to 80 ℃ at 1 ℃/min so that the Raman spectrum of the pure amorphous structure could be measured. Afterward, the sample was cooled slowly to room temperature at 1 ℃/min so that the spectrum of pure α-form crystals could be obtained.

Raman imaging measurements based on the confocal technique, which allowed for high spatial resolution were conducted using a Renishaw inVia Raman spectrometer system with a grating of 1800 gr/mm and equipped with a 532 nm solid-state laser, 50×/0.75 NA objective lens, Renishaw CCD detector, and Leica DM2500 upright microscope with a computer-controlled motorized stage for *XY* imaging. A linear polarizer and a half-wave plate were also inserted between the laser and the sample for the polarization measurements. Two different polarizer angles, 0 ° and 90 °, were used, and the corresponding polarization geometries (Porto notation) were $Z(X, XY)\bar{Z}$ and $Z(Y, XY)\bar{Z}$, respectively, on the *XYZ* Cartesian coordinates system, where the *X* and *Y* directions were parallel to the sample surface while the *Z* direction was perpendicular to the sample surface (see Figure A2-2 in the Appendix 2). The imaging was conducted in point-by-point mode. In Raman imaging, the laser was focused on the sample surface, the sample stage moved automatically, and Raman signals generated from the sample were collected by the CCD detector. The exposure time for each point was 0.4 s and the effective laser power was 10 mW. The spectral resolution was 1.5 cm^{-1}. The spatial resolution was approximately 0.35 μm in the *XY* plane ($R = \lambda/2NA$,[58] where *R* is the maximum spatial resolution). Every spectrum was collected at a 0.35 μm grid, but the final imaging areas were decided based on the size of the spherulites of different samples.

Analysis of Raman imaging data was performed using the Renishaw WiRE 4.2 software. Before the calculation of each Raman image, all of the Raman peaks that were used were truncated and then corrected by subtracting the baseline. Raman peak areas were calculated by integrating the areas between the Raman peaks and the baseline. Raman peak positions were determined by

curve fitting under Gaussian function.

Results and Discussion

Polymorphic Behaviors and Spherulite Morphologies of PBA Isothermally Melt-Crystallized at Different Temperatures

Figures 3-1(a–j) show POM images of PBA26–35. These samples exhibited different spherulite morphologies depending on the crystallization temperature, as summarized in Figure 3-1(k). The typical ringless spherulites were formed below 29 ℃ (zone 1 in Figure 3-1(k)) and above 34 ℃ (zone 4), whereas more complex patterns consisting of ring-banded with out-layer ringless textures were obtained after the isothermal melt crystallization at 31–33 ℃ (zone 3), as shown by the white and black arrows, respectively, in Figure 3-1(h). The POM image of PBA crystallized at 30 ℃ (zone 2) displays semi-banded spherulites with irregular alternately distributed bright and dark regions; the texture seems to be intermediate between the ringless and banded spherulites.

WAXD profiles of PBA films that were treated under the same conditions as those used for the samples examined using POM are shown in Figure 3-2. The results reveal that pure β- and α-form crystals were formed when PBA was crystallized below 29 ℃ and above 34 ℃, respectively. At 29–33 ℃, the β- and α-form crystals coexist, and as the crystallization temperature increases, the intensity of the α(020) diffraction peak increases, while that of the β(020) peak decreases. It is noted that the relative diffraction intensities of α(110)/α(020) and β(110)/β(020) are also different for PBA26–35. For the films with pure β- and α-form structures, the intensity of the (110) peak is much higher than that of the (020) peak; however, for the films with mixed crystal structures, the intensity of the (110) peak is much lower than that of the (020) peak. Since the WAXD measurements in the present study were performed in the reflection mode, in this geometry, only the crystal lattice planes that are oriented parallel to the substrate contribute to the intensity of Bragg diffraction. Therefore, it is suggested based on Figure 3-2 that the orientation of the crystal structure for the ring-banded spherulites is different from that of ringless spherulites, and this may be related to lamellar twisting, which will be discussed in the following section.

The results of POM observation and the WAXD profiles from the present study are almost identical to those from previous studies, which have been mentioned in the Introduction, except for those of Zone 3. The previous works only reported that a PBA film with mixed crystal

modifications forms a banded pattern, but not a ring-banded spherulites with an out-layer ringless region.[29] A similar ringless-banded mixed pattern was reported by Liu et al.;[17] they used a low-MW sample (MW = 5.2k) and grew spherulites at 30 ℃. The growth of the low- MW PBA sample showed a ringless pattern initially, then a ring-banded pattern, and finally a ringless pattern again (see Figure 17 in ref. 17). The ringless and ring-banded parts were composed of the α and β forms, respectively. However, in contrast to the results of the present study, a pure β-form crystal formed ring-banded spherulites in their study when PBA was crystallized at a lower temperature. Moreover, their POM images clearly showed that the ring-banded spherulite was formed through β-form nucleation at the edge of ringless spherulites (α-form). Therefore, there should be another reason for the formation of the ring-banded pattern of PBA in the present study. It should be noted that the out-layer ringless region is not belong to the ring-banded PBA spherulite in the present work, the reason will be discussed in the following section.

Polymorphic Crystal Distribution within Ring-Banded PBA Spherulites

Figure 3-3(a) displays the 1900–700 cm^{-1} region of the Raman spectra of the amorphous state and the α and β crystals of PBA. Peaks due to backbone stretching and CH_2 rocking modes are mostly located in the 1000–700 cm^{-1} region, while peaks in the 1600–1000 cm^{-1} region are mainly attributed to the C–O–C stretching modes and CH_2 wagging mode, and a peak arising from the C=O stretching mode is observed at 1733 cm^{-1}.[59]

Figure 3-3(a) shows that most of the Raman peaks of pure α- and β-form crystals are located in nearly the same positions, and thus, peaks due to both forms are difficult to distinguish from each other. Only the relative intensities of some peaks are different, and they are correlated with the different crystal structures and the different orientations of the molecular chains.[56,60,61] The Raman spectrum of the amorphous structure shows some different characteristics from those of the crystal structures. For example, a peak at 985 cm^{-1} is observed only in the spectra of the crystal structures, while a peak at 1142 cm^{-1} shows up only when PBA is in the amorphous state. Interestingly, in the 1300–1150 cm^{-1} region (Figure 3-3(b)), characteristic peaks for the β- and α-form crystals and the amorphous structure are found at 1268 (blue line), 1185 (red line), and 1211 cm^{-1} (brown line), respectively. In the 1260–1230 cm^{-1} region, the spectra of both types of structures show Raman peaks; the spectra of the β-form crystal and amorphous structure show a

peak at 1245 cm^{-1}, and that of the α-form crystal shows a peak at 1247 cm^{-1}. Since the 1245 and 1247 cm^{-1} peaks are near each other, they combine to form one peak in the Raman spectra, and this peak is designated hereafter as the C-peak. The characteristic Raman peaks of PBA are listed in Table 3-1. These peaks will be used in Raman imaging analysis. Note that the current assignments are merely tentative and that more detailed and accurate peak assignments for PBA should be made in conjunction with the computational simulation, which need a further work.

Since PBA32 contains the most typical ring-banded texture, as shown in Figure 3-1(g), it was selected for the examination of the formation mechanism of the interesting spherulite patterns of PBA. Figures 3-4(a and b) show an optical image and the Raman imaging results of PBA32, respectively. The author obtained polarized Raman images with both 0 ° and 90 ° polarization, which gives us information not only about the molecular structure, but also about the molecular chains orientation. The images generated from the integrated areas of the C-peak, α-form peak (1185 cm^{-1}), and β-form peak (1268 cm^{-1}), respectively, are presented in Figure 3-4(b). Figure 3-4(b) shows that the crystal structure is distributed throughout the area, which means that the system is highly crystalline. Note that the surface topography fluctuation of PBA32, for example, different heights in the center, ring-banded, or edge regions of the spherulite, will not significantly affect our Raman results since the fluctuations were reported to be less than 100 nm,[19] which is much smaller than the laser penetration depth (more than 1 μm) in the present study. The distribution of the amorphous structure is not shown since the intensity of the 1211 cm^{-1} peak due to the amorphous structure is too low; moreover, since the intensity of the amorphous peak at 1245 cm^{-1} is much lower than that of the 1211 cm^{-1} peak (shown in Figure 3-3(b)), it will not affect the integrated area of the C-peak, even though they are overlapped. It was noted that the α- and β-form crystals are abundant in the out-layer and ring-banded region, respectively, in PBA32, as shown in Figure 3-4(b). Moreover, the patterns for both the β- and α-form peak areas and C-peak areas show polarization dependence, which is due to the molecular chains orientation within the spherulite, and this will be elucidated in the following section.

Since the values of peak areas are affected by the molecular chains orientation, therefore Raman images of peak areas cannot reflect the real polymorphic crystals distribution. To eliminate such effect on the result of the polymorphic crystals distribution, images were generated from the Raman peak position obtained through curve fitting of the C-peak (examples of curve fitting are

shown in Figure A2-3 in the Appendix 2) and are shown in Figure 3-4(b). As mentioned above, the C-peak is composed of both the α- and β-form peaks (the amorphous peak at 1245 cm^{-1} can be ignored since it is too weak to be detected). Its position is mainly related to the relative content of the α- and β-form crystals, since the orientation of the molecular chains within the crystalline domains should be similar at every measuring spot. For example, if the β-form crystals are much more abundant than the α-form crystals, the C-peak will be near 1244 cm^{-1}; on the other hand, this value will be closer to 1247 cm^{-1} when the α-form crystals are more abundant. Thus, the C-peak position will appear at different values in different spots, depending on the relative content of the α- and β-form crystals. Therefore, the Raman image based on the C-peak position is suitable for investigating the distribution of the polymorphic crystals.

The C-peak position obtained from the center region of the spherulite is different from those obtained from other regions and is between those from the ring-banded (1244.5 cm^{-1}) and out-layer ringless (1247 cm^{-1}) regions. This means that the α-form crystals exist in the center region. The images of the C-peak position and the α-form peak area are comparable to each other, because both show a similar distribution of the α-form crystals. This also demonstrates that using the C-peak position to investigate the polymorphic crystals distribution is reasonable. The 1280–1170 cm^{-1} region of the polarized Raman spectra of the center region (**#1**), the flat-on (**#2**) and edge-on (**#3**) domains of the ring-banded region, and the out-layer ringless region (**#4**) of the spherulites in Figure 3-4(a) are shown in Figures 3-4(c and d). It is clear that the α-form peak is more apparent in regions **#1** and **#4** than in regions **#2** and **#3**, but the opposite is true for the β-form peak. The formation of the spherulite occurs through nucleation, and the Raman imaging results for PBA spherulites in this study suggest that the β- and α-form crystals can nucleate at the same time at 32 ℃.

To study the ring-banded PBA spherulites further, the author carried out time-dependent in situ observation of the crystallization of PBA32 using POM, and the results are shown in Figure 3-5. The crystallization process was complete within 60 s, and nucleation began at around 9 s. The ring-banded patterns appeared just after the formation of the crystal nuclei, as indicated by the white arrow, “A”, in Figure 3-5. Liu et al.[17] found that the transformation from ringless to ring-banded PBA spherulites began from several crystal nuclei of ring-banded spherulites formed at the edge of ringless spherulites. In the present study, however, it was difficult to see whether any

nucleation point was formed before the ring-banded spherulites appeared in Figure 3-5. Moreover, the subsequent growth process of the ring-banded pattern is very smooth, and the pattern grows at the entire periphery of the crystal nucleus. After the ring-banded spherulites had grown to some extent, the out-layer region started to appear, and it grew instead of the ring-banded spherulites until crystallization was complete. The growth rate of the ring-banded spherulites, calculated from the increase in the diameter, is shown in the blue region of Figure 3-6. It can be seen from Figure 3-6 that the growth rate increases conspicuously to approximately 5 μm/s until approximately 18 s, and then decreases to approximately 1 μm/s, and that the growth of the out-layer region began at 30 s, as shown by the yellow arrow, "B", in Figure 3-5.

On the structure origin of the ring-banded spherulites morphology of polymer, many evidence shows that it is related to the helicoidal twisted lamellae along the radial growth direction of the spherulites.[7,62-70] Helicoidal twist has mainly explained by the unbalanced surface stress that results from differential congestion of fold surfaces[31] or isochiral giant screw dislocations.[71]

Untill now, AFM,[7,8,11,17,19,30,72] tilt POM,[7,8,17,72] and microbeam X-ray[11,65,66-70] measurements have generally been used to investigate the hierarchical organization of ring-banded spherulites. By tilt POM and AFM experiments, it has been reported that the lamellar twisting also occurs in banded PBA spherulites.[17,19] Our results show the periodic change of the molecular chain orientations, which corresponding well to the previous studies, this part will be discussed later in the following section.

Figure 3-7(a) and (b) show optical images of PBA28–35 and the corresponding Raman images generated from the position of the C-peak, respectively. Like with the image in Figure 3-4(b), the author used the C-peak position to determine the relative distributions of the two types of crystal structures. The ringless patterns can be seen for PBA28 and PBA35 in Figure 3-7(a), while the ring-banded patterns were observed for PBA30–33. As mentioned above, the Raman image based on the C-peak position of PBA32 shows mainly three different regions in the spherulite: the center, the region between the center and out-layer of the spherulite, and the out-layer region. Therefore, in Figure 3-7(b), the author chose three small square regions as regions 1–3 (designated hereafter as R1–R3), which are located in the center region, the region between the center and out-layer of the spherulite, and the out-layer region, respectively. The average peak position was calculated in each region, and the results are plotted in Figure 3-7(c). Since PBA28

and PBA35 contain pure β- and α-form crystals, respectively (Figure 3-2), only their center region and another region were chosen. The C-peak position in the 1247–1244 cm^{-1} region was determined from the relative contents of the β and α forms; hence, Figure 3-7(c) was divided into three regions based on the peak position (Raman shift): the β-form region (1244 ±0.3 cm^{-1}, yellow), (α+β)-forms region (1244–1247 cm^{-1}, green), and α-form region (1247 ±0.3 cm^{-1}, blue). The peaks position for both R1 and R2 of PBA28 and PBA35 undoubtedly appear in the β- and α-form regions, respectively, as shown in Figure 3-7(c). What is more interesting is that R1 and R2 for PBA31–33 appear in the (α+β) region, which indicates conucleation and cogrowth of the α and β forms in PBA31–33. For PBA30, only R3 appears in the (α+β) region, while R1 and R2 appear in the β region. This is somewhat strange, although there is no doubt that the ring-banded region contains both the α and β forms for PBA30, which is in agreement with the results for PBA31–33.

The C-peak positions of R3 for PBA31–33 in the α-form region are almost unchanged, while the positions of R1 and R2 are not constant; they increase with increasing T_c, owing to the fact that PBA prefers to crystallize into the α form at higher T_c. Moreover, it is of note that the peak positions of R1 are always higher than those of R2, suggesting that the α form is more abundant in the center region than in the ring-banded region. Two factors for this phenomenon should be considered. One is the relative primary nucleation rate, and the other is the radial growth rate. The primary nucleation rate of the α form is faster than that of the β form, while the growth rate of the α form is slower than that of the β-form.[17] Therefore, in the center region, the α-form crystals, which form first, may restrict the formation of β-form crystals, while the α and β forms grow together during the growth process.

The average band spacing (S) changes of PBA31–33 were also investigated, and the results are shown in Figure 3-7(d) (the band spacing for PBA31, PBA32, and PBA33 are shown in Figure A2-4 in the Appendix 2). As T_c increased, the band spacing decreased from approximately 4.6 to 3 μm. If the lamellar twist resulting from surface stresses, the deformation energy for lamellar twisting, U_{twist}, is related to the band spacing, as shown in eq. 3-1:[73]

$$U_{twist} = \frac{\pi^2 G W l^2}{6S} \qquad (3\text{-}1)$$

where G is the rigidity modulus, W is the crystal width, and l is the lamellar thickness. Assuming that G of the lamellae is constant, increases in l and W and a decrease in S with T_c will lead to an

increase in U_{twist}. Moreover, in this study, since the relative contents of α- and β-form crystals in the ring-banded region also change with T_c, it is reasonable to speculate that changes in their contents may also affect U_{twist}.

As for the formation of pure α-form crystals in the out-layer region (R3), based on the growth process of PBA32 (Figure 3-5), it seems that the pattern in the out-layer region is not smooth, but composed of many small fan-shaped parts. This may be due to the nucleation and growth of many small spherulites along the surface of the ring-banded spherulites at the same time. That is to say, the out-layer ringless region is not belong to the ring-banded PBA spherulite. Liu et al.[17] had reported a similar phenomenon, which was attributed to the PBA molecular chains with low MW. They found that the low-MW molecular chains tend to form α-form crystals, while high-MW chains tend to form β-form crystals under the same supercooling. During crystallization, the β-form crystals have a faster crystallization rate, which means that the molecular chains with high-MW will be used up earlier than the low-MW chains. Thus, in the present study, the out-layer region consists only of α-form crystals, which are formed by the leftover low-MW chains. This can also be proven by the fact that the out-layer region becomes larger from PBA31 to PBA33, as shown in Figures 3-1(f–h), which suggests that more molecular chains are crystallized into α-form crystals at higher crystallization temperatures. The detailed distribution of different MW chains within the PBA spherulite is currently under investigation.

Molecular Chains Orientation within the Ring-Banded PBA Spherulites.

Since the molecular chains in the amorphous region are almost disordered, the following discussion are mainly about the molecular chains orientation in the crystal region. Note that the POM image of PBA32 (Figure 3-1(g)) shows a very orderly ring-banded pattern, which means the refractive index of the lamellar structure along the film thickness should be kept constant. Therefore, the molecular chains within the lamellar structure should have a similar orientation across the film thickness.

As shown in the Figure 3-4(b), the Raman images which generated by the C-peak area present ring-banded bow-tie patterns, and the direction of the bow-tie also shows laser polarization dependence. While the Raman images for the C=O stretching band area show just bow-tie pattern without ring-banded (Figure A2-5). Moreover, the directions of the bow-tie patterns for the C=O stretching peak area are different with that of the C-peak area as well. For example, the bow-tie is

in vertical direction for the C-peak, while in horizontal direction for the *ν*(C=O) peak when the incident laser polarization angle is 0 °, and vice versa. These indicated that the molecular chains within the spherulites oriented not only about the radial direction of the spherulite, but also about the substrate plane. It is well known that the twisting lamellae will lead to the different orientations of the crystal axes with respect to the substrate (sample film) surface.[70,72,74-77]

Thus, our Raman imaging results were in good agreement with previous studies; both suggested that the molecular chains have periodical orientations with respect to the substrate plane. Moreover, if the lamellar twisting model is also considered, then it is reasonable to speculate that the molecular chains are perpendicular to the substrate plane in the flat-on domains and parallel to the substrate plane in the edge-on domains within the ring-banded PBA spherulites, as shown in Figure 3-8. Since the helicoidal twisted lamellae have similar orientation across the film thickness as mentioned above, in general, it can be presented simplified as a screw.[2,7,8,31,47,69] For PBA, there is no preferred twist handedness; since PBA is an achiral polymer, both left- and right-handed twists can exist in each of the ring-banded spherulite.[17] The similar phenomenon has also been found in the ring-banded spherulite of poly(ε-caprolactone) (PCL).[78]

Conclusion

The distribution of polymorphic crystals and the molecular chains orientation in PBA spherulites was investigated using Raman spectroscopy and Raman imaging for the first time. Special attention were paid to the so-called "ring-banded" PBA spherulites with out-layer ringless region that were isothermally crystallized at T_c = 31–33 ℃; within each spherulite, two crystal forms, the α and β forms, coexisted (Figure 3-1).

The characteristic Raman peaks for both α- and β-form crystal structures and the amorphous structure of PBA were observed (Figure 3-2). These peaks were employed to investigate the polymorphic crystal distribution through Raman imaging. It was found that the center and ring-banded regions contained both α- and β-form crystals, while the out-layer region contained only α-form crystals (Figures 3-4 and 3-7). The formation of the α-form crystals in the out-layer ringless region is due to the crystallization of the low-molecular-weight PBA chains. The results of Raman imaging and in-situ time-resolved POM indicated that the α- and β-form crystals can nucleate and grow in the same temperature range (31–33 ℃), and the relative content of these two crystal forms within the ring-banded spherulites show temperature dependence. The higher crystallization temperature, the higher content of the α-form crystals.

The molecular chains within the PBA spherulites are oriented almost perpendicular to the spherulite growth direction. However, the ring-banded domains have different orientations about the substrate plane; the molecular chains orient perpendicular to the substrate plane in the flat-on domains and parallel to the substrate plane in the edge-on domains (Figure 3-8).

The present study has suggested that Raman imaging is a very powerful technique in polymer crystal structure research. Because of the high spatial resolution of Raman imaging, information about inhomogeneous structures even in a small crystal domain can be provided, and polarized measurements can be used to investigate the orientations of the molecular chains within a crystal structure as well.

References

1. Shtukenberg, A. G.; Punin, Y. O.; Gunn, E.; Kahr, B. Spherulites. *Chem. Rev.* **2012**, 112, 1805–1838.
2. Crist, B.; Schultz, J. M. Polymer spherulites: A critical review. *Prog. Polym. Sci.* **2016**, *56*, 1–63.
3. Geil, P. H. *Polymer Single Crystals*; Wiley-Interscience: New York, 1963.
4. Gránásy, L.; Pusztai, T.; Tegze, G.; Warren, J. A.; Douglas, J. F. Growth and form of spherulites. *Phys. Rev. E* **2005**, *72*, 011605.
5. Hosier, I. L.; Bassett, D. C.; Vaughan, A. S. Spherulitic Growth and Cellulation in Dilute Blends of Monodisperse Long n-Alkanes. *Macromolecules* **2000**, *33*, 8781–8790.
6. Hosier, I. L.; Bassett, D. C. A study of the morphologies and growth kinetics of three monodisperse n-alkanes: C 122 H 246, C 162 H 326 and C 246 H 494. *Polymer* **2000**, *41*, 8801–8812.
7. Ye, H.; Xu, J.; Guo, B.; Iwata, T. Left- or Right-Handed Lamellar Twists in Poly[(R)-3-hydroxyvalerate] Banded Spherulite: Dependence on Growth Axis. *Macromolecules* **2009**, *42*, 694–701.
8. Ye, H.; Wang, J.; Tang, S.; Xu, J.; Feng, X.; Guo, B.; Xie, X.; Zhou, J.; Li, L.; Wu, Q. Surface Stress Effects on the Bending Direction and Twisting Chirality of Lamellar Crystals of Chiral Polymer. *Macromolecules* **2010**, *43*, 5762–5770.
9. Xu, J.; Guo, B.; Zhou, J.; Li, L.; Wu, J.; Kowalczuk, M. Observation of banded spherulites in pure poly(L-lactide) and its miscible blends with amorphous polymers. *Polymer* **2005**, *46*, 9176–9185.
10. Cao, Q.; Qiao, X.; Wang, H.; Liu, J. Structures and growth mechanisms of poly-(3-hydroxybutyrate) (PHB) crystallized from solution and thin melt film. *Sci. China Ser. B: Chem.* **2008**, *51*, 853–858.
11. Wang, Z.; Alfonso, G. C.; Hu, Z.; Zhang, J.; He, T. Rhythmic Growth-Induced Ring-Banded Spherulites with Radial Periodic Variation of Thicknesses Grown from Poly(ε-caprolactone) Solution with Constant Concentration. *Macromolecules* **2008**, *41*, 7584–7595.
12. Hoffman, J. D.; Lauritzen, J. I.; Passaglia, E.; Ross, G. S.; Frolen, L. J.; Weeks, J. J. Kinetics

of polymer crystallization from solution and the melt. *Kolloid Z. Z. Polym.* **1969**, *231*, 564–592.

13. Zhu, B.; He, Y.; Asakawa, N.; Yoshie, N.; Nishida, H.; Inoue, Y. Polymorphic Crystallization and Melting-Recrystallization Behavior of Poly(3-hydroxypropionate). *Macromolecules* **2005**, *38*, 6455–6465.
14. Stein, R. S.; Misra, A. Morphological studies on polybutylene terephthalate. *J. Polym. Sci., Polym. Phys.* **1980**, *18*, 327–342.
15. Roche, E. J.; Stein, R. S.; Thomas, E. L. Electron microscopy study of the structure of normal and abnormal poly(butylene terephthalate) spherulites. *J. Polym. Sci., Polym. Phys.* **1980**, *18*, 1145–1158.
16. Fu, Q.; Heck, B.; Strobl, G.; Thomann, Y. A Temperature- and Molar Mass-Dependent Change in the Crystallization Mechanism of Poly(1-butene): Transition from Chain-Folded to Chain-Extended Crystallization? *Macromolecules* **2001**, *34*, 2502–2511.
17. Liu, J.; Ye, H.; Xu, J.; Guo, B. Formation of ring-banded spherulites of α and β modifications in Poly(butylene adipate). *Polymer* **2011**, *52*, 4619–4630.
18. Woo, E. M.; Yen, K. C.; Wu, M. C. Analysis of multiple melting behavior of spherulites comprising ring-band shell/ringless core in polymorphic poly(butylene adipate). *J. Polym. Sci. B Polym. Phys.* **2008**, *46*, 892–899.
19. Zhao, L.; Wang, X.; Li, L.; Gan, Z. Structural analysis of poly(butylene adipate) banded spherulites from their biodegradation behavior. *Polymer* **2007**, *48*, 6152–6161.
20. Song, Y.; Ye, H.; Xu, J.; Hou, K.; Zhou, Q.; Lu, G. Stretch-induced bidirectional polymorphic transformation of crystals in poly(butylene adipate). *Polymer* **2014**, *55*, 3054–3061.
21. Yang, J.; Chen, Y.; Qin, S.; Liu, J.; Bi, C.; Liang, R.; Dong, T.; Feng, X. Effects of Cyanuric Acid on Crystallization Behavior, Polymorphism, and Phase Transition of Poly(butylene adipate). *Ind. Eng. Chem. Res.* **2015**, *54*, 8048–8055.
22. Pan, P.; Inoue, Y. Polymorphism and isomorphism in biodegradable polyesters. *Prog. Polym. Sci.* **2009**, *34*, 605–640.
23. Minke, R.; Blackwell, J. Polymorphic structures of poly(tetramethylene adipate). *J. Macromol. Sci. B Phys.* **1979**, *16*, 407–417.
24. Gan, Z.; Abe, H. Temperature-Induced Polymorphic Crystals of Poly(butylene adipate).

Macromol. Chem. Phys. **2002**, *203*, 2369–2374.

25. Pouget, E.; Almontassir, A.; Casas, M. T.; Puiggalí, J. On the Crystalline Structures of Poly(tetramethylene adipate). *Macromolecules* **2003**, *36*, 698–705.
26. Gan, Z.; Kuwabara, K.; Abe, H.; Iwata, T.; Doi, Y. Metastability and Transformation of Polymorphic Crystals in Biodegradable Poly(butylene adipate). *Biomacromolecules* **2004**, *5*, 371–378.
27. Noguchi, K.; Kondo, H.; Ichikawa, Y.; Okuyama, K.; Washiyama, J. Molecular and crystal structure of poly(tetramethylene adipate) α form based on synchrotron X-ray fiber diffraction. *Polymer* **2005**, *46*, 10823–10830.
28. Wang, L.; Lugito, G.; Woo, E. M.; Wang, Y. Phase behavior, polymorphism and spherulite morphology in Poly(1,4-butylene adipate) interacting with two structurally similar acrylic polymers. *Polymer* **2012**, *53*, 3815–3826.
29. Gan, Z.; Kuwabara, K.; Abe, H.; Iwata, T.; Doi, Y. The role of polymorphic crystal structure and morphology in enzymatic degradation of melt-crystallized poly(butylene adipate) films. *Polym. Degrad. Stab.* **2005**, *87*, 191–199.
30. Frömsdorf, A.; Woo, E. M.; Lee, L.; Chen, Y.; Förster, S. Atomic Force Microscopy Characterization and Interpretation of Thin-Film Poly(butylene adipate) Spherulites with Ring Bands. *Macromol. Rapid Commun.* **2008**, *29*, 1322–1328.
31. Lotz, B.; Cheng, S. Z. D. A critical assessment of unbalanced surface stresses as the mechanical origin of twisting and scrolling of polymer crystals. *Polymer* **2005**, *46*, 577–610.
32. Minke, R.; Blackwell, J. Single crystals of poly(tetramethylene adipate). *J. Macromol. Sci. Part B: Phys.* **1980**, *18*, 233–255.
33. Yan, C.; Zhang, Y.; Hu, Y.; Ozaki, Y.; Shen, D.; Gan, Z.; Yan, S.; Takahashi, I. Melt Crystallization and Crystal Transition of Poly(butylene adipate) Revealed by Infrared Spectroscopy. *J. Phys. Chem. B* **2008**, *112*, 3311–3314.
34. Yang, J.; Li, Z.; Pan, P.; Zhu, B.; Dong, T.; Inoue, Y. Temperature-dependent polymorphic crystalline structure and melting behavior of poly(butylene adipate) investigated by time-resolved FTIR spectroscopy. *J. Polym. Sci. B Polym. Phys.* **2009**, *47*, 1997–2007.
35. Sun, X.; Pi, F.; Zhang, J.; Takahashi, I.; Wang, F.; Yan, S.; Ozaki, Y. Study on the Phase Transition Behavior of Poly(butylene adipate) in its Blends with Poly(vinyl phenol). *J. Phys.*

Chem. B **2011**, *115*, 1950–1957.

36. Sun, X.; Liu, J.; Takahashi, I.; Yan, S. Melting and β to α transition behavior of β-PBA and the β-PBA/PVPh blend investigated by synchrotron SAXS and WAXD. *RSC Adv.* **2014**, *4*, 39101–39109.
37. Vogel, C.; Wessel, E.; Siesler, H. W. FT-IR Spectroscopic Imaging of Anisotropic Poly(3-hydroxybutyrate)/Poly(lactic acid) Blends with Polarized Radiation. *Macromolecules* **2008**, *41*, 2975–2977.
38. Merten, C.; Kowalik, T.; Achoff, S. J.; Hartwig, A. FTIR Imaging of Poly(3-hydroxybutyrate) and Isotactic Poly(propylene oxide) Spherulites. *Macromol. Chem. Phys.* **2010**, *211*, 1627–1631.
39. Cong, Y.; Hong, Z.; Qi, Z.; Zhou, W.; Li, H.; Liu, H.; Chen, W.; Wang, X.; Li, L. Conformational Ordering in Growing Spherulites of Isotactic Polypropylene. *Macromolecules* **2010**, *43*, 9859–9864.
40. Wang, W.; Jin, Y.; Yang, X.; Su, Z. Chain orientation and distribution in ring-banded spherulites formed in poly(ester urethane) multiblock copolymer. *J. Polym. Sci, Part B: Polym. Phys.* **2010**, *48*, 541–547.
41. Jin, Y.; Wang, W.; Su, Z. Infrared Imaging of Ring-Banded Spherulites Formed in Poly (L-lactide)–Poly(ethylene glycol) Diblock Copolymer: Segment Distribution and Orientation. *Appl. Spectrosc.* **2011**, *65*, 454–458.
42. Hikima, Y.; Morikawa, J.; Hashimoto, T. FT-IR Image Processing Algorithms for In-Plane Orientation Function and Azimuth Angle of Uniaxially Drawn Polyethylene Composite Film. *Macromolecules* **2011**, *44*, 3950–3957.
43. Hong, Z.; Cong, Y.; Qi, Z.; Li, H.; Zhou, W.; Chen, W.; Wang, X.; Zhou, Y.; Li, L. Studying deformation behavior of a single spherulite with in-situ infrared microspectroscopic imaging. *Polymer* **2012**, *53*, 640–647.
44. Hikima, Y.; Morikawa, J.; Hashimoto, T. Imaging of Two-Dimensional Distribution of Molecular Orientation in Poly(ethylene oxide) Spherulite Using IR Spectrum and Birefringence. *Macromolecules* **2012**, *45*, 8356–8362.
45. Chen, W.; Li, X.; Li, H.; Su, F.; Zhou, W.; Li, L. Deformation-induced crystal-crystal transition of polybutene-1: an in situ FTIR imaging study. *J. Mater. Sci.* **2013**, *48*, 4925–4933.

46. Li, H.; Zhou, W.; Ji, Y.; Hong, Z.; Miao, B.; Li, X.; Zhang, J.; Qi, Z.; Wang, X.; Li, L.; Li, Z. Spatial distribution of crystal orientation in neck propagation: An *in-situ* microscopic infrared imaging study on polyethylene. *Polymer* **2013**, *54*, 972–979.
47. Hikima, Y.; Morikawa, J.; Hashimoto, T. Wavenumber Dependence of FT-IR Image of Molecular Orientation in Banded Spherulites of Poly(3-hydroxybutyrate) and Poly(L-lacticacid). *Macromolecules* **2013**, *46*, 1582–1590.
48. Hu, J.; Tashiro, K. Time-Resolved Imaging of the Phase Transition in the Melt-Grown Spherulites of Isotactic Polybutene-1 as Detected by the Two-Dimensional Polarized IR Imaging Technique. *J. Phys. Chem. B* **2016**, *120*, 4689–4698.
49. Sasic, S., Ozaki, Y., Eds.; *Raman, Infrared, and Near-Infrared Chemical Imaging*; John Wiley & Sons, Inc.: Hoboken, NJ, 2010.
50. Salzer, R., Siesler, H. W., Eds.; *Infrared and Raman Spectroscopic Imaging*, 2nd ed.; Wiley-VCH: Weinheim, 2009.
51. Lan, Q.; Li, Y. Mesophase-Mediated Crystallization of Poly(L-lactide): Deterministic Pathways to Nanostructured Morphology and Superstructure Control. *Macromolecules* **2016**, *49*, 7387–7399.
52. van Apeldoorn, A. A.; Van Manen, H.; Bezemer, J. M.; de Bruijn, J. D.; van Blitterswijk, C. A.; Otto, C. Raman Imaging of PLGA Microsphere Degradation Inside Macrophages. *J. Am. Chem. Soc.* **2004**, *126*, 13226–13227.
53. Schaeberle, M. D.; Karakatsanis, C. G.; Lau, C. J.; Treado, P. J. Raman chemical imaging: noninvasive visualization of polymer blend architecture. *Anal. Chem.* **1995**, *67*, 4316–4321.
54. Chernenko, T.; Matthäus, C.; Milane, L.; Quintero, L.; Amiji, M.; Diem, M. Label-Free Raman Spectral Imaging of Intracellular Delivery and Degradation of Polymeric Nanoparticle Systems. *ACS Nano* **2009**, *3*, 3552–3559.
55. Unger, M.; Sato, H.; Ozaki, Y.; Fischer, D.; Siesler, H. W. Temperature-Dependent Fourier Transform Infrared Spectroscopy and Raman Mapping Spectroscopy of Phase-Separation In a Poly(3-hydroxybutyrate)-poly(L-Lactic Acid) Blend. *Appl. Spectrosc.* **2013**, *67*, 141–148.
56. Martin, J.; Bourson, P.; Dahoun, A.; Hiver, J. M. The β-Spherulite Morphology of Isotactic Polypropylene Investigated by Raman Spectroscopy. *Appl. Spectrosc.* **2009**, *63*, 1377-1381.
57. Wu, M. C.; Woo, E. M. Effects of α- form or β-form nuclei on polymorphic crystalline

morphology of poly(butylene adipate). *Polym. Int.* **2005**, *54*, 1681–1688.

58. Gautam, R.; Samuel, A.; Sil, S.; Chaturvedi, D.; Dutta, A.; Ariese, F.; Umapathy, S. Raman and mid-infrared spectroscopic imaging: applications and advancements. *Curr. Sci.* **2015**, *108*, 341–356.
59. Colthup, N. B.; Daly, L. H.; Wiberley, S. E. *Introduction to Infrared and Raman Spectroscopy*, 3rd ed.; Academic Press: London, 1990.
60. Fernandez, M. R.; Merino, J. C.; Gobernado-Mitre, M. I.; Pastor, J. M. Molecular and Lamellar Orientation of α- and β-Transcrystalline Layers in Polypropylene Composites by Polarized Confocal Micro-Raman Spectroscopy: Raman Imaging by Static Point Illumination. *Appl. Spectrosc.* **2000**, *54*, 1105–1113.
61. Song, K.; Rabolt, J. F. Polarized Raman Measurements of Uniaxially Oriented Poly(ε-caprolactam). *Macromolecules* **2001**, *34*, 1650–1654.
62. Keith, H. D. Optical Behavior and Polymorphism in Poly(ethylene sebacate). 1. Morphology and Optical Properties. *Macromolecules* **1982**, *15*, 114–122.
63. Gazzano, M.; Focarete, M. L.; Riekel, C.; Scandola, M. Structural Study of Poly($_L$-lactic acid) Spherulites. *Biomacromolecules* **2004**, *5*, 553–558.
64. Point, J. J. Multiple order light scattering by ringed spherulites. *Polymer* **2006**, *47*, 3186–3196.
65. Tanaka, T.; Fujita, M.; Takeuchi, A.; Suzuki, Y.; Uesugi, K.; Doi, Y.; Iwata, T. Structure investigation of narrow banded spherulites in polyhydroxyalkanoates by microbeam X-ray diffraction with synchrotron radiation. *Polymer* **2005**, *46*, 5673–5679.
66. Kikuzuki, T.; Shinohara, Y.; Nozue, Y.; Ito, K.; Amemiya, Y. Determination of lamellar twisting manner in a banded spherulite with scanning microbeam X-ray scattering. *Polymer* **2010**, *51*, 1632–1638.
67. Rosenthal, M.; Bar, G.; Burghammer, M.; Ivanov, D. A. On the Nature of Chirality Imparted to Achiral Polymers by the Crystallization Process. *Angew. Chem., Int. Ed.* **2011**, *50*, 8881–8885.
68. Rosenthal, M.; Portale, G.; Burghammer, M.; Bar, G.; Samulski, E. T.; Ivanov, D. A. Exploring the Origin of Crystalline Lamella Twist in Semi-Rigid Chain Polymers: the Model of Keith and Padden revisited. *Macromolecules* **2012**, *45*, 7454–7460.
69. Rosenthal, M.; Burghammer, M.; Bar, G.; Samulski, E. T.; Ivanov, D. A. Switching Chirality

of Hybrid Left–Right Crystalline Helicoids Built of Achiral Polymer Chains: When Right to Left Becomes Left to Right. *Macromolecules* **2014**, *47*, 8295–8304.

70. Hsieh, Y.; Ishige, R.; Higaki, Y.; Woo, E. M.; Takahara, A. Microscopy and microbeam X-ray analyses in poly(3-hydroxybutyrate-co-3-hydroxyvalerate) with amorphous poly(vinyl acetate). *Polymer* **2014**, *55*, 6906–6914.
71. Toda, A.; Okamura, M.; Taguchi, K.; Hikosaka, M.; Kajioka, H. Branching and Higher Order Structure in Banded Polyethylene Spherulites. *Macromolecules* **2008**, *41*, 2484–2493.
72. Meyer, A.; Yen, K. C.; Li, S.; Förster, S.; Woo, E. M. Atomic-Force and Optical Microscopy Investigations on Thin-Film Morphology of Spherulites in Melt-Crystallized Poly(ethylene adipate). *Ind. Eng. Chem. Res.* **2010**, *49*, 12084–12092.
73. Keith, H. D.; Padden, F. J. Twisting orientation and the role of transient states in polymer crystallization. *Polymer* **1984**, *25*, 28–42.
74. Sun, X.; Chen, Z.; Wang, F.; Yan, S.; Takahashi, I. Influence of Poly(vinylphenol) Sublayer on the Crystallization Behavior of Poly(3-hydroxybutyrate) Thin Films. *Macromolecules* **2013**, 46, 1573-1581.
75. Sun, X.; Ren, Z.; Liu, J.; Takahashi, I.; Yan, S. Structure Evolution of Poly(3-hexylthiophene) on Si Wafer and Poly(vinylphenol) Sublayer. *Langmuir* **2014**, *30*, 7585–7592.
76. Li, H.; Yan, S. Surface-Induced Polymer Crystallization and the Resultant Structures and Morphologies. *Macromolecules* **2011**, *44*, 417–428.
77. Marubayashi, H.; Nobuoka, T.; Iwamoto, S.; Takemura, A.; Iwata, T. Atomic Force Microscopy Observation of Polylactide Stereocomplex Edge-On Crystals in Thin Films: Effects of Molecular Weight on Lamellar Curvature. *ACS Macro Lett.* **2013**, *2*, 355–360.
78. Nozue, Y.; Hirano, S.; Kurita, R.; Kawasaki, N.; Ueno, S.; Iida, A.; Nishi, T.; Amemiya, Y. Co-existing handednesses of lamella twisting in one spherulite observed with scanning microbeam wide-angle X-ray scattering. *Polymer* **2004**, *45*, 8299–8302.

Table 3-1. Assignments for Characteristic Raman Peaks of PBA.

Raman shift (cm^{-1})	assignments
1185	α-form crystal
1245	β-form crystal, amorphous
1247	α-form crystal
1268	β-form crystal

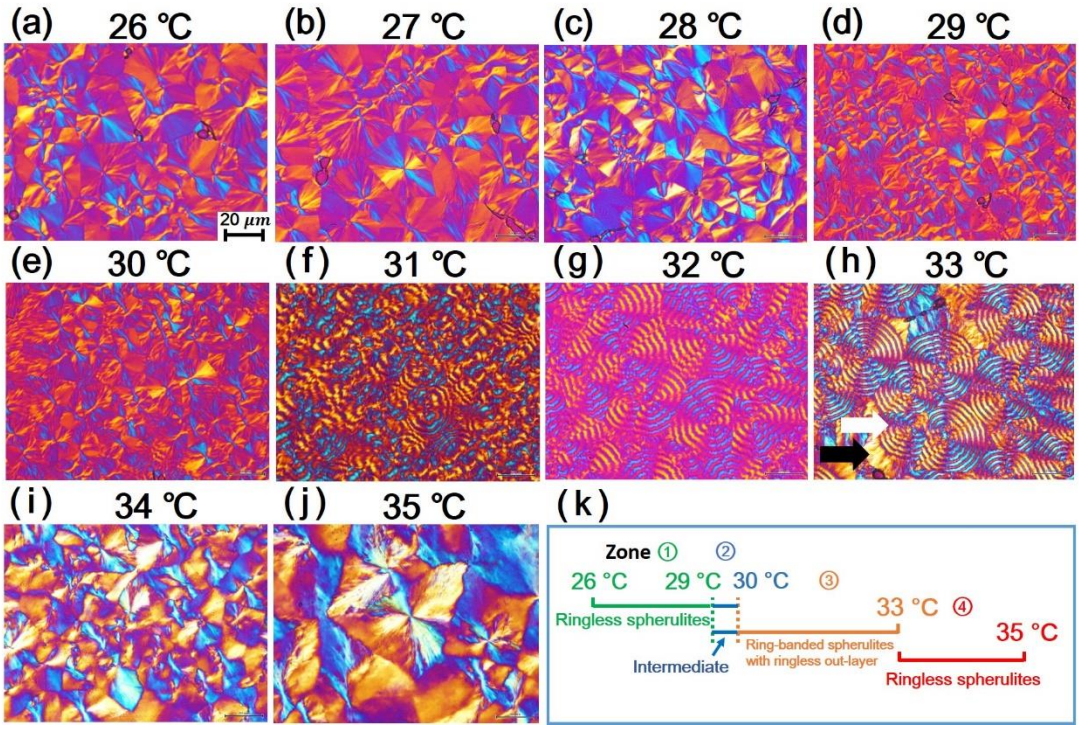

Figure 3-1. POM images of PBA spherulites that underwent isothermal melt crystallization at different temperatures between 26 and 35 ℃ (a–j) (the scale bar is 20 μm for all micrographs) and the morphology diagrams of the PBA spherulites crystallized at different temperatures (k).

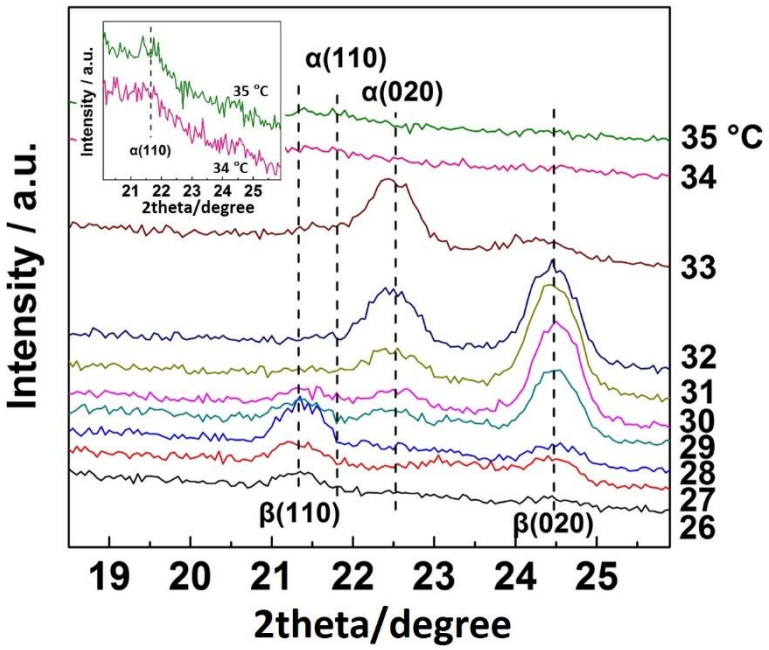

Figure 3-2. WAXD profiles of PBA films that underwent isothermal melt crystallization at different temperatures between 26 and 35 ℃.

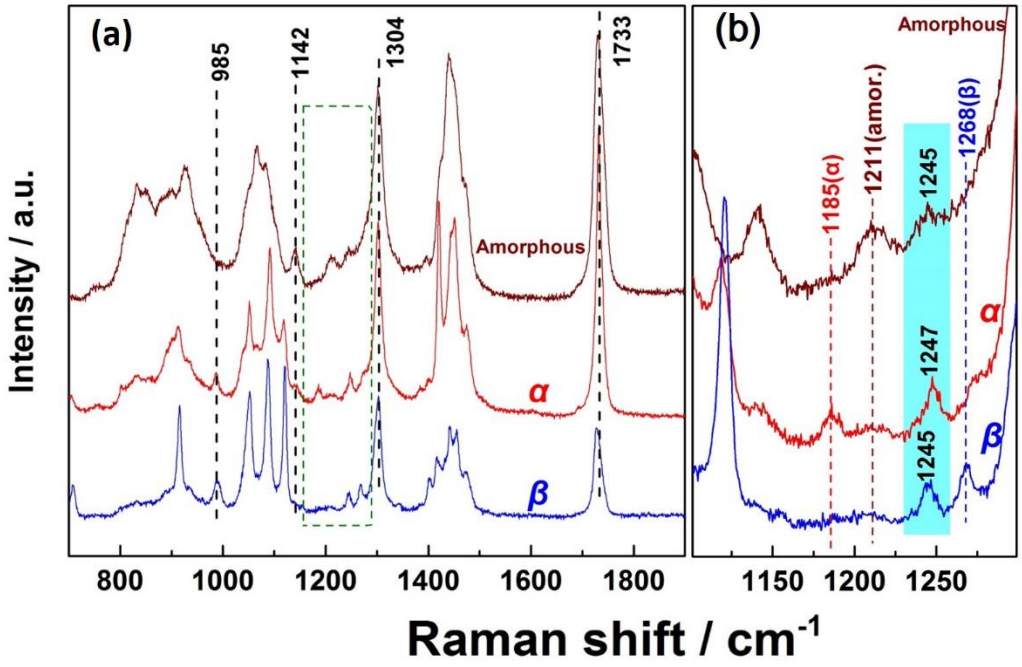

Figure 3-3. Raman spectra of PBA film with α- and β-form crystals, measured at room temperature, and with an amorphous structure, measured at 70 ℃.

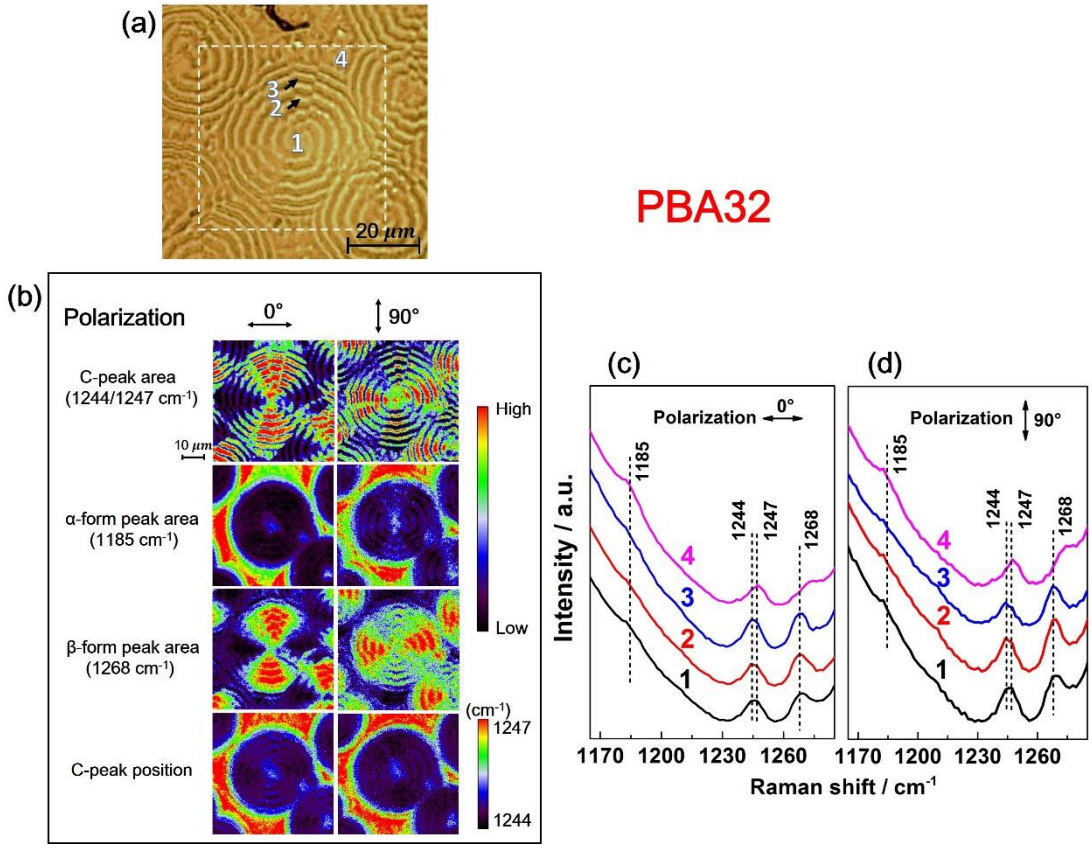

Figure 3-4. (a) Optical micrograph of PBA32. (b) Raman imaging of the same area as (a) with polarization parallel (0 °) and perpendicular (90 °) to the horizontal direction; imaging of the area was achieved by integrating the C-peak, α-form peak, and β-form peak regions. The image based on the C-peak position was obtained by point-by-point peak fitting of the C-peak. (c, d) Raman spectra with parallel (0 °) and perpendicular (90 °) polarization of the center (#1), flat-on (#2), edge-on (#3), and out-layer ringless (#4) regions in the PBA32 shown in (a).

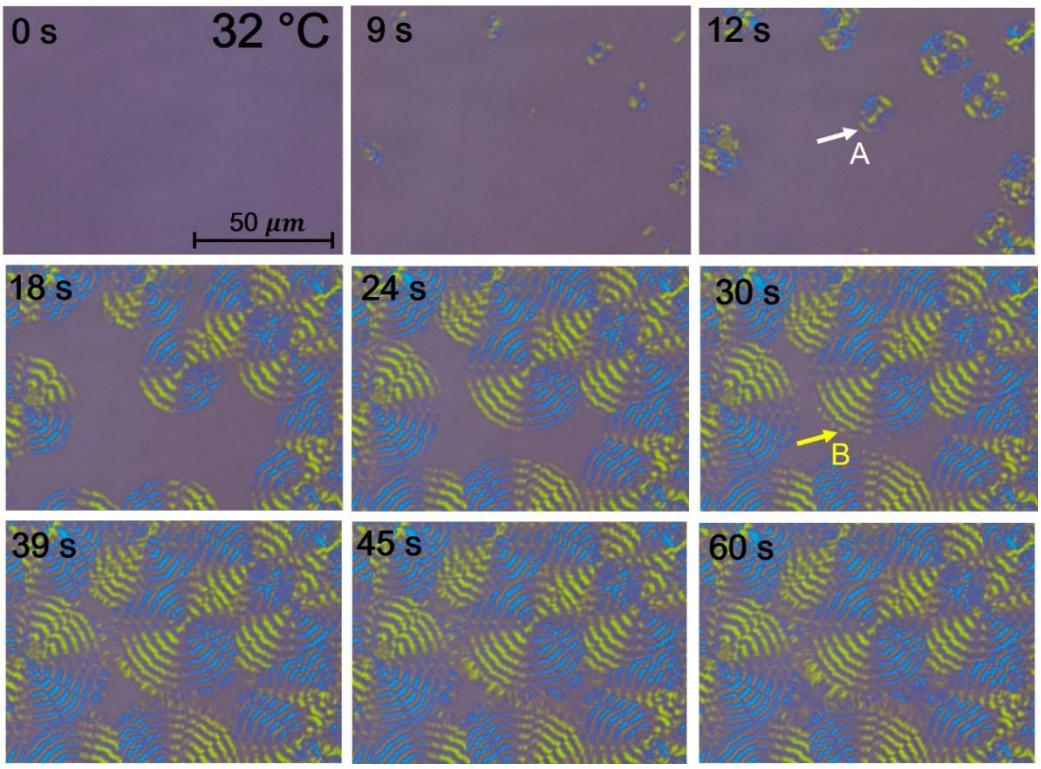

Figure 3-5. Optical micrographs of in situ time-resolved crystallization of PBA32 (the scale bar is 50 μm for all micrographs).

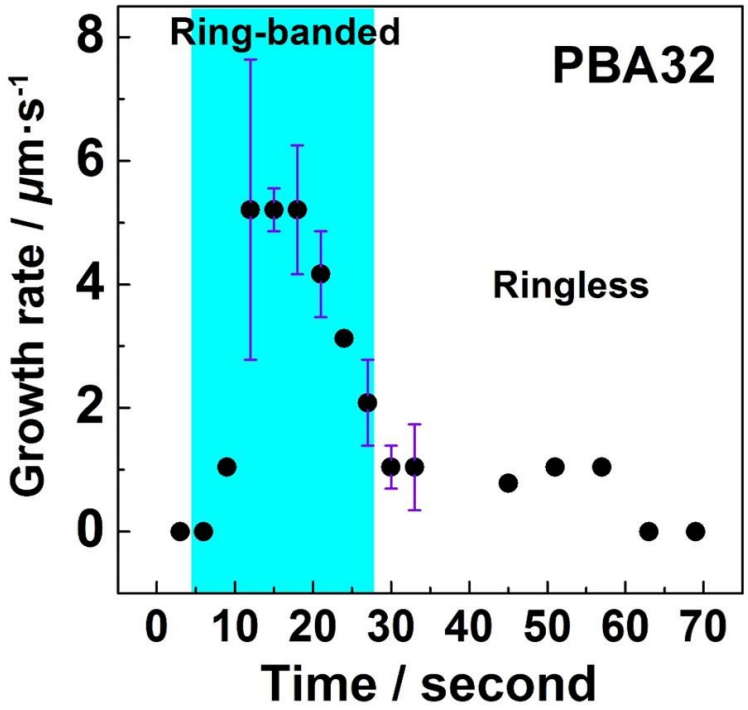

Figure 3-6. Time-dependent growth rate in crystallization of PBA32 corresponding to Figure 5.

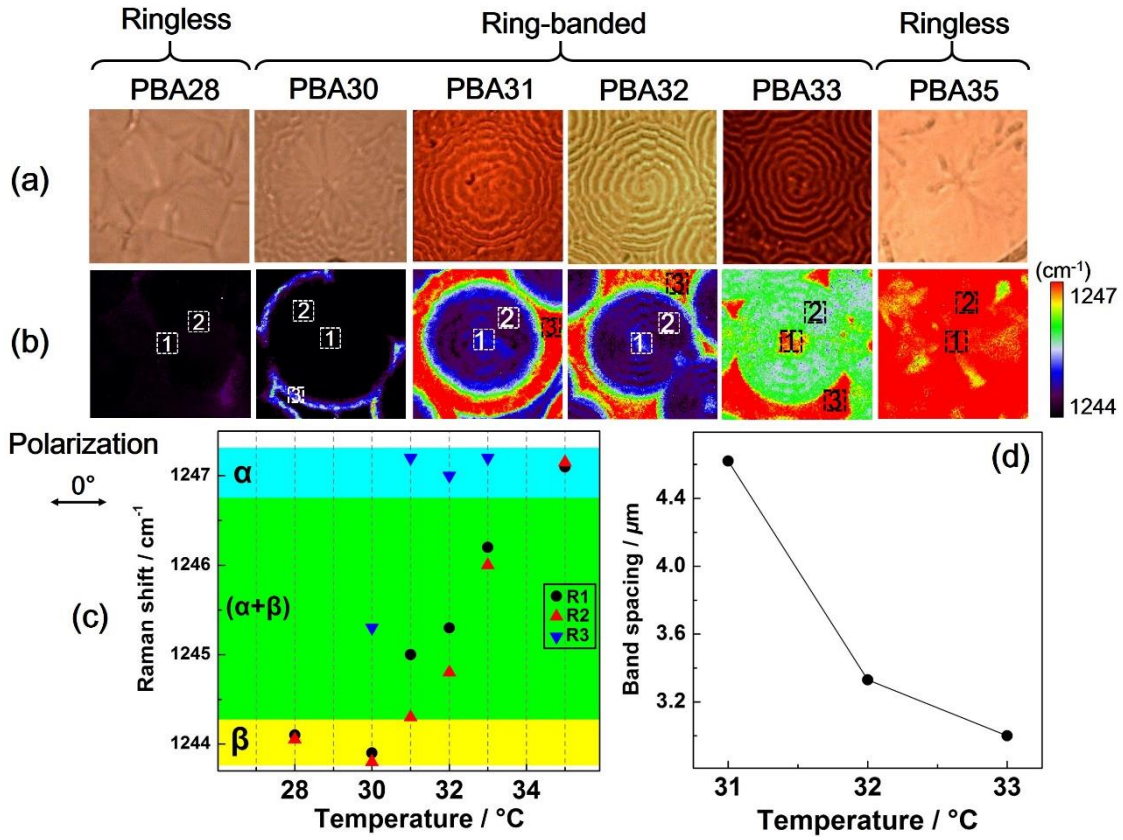

Figure 3-7. (a) Optical micrographs of PBA28, PBA30–33, and PBA35. (b) Raman imaging of C-peak position for the same area in (a). (c) Averaged C-peak position in the center region (R1), the region between the center and out-layer of the spherulite (R2), and the out-layer region (R3) for PBA30–33, and in the center region (R1) and another region (R2) for PBA28 and PBA35. (d) Average band spacing change for PBA31–33.

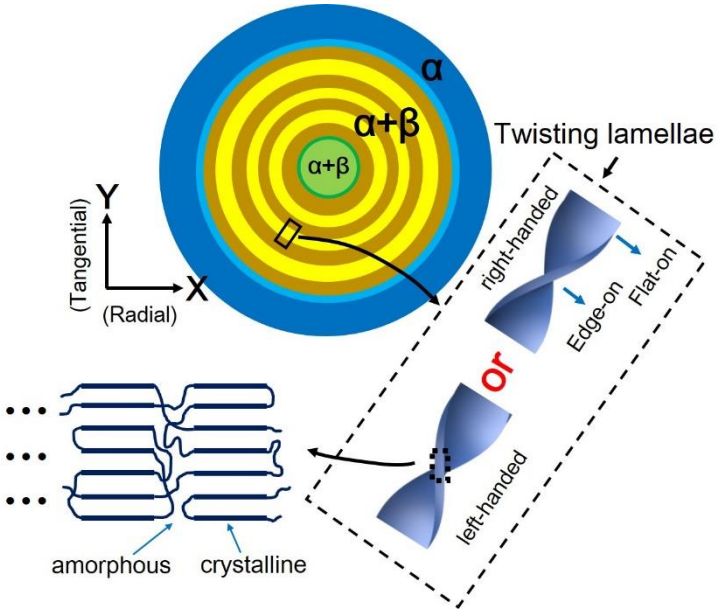

Figure 3-8. Schematic diagram of hierarchy structure consisting of twisting lamellae in the ring-banded region and polymorphic crystal distribution within a ring-banded PBA spherulite with a ringless out-layer.

Appendix 2

A2-1. Chemical Structure of Poly(butylene adipate)

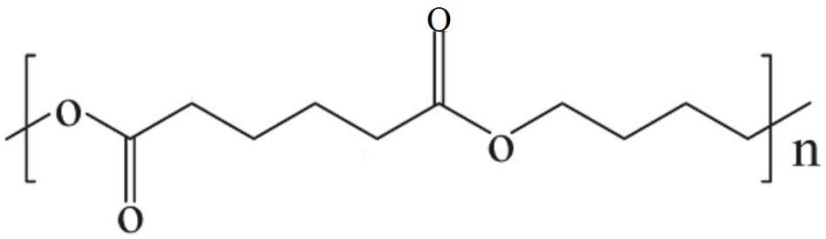

Figure A2-1. Chemical structure of poly(butylene adipate) (PBA).

A2-2. Scattering Geometries for Polarized Raman Measurements

Raman imaging measurements in present study was under backscattering mode. In Porto notation, Z and $\bar{Z}$ refers to the direction of incident and scattering light, respectively. The $\bar{Z}$ implies that the scattered light is rotated 180 ° with respect to Z. The X (or Y) in the parentheses describes the polarization of the incident light and the XY means no analyzer in the scattered beam path.[1]

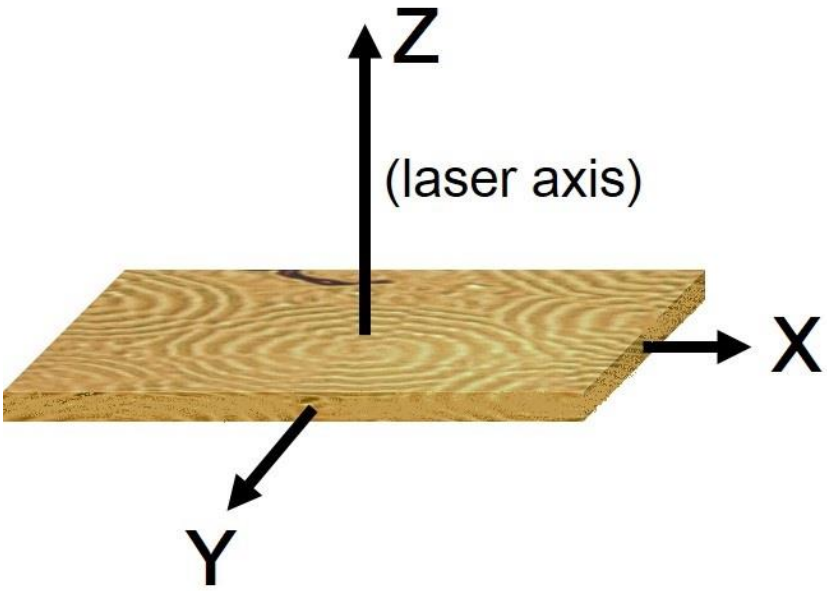

Figure A2-2. Schematic diagram of the scattering geometries used for polarized Raman measurements.

1. Dieing, T.; Hollricher, O.; Toporski, J., Eds. *Confocal Raman Microscopy*; Springer: Heidelberg, Dordrecht, London, New York, 2011.

A2-3. Examples of Curve-Fitting Results for PBA32

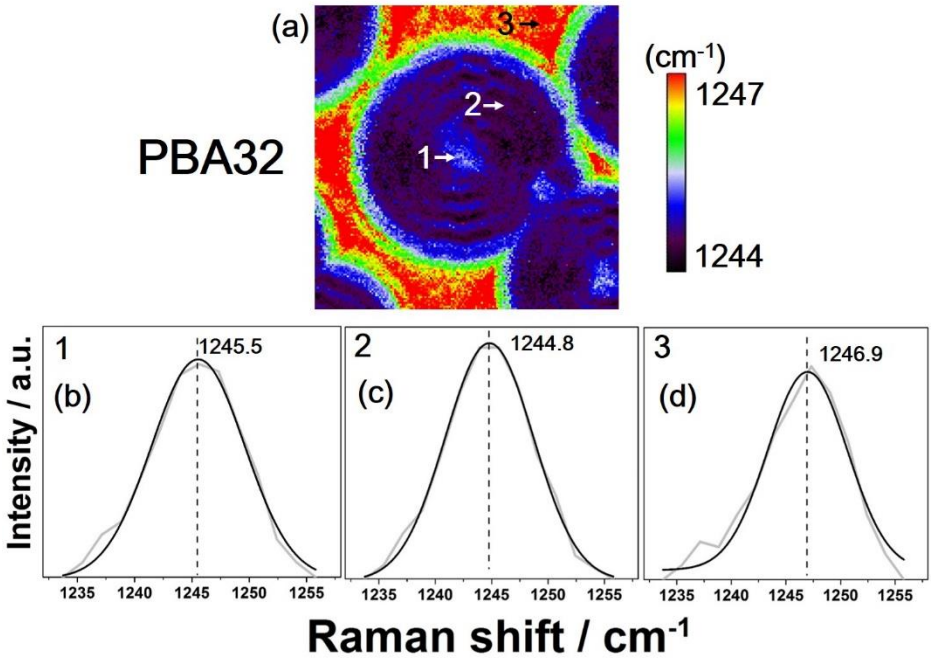

Figure A2-3. (a) Raman image developed by the peak position of the C-peak that obtained by curve fitting for PBA32. (b–d) examples of curve-fitting results for select point-1, 2 and 3 in (a).

A2-4. Band Spacing for PBA31–33

Since the ring-banded pattern within PBA spherulite is caused by the lamellar twisting, therefor the molecular chains orientation about the substrate plane is different between the adjacent rings. The different molecular chains orientation will induce the Raman intensity change, because the angle between the incidence Raman laser and the polarizability of the chemical bond will variance with the molecular chains orientation.

Therefore, peak area change of the C-peak along the radial direction of the spherulite was used to calculate the band spacing in present study.

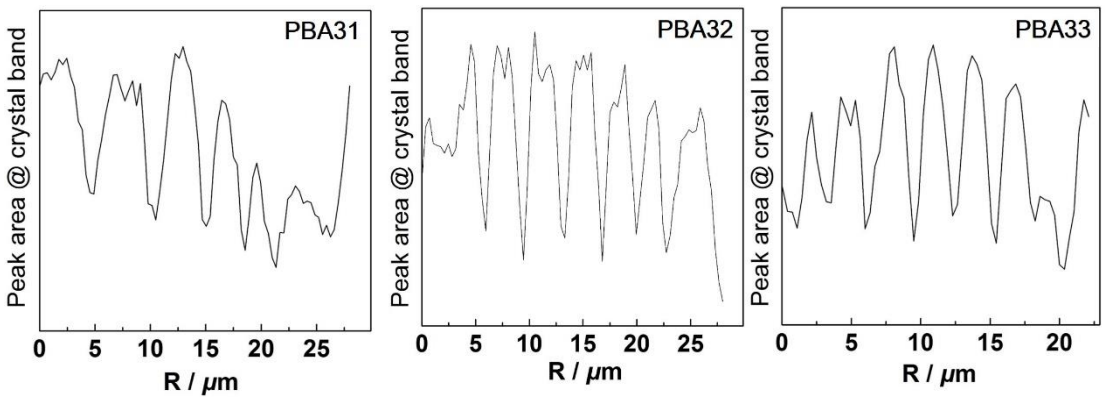

Figure A2-4. Peak area change of the C-peak for PBA31–33 along the radial direction of the spherulite.

A2-5. Raman images by peak area of α-form, β-form peak, C-peak and ν(C=O) peak of PBA32

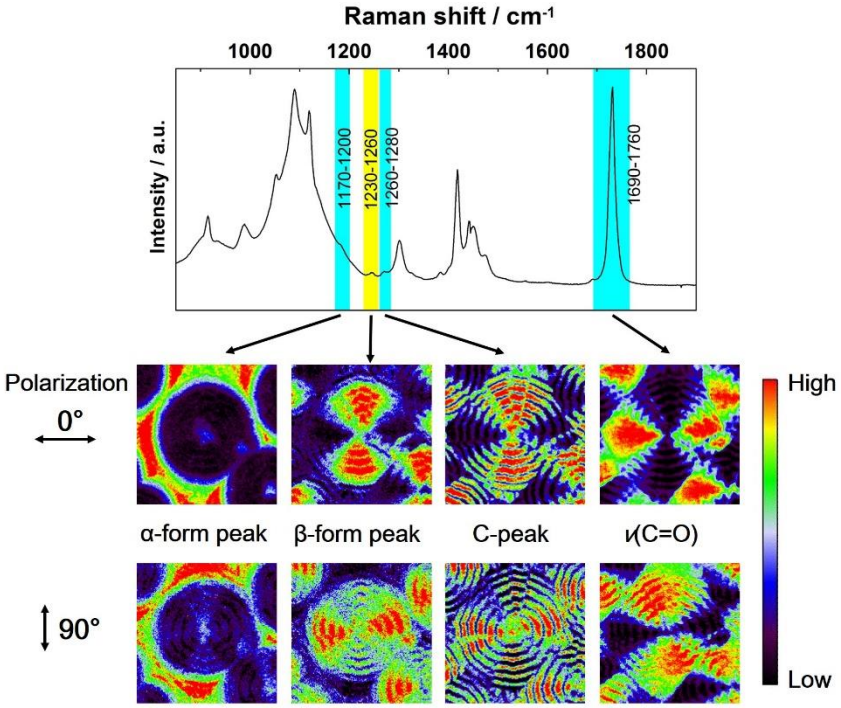

Figure A2-5. Raman images by peak area of *α*-form, *β*-form peak, C-peak and *ν*(C=O) peak of PBA32

Acknowledgments

During the evolution of this dissertation, I am deeply indebted to everyone who have guided and supported me in many ways.

I would like to express my utmost gratitude to Prof. Yukihiro Ozaki from Kwansei Gakuin University, my supervisor, for his sincere and endless encouragement, selfless support, and kind advice throughout all the stages of my research in Ozaki Group. Moreover, I am so much appreciated that Prof. Ozaki provided me a very good research environment and strong supported every of my idea. He also devoted a considerable portion of his time to read my manuscript and gave me insightful suggestions for further revisions. It was him, who showed me what the real scientist is, made me truly grown up.

At the same time, I want to give my heartfelt gratitude to Prof. Kohji Tashiro from Toyota Technological Institute, who is undoubtedly another most important person for this dissertation. Thank you for him allowing me to do experiments in his lab, and instructed me many valuable experiment techniques and skills for polymer science. I will not forget the discussion with Prof. Tashiro, he answered every of my question patiently even in the midnight. All of the guidance from Prof. Tashiro were much helpful for my research, and will also continuously influence and help me in the future.

I also must thank to Prof. Isao Takahashi for the support with the X-ray instrument. Thank you for Dr. Shigesaburo Ogawa for the help with the X-ray measurement. Thank you for Prof. Harumi Sato from Kobe University, Prof. Jianming Zhang from Qingdao University of Science and Technology, and my Master degree adviser, Prof. Weiyu Cao from Beijing University of Chemical Technology, who spared their time to discuss with me and gave many professional advice to me.

The same thanks should also give to Dr. Khasanah, Dr. Sanpon Vantasin and Mr. Jiping Wang, who are not only very important research partners but also good friends of mine. I also want to give my thanks to all Ozaki group members.

I would like to thank Japanese Government and Kwansei Gakuin University for the scholarship and financial supporting on my research and living in Japan.

Finally, but not the least, I want to express my great appreciation to my parents, girlfriend and all closest friends, for their selfless accompany and encouragement. Nothing can replace them in my heart.

List of Publications

1. **Mengfan Wang**, Khasanah, Harumi Sato, Isao Takahashi, Jianming Zhang, and Yukihiro Ozaki; Higher-order structure formation of a poly(3-hydroxybutyrate) film during solvent evaporation. *RSC Advances* **2016**, *6*, 95021–95031. **[Chapter 1]**
2. **Mengfan Wang**, Kohji Tashiro, and Yukihiro Ozaki; Reinvestigation of the β-to-α Crystal Phase Transition of Poly(butylene adipate) by the Time-Resolved X-ray Scattering and FTIR Spectral Measurements in the Temperature-Jump Process. *Macromolecules* **2017**, *50*, 3883–3889. **[Chapter 2]**
3. **Mengfan Wang**, Sanpon Vantasin, Jiping Wang, Harumi Sato, Jianming Zhang, and Yukihiro Ozaki; Distribution of Polymorphic Crystals in the Ring-Banded Spherulites of Poly(butylene adipate) Studied Using High-Resolution Raman Imaging. *Macromolecules* **2017**, *50*, 3377–3387. **[Chapter 3]**

List of related publications

4. Sanpon Vantasin, Wei Ji, Yoshito Tanaka, Yasutaka Kitahama, **Mengfan Wang**, Kanet Wongrawee, Harnchana Gatemala, Sanong Ekgasit, and Yukihiro Ozaki; 3D SERS Imaging Using Chemically Synthesized Highly Symmetric Nanoporous Silver Microparticles. *Angewandte Chemie* **2016**, *128*, 8531–8535.
5. Jiping Wang, **Mengfan Wang**, Yukihiro Ozaki, Harumi Sato, and Jianming Zhang; Investigation of Crystallization Behavior of Asymmetry PLLA/PDLA Blend Using Raman Imaging. *Vibrational Spectroscopy* submitted.